SUPERCONDUCTIVITY AND MIXED VALENCY IN THALLIUM-DOPED LEAD TELLURIDE

A DISSERTATION

SUBMITTED TO THE DEPARTMENT OF MATERIALS SCIENCE AND ENGINEERING

AND THE COMMITTEE ON GRADUATE STUDIES

OF STANFORD UNIVERSITY

IN PARTIAL FULFILLMENT OF THE REQUIREMENTS

FOR THE DEGREE OF

DOCTOR OF PHILOSOPHY

Yana Matsushita

March 2007

I certify that I have read this dissertation and that, in my opinion, it is fully adequate in scope and quality as a dissertation for the degree of Doctor of Philosophy.

(Ian R. Fisher) Principal Co-Adviser

I certify that I have read this dissertation and that, in my opinion, it is fully adequate in scope and quality as a dissertation for the degree of Doctor of Philosophy.

(Theodore H. Geballe) Principal Co-Adviser

I certify that I have read this dissertation and that, in my opinion, it is fully adequate in scope and quality as a dissertation for the degree of Doctor of Philosophy.

(Bruce M. Clemens)

Approved for the University Committee on Graduate Studies.

Abstract

Tl-doped PbTe ($Pb_{1-x}Tl_xTe$) is a degenerate semiconductor exhibiting superconductivity at a remarkably high T_c given its relatively low carrier concentration of $\sim 10^{20}$ cm^{-3}. For Tl concentrations x beyond a critical value $x_c \sim 0.3\%$, it is observed to superconduct with T_c rapidly increasing with x up to a maximum T_c of 1.5 K for the highest Tl doping of 1.5%. In comparison, other similar superconducting semiconductors can achieve comparable T_c values with much higher carrier concentrations. Since thallium is the only impurity known to cause superconductivity in PbTe, there has been considerable discussion as to the role of the Tl impurities in this material. In particular, it has been suggested that the superconductivity can be linked to the presence of a mixed Tl valence fluctuating between Tl^+ and Tl^{3+} states.

We investigate the superconducting and normal state properties of single crystal Tl-doped PbTe samples for a range of Tl concentrations up to the solubility limit of approximately 1.5%. Estimates of superconducting parameters from heat capacity and upper critical field measurements show that the material is a Type II, weak-coupled BCS superconductor in the dirty limit. Evidence for the mixed valence state appears as a carrier

concentration saturation in the Hall effect measurements, indicating a self-compensating mixture of Tl^{+} (acceptors) and Tl^{3+} (donors) beyond a characteristic Tl concentration near x_c. Furthermore, we show evidence that an anomalous low-temperature resistivity upturn may be associated with a charge Kondo effect arising from the quantum valence fluctuations between the degenerate valence states of the Tl impurities. The resistivity anomaly was observed only in superconducting samples where $x > x_c$. These observations would support the notion of an alternate pairing mechanism for superconductivity in this material which is linked to the presence of the mixed valence state.

Acknowledgments

As every Ph.D. student knows, the journey to completing a thesis is a long and difficult one that is impossible to survive without the help and support of numerous others. The most important contributors and greatest source of guidance for me were of course my two advisors Ian Fisher and Ted Geballe. Even though I was coming from a background of Materials Science, their role as excellent teachers and the source of motivating encouragement almost convinced me that I could tackle the challenge of comprehending superconductivity. Ian always had the energetic enthusiasm that had pulled me into the project in the first place and had helped sustain my efforts through tedious tasks. I was lucky to have benefited from his close involvement in the lab and in the thesis project and will always appreciate his exceptional kindness and sincerity as both an advisor and mentor. It was also an honor and a privilege to have worked with Ted. I am grateful for his immense knowledge and infinite wisdom that contributed so much to the project. I can only strive to achieve the same agility of the mind when I reach his age.

I would also like to thank the rest of my thesis defense committee for their contribution. Together with my two advisors in Applied Physics, it was a perfect mixture

of committee members with Bruce Clemens and Paul McIntyre from Materials Science, Mac Beasley from Applied Physics, and James Harris from Electrical Engineering. It was a privilege to engage in discussion of my project with them.

The Fisher lab had many supportive and memorable members who were closely involved in the development of my thesis. I owe much of my more interesting and exciting thesis experiences to the colorful members of the Fisher lab. Suchitra, Kyungyun, Nancy, Ann, and Eric were my fellow labmates enduring the same equipment frustrations and sharing small lab triumphs together. As Ian's first students, Suchitra, K-Yun, and I relied on each other as we learned the lab basics including sporadically successful crystal growth, stressfully delicate glasswork, and clumsy liquid helium transfers. Suchitra was a colorful entity in the lab whose occasional mischief certainly kept the lab interesting. I am thankful for her support that she continued to provide as we made progress in our separate projects. I would also like to thank K-Yun for his willingness to help with any task and for his general good nature. I owe thanks to Nancy for her always pleasant support and for helping me laugh away the happenings in the group, both good and bad. I also appreciated Ann for helping with the lab responsibilities when I know it can be overwhelming at times. I have really enjoyed having Eric as a very considerate and supportive labmate and desk neighbor who, along with K-Yun, provided much needed help especially with tasks needing some extra muscle. Additionally, I owe many thanks to the superstar undergrads Tim, Philip, Piotr, and Ariel who have helped with my project or have otherwise provided support in the lab.

I must also thank my other lab family, the KGB group. Gert, Myles, Alan, Mike,

and Dave were kind and patient enough to help me out in the early stages of my thesis. Other support came from Rafael, Wolter, Jeong-Uk, Jing, Sylvia, Andy, and Bob Hammond. I owe numerous thanks to Paul for his friendship and extensive help with almost everything. The KGB lab was an excellent resource for vacuum needs, temperature control problems, spare parts, and general physics questions. In particular, I much appreciated the extra support from Gert, Myles, Paul, and Wolter when dealing with the pains of the PPMS through the years. I would like to again thank Mac Beasley for his support and for always inspiring integrity in my work. I also owe thanks to Aharon Kapitulnik for his honest criticism and expert advice. It was an honor to be a part of such a historical group.

The rest of the GLAM community also provided essential support for completing this thesis work. I would like to thank Corrina, Droni, Roberta, Judy, Cyndi, and Angela for their quick and friendly help with administrative dealings, whether it be for a form to fill out or a dire need for a projector. I owe thanks to Arturas for his aid with the XRD and to Mike Kelly for XPS advice. I have enjoyed and appreciated the EMPA services of Bob Jones and will miss our discussions very much. I also acknowledge the valuable resources and friendliness of all neighboring labs in GLAM, especially the Manoharan Lab, the Moler Lab, the Greven Lab, and the Shen Lab. I owe special thanks to Larry for holding the building together and keeping us safe. Of course, I cannot show enough appreciation for Mark Gibson for always bringing our packages with a smile and for always going above and beyond to help us with shipments and equipment.

Outside of GLAM, I would like to thank the Machine shop fellows for their friendly

services and for their willingness to work with me on complicated parts. In the MSE department, I am thankful for the administrative support from Stephanie, Doris, and Billie. I also owe many thanks to the folks at SLAC, especially Todd Slater for his frequent help with purchasing and liquid helium needs.

I could not have survived life at Stanford and the trials of the Ph.D. career without essential friends and family to support me. My MSE friends Juliet, Aditi, Pete, Gloria, Homan, David Chi, Andrew, and Melissa formed a group of support and encouragement to help each other survive the first few years of grad school. Juliet and Aditi were especially supportive in helping me through the last stretch. They provided the best technical and non-technical research advice during my times of need. I am grateful for the friendship of David Mann, Alex, Russell, and Laura and for keeping me from working too hard. I am also thankful for the MSE IM Soccer team and the Silicon Valley Soccer Association Women's and Co-ed teams for the friendship of my teammates and for providing an outlet for stress. Finally, I would like to thank Jonathan for always being there for me.

Contents

Chapter 1

Introduction

The many accomplishments in the field of superconductivity have allowed for a clear comprehension of most traditional low-temperature superconductors, but much work still remains for the full understanding of many unconventional systems. For example, the microscopic theory for superconductivity developed by Bardeen, Cooper, and Schrieffer (BCS theory) that has successfully described most conventional superconductors has been found insufficient on its own to explain the high values of T_c in high-temperature cuprates. Even within BCS theory which assumes a small attractive interaction to form bound electron pairs, the mechanism of the attraction does not necessarily have to be from conventional electron-phonon coupling. For this reason, the possibility of alternate pairing mechanisms or electron interactions has been suggested [1, 2].

In order to explain the highest T_c values of the cuprates, further possibilities like an enhanced interaction or an additional pairing mechanism of unconventional form have been suggested [2–5]. One such mechanism that has attracted much attention involves

negative-U centers. It was noted that the cuprates with the highest T_c values contained the heavy metal ions Tl, Bi, or Pb in the charge reservoir layers. These ions are known to skip valence states. For example, compounds containing Tl are known to form Tl^{+} or Tl^{3+} but not the Tl^{2+} valence [6]. This behavior can be characterized in terms of a negative (attractive) on-site correlation energy, or negative U [7]. The tendency to form two valence states differing by two electrons suggests local pairing at the negative-U site as a possible unconventional pairing mechanism for superconductivity [8–13].

The study of impurities in superconductors has been discussed before, including the notion of impurities that may cause superconductivity in a material [13, 14]. For example, it has been suggested that a narrow impurity band could enhance the density of states at the Fermi level and increase the carrier concentration, resulting in superconductivity [15, 16]. A more intriguing theory has been suggested where a special type of impurity, a negative-U impurity, can supply the pairing mechanism that both causes superconductivity and enhances T_c [8, 9]. While such systems have been described theoretically, convincing experimental evidence that such a mechanism plays a dominant role in any real materials has not been previously shown.

We have chosen to investigate Tl-doped PbTe ($Pb_{1-x}Tl_xTe$) as a model system to study whether Tl impurities can indeed act as negative-U centers and whether the centers can contribute to superconductivity. This simpler system lacks the more complex, layered oxide structure of the high-temperature cuprates. Tl-doped PbTe is a degenerate semiconductor with carrier concentrations no more than 10^{20} cm^{-3} [17–19]. It is known to superconduct up to approximately 1.5 K at the solubility limit of $x = 1.5\%$ Tl [16].

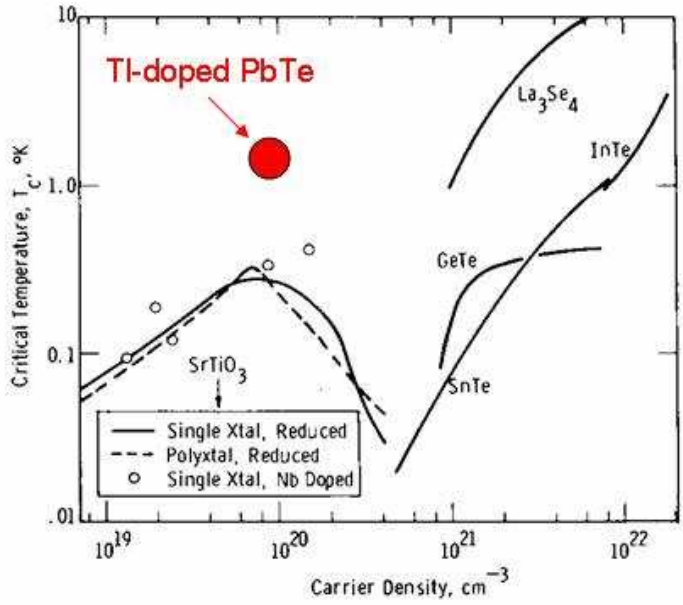

Figure 1.1: Critical temperature T_c as a function of carrier density of several superconducting semiconductors, taken from Ref. [20]. The red spot representing the highest T_c observed for Tl-doped PbTe is added for comparison.

While this may sound like a small value of T_c, the superconductivity in this material is somewhat anomalous when compared with similar doped semiconductors that exhibit superconductivity. Figure 1.1 is taken from Ref. [20] where the T_c of various superconducting semiconductors are shown as a function of their carrier densities. Tl-doped PbTe is depicted as the red spot at approximately 1.5 K and 10^{20} cm^{-3}. This comparison shows that the T_c of Tl-doped PbTe is approximately two orders of magnitude higher than expected for similar telluride compounds for the given carrier concentration. While La_3Se_4 and InTe can achieve comparable transition temperatures, they require much higher carrier densities.

Tl-doped PbTe is also of particular interest because Tl is the only impurity known to

cause superconductivity in the PbTe host [18]. PbTe can be doped to similar carrier concentrations by other dopants including vacancies, excess Pb, and Na impurities with no evidence of superconductivity. Furthermore, T_c is observed to rise rapidly with increasing Tl content. With respect to this behavior and the anomalously high T_c, my thesis work investigates the special role that the Tl impurities play in the superconductivity of this material.

The following is an outline of this dissertation:

Chapter 2 describes the physical vapor transport technique for growing the single crystals of Tl-doped PbTe in this study and the chemical analysis method. The chapter also explains the experimental techniques used for studying the low-temperature thermodynamic and transport properties of the material.

Chapter 3 provides some relevant theoretical background. The first section provides the details of the electronic structure of PbTe that is necessary for subsequent analysis of the material. Then, we introduce the negative-U system, valence-skipping elements, and mixed valence systems. Within the negative-U model, we show how the Tl impurities achieve degeneracy between the Tl^{+} and Tl^{3+} valences via a self-tuning doping process and cause pinning of the chemical potential. Significantly, a unique charge Kondo effect has been predicted in negative-U mixed valence systems. We include an introduction to the more commonly known spin Kondo effect and explain the analogous charge Kondo characteristics. It is noted here that, while this phenomenon has been discussed theoretically, it had not been observed experimentally prior to our work.

Chapter 4 describes the detail of the Hall effect analysis for Tl-doped PbTe and

reports the results for electronic transport parameters. The observation of a saturation in the carrier concentration with Tl doping is presented as evidence for the presence of a mixed valence state. The density of states is also calculated from heat capacity measurements combined with the Hall effect analysis.

Chapter 5 summarizes the superconducting properties of Tl-doped PbTe. We find that the material, as previously reported in the literature, is a Type II, BCS superconductor in the dirty limit. The chapter concludes by drawing attention to the apparent critical Tl concentration ($x_c \sim 0.3\%$) necessary for superconductivity.

Chapter 6 presents results of the normal state thermodynamic and transport properties. We first examine the full range of resistivity up to 300 K, finding a surprising linear temperature dependence and a residual resistivity that rapidly increases with Tl concentration. Significantly, the low-temperature data reveal a resistivity upturn characteristic of the Kondo effect. The effect is only observed in the mixed valence state and only for superconducting samples above the critical concentration. While a resistance minimum and low-temperature upturn may arise from other mechanisms, the data show some inconsistencies with these other possibilities. In particular, the magnetic susceptibility is diamagnetic, and there are no detectable magnetic impurities down to 5 ppm, ruling out the possibility of a magnetic Kondo effect. Although the magnetoresistance resembles some features of weak localization, it is difficult to fully describe the data using a simple weak localization scenario. The chapter concludes by suggesting the applicability of the charge Kondo model.

Chapter 7 discusses the observations of superconducting and normal state properties

in light of a charge Kondo model. We find that the size of the resistivity anomaly is consistent with only a small fraction of the Tl impurities contributing to Kondo scattering. Also, if we attribute the enhancement in electronic heat capacity to the Kondo resonance at the Fermi level, we find that the number of Kondo impurities is consistent with the number estimated from the resistivity anomaly. We offer a possible explanation by suggesting a distribution in the energies of the Tl states. Within the charge Kondo scenario, the relationship between T_c and the density of states roughly follows a BCS dependence, suggesting that the Kondo enhancement of the density of states is included. While the results are consistent with a distribution of Tl impurities, we also suggest other possibilities for the limited charge Kondo effect.

Chapter 8 summarizes the major conclusions and includes some ongoing collaborative experiments.

Chapter 2

Experimental Methods

2.1 Crystal growth

Doped PbTe and its quasi-binary systems have been studied extensively for their optoelectronic and thermoelectric applications, where the properties and growth techniques are reviewed by Khokhlov [19]. Studies of Tl-doped PbTe in particular and its superconductivity were mainly on polycrystalline material [15, 16, 21] and some more recent work on thin films [22]. There is limited work on single crystals grown from the Bridgman-Stockbarger method [23, 24] where the superconductivity was not investigated. In order to study the physics and transport properties without the effects or limitations of grain size, grain boundaries, and thin film strain, the work in this dissertation focuses on the characterization of single crystals of undoped and Tl-doped PbTe ($Pb_{1-x}Tl_xTe$) up to the solubility limit of $x = 1.5\%$.

The equilibrium phase diagram for the Pb-Te binary is shown in Fig. 2.1. The PbTe

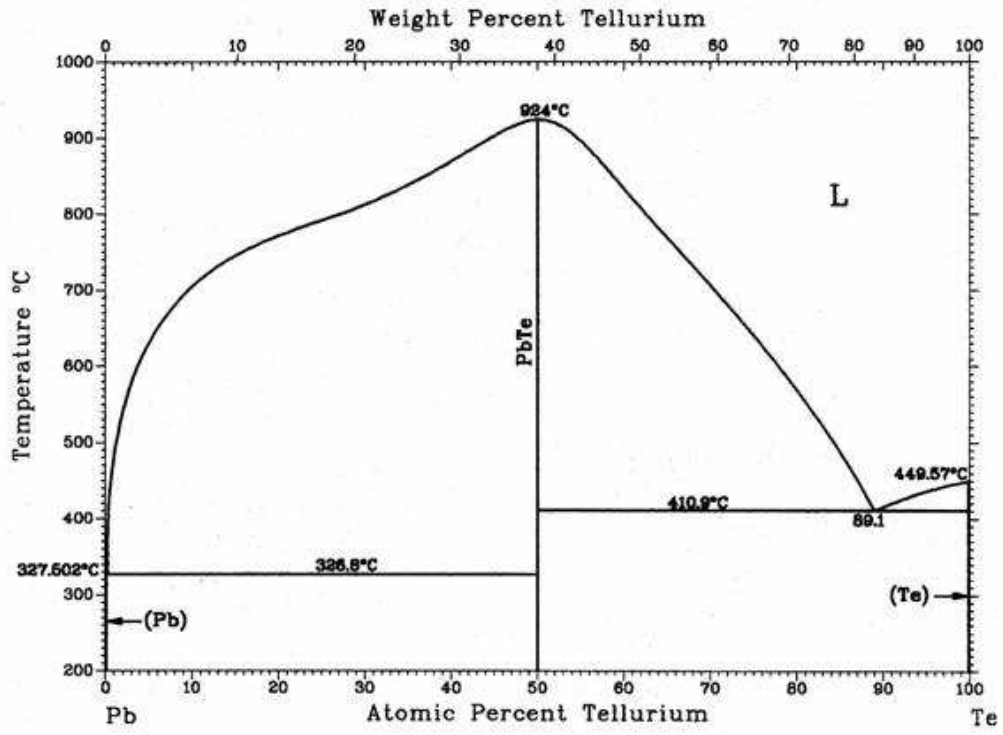

Figure 2.1: Equilibrium phase diagram for Pb-Te system taken from Ref. [25].

compound tends to form slightly off stoichiometry due to small concentrations of point defects. As a result, the material has a small width of formation. Depending on growth conditions, crystals are n-type PbTe with Te vacancies or p-type PbTe with Pb vacancies. The nonstoichiometric growth causes the material to be degenerate with typical carrier concentrations of $\sim 10^{18}$ cm^{-3}.

Single crystals were grown by an unseeded physical vapor transport method. The technique involves the vaporization of a source charge material at elevated temperatures in a sealed quartz ampoule. Small temperature gradients and long growth times allow nucleation and growth of homogeneous single crystals at the slightly cooler parts of the ampoule. The composition of the grown crystals are the same as the starting source material since the majority of the vapor transport occurs as molecules (i.e., PbTe) as opposed to the elemental constituents. Theoretical calculations of vapor pressures for the physical vapor transport of PbTe have shown that stoichiometric sublimation of PbTe occurs below 850°C, and dissociation of PbTe to gaseous Pb and Te_2 is less than 1% [26]. The transport by molecules was also confirmed by reported mass spectrometry results from Knudsen effusion of PbTe [27]. The procedure used here was developed from the vapor transport technique for bulk crystals described in Ref. [28] for $Pb_{1-x}Sn_xTe$ and from the polycrystalline source material preparation procedure for Tl-doped thin films in Ref. [22].

Since the melting and sublimation properties of the Tl source material (Tl or Tl_2Te) are different than PbTe and since all source material is vaporized in the same conditions in the same ampoule, it is necessary to pre-synthesize polycrystalline source material for

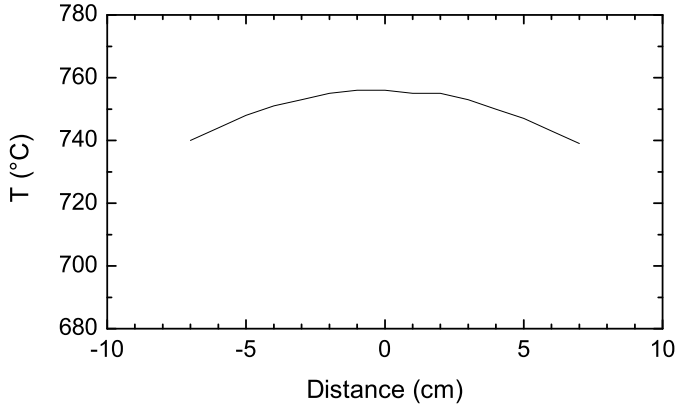

Figure 2.2: Temperature profile in horizontal tube furnace used for physical vapor transport of Tl-doped PbTe single crystals. Distance is measured from the center of the furnace.

sufficient incorporation of the Tl in PbTe and for controlling the final stoichiometry. The starting materials consist of PbTe (99.999%), Te (99.9999%), and either Tl_2Te (99.9%) or elemental Tl (99.999%) all purchased from Alfa Aesar. The excess Te is required for maintaining stoichiometry when adding Tl. The starting materials are ground to a powder in appropriate ratios for the desired stoichiometry. The powder is then cold pressed into pellets and sealed in a quartz ampoule in Ar gas. The pellets are sintered at 600°C for 24–48 hours, where the Ar gas helps prevent transport during sintering. The sintered material is ground, pressed, and sintered again to ensure incorporation and homogeneity. The result is a polycrystalline mass of Tl-doped PbTe.

For the crystal growth, the polycrystalline source material is crushed into 0.5–3 mm pieces and sealed in an evacuated quartz ampoule. The ampoule is placed in a horizontal tube furnace held at 750°C for 7–10 days. The measured temperature profile of the tube furnace is plotted in Fig. 2.2. The ampoule of approximately 8–10 cm placed in the

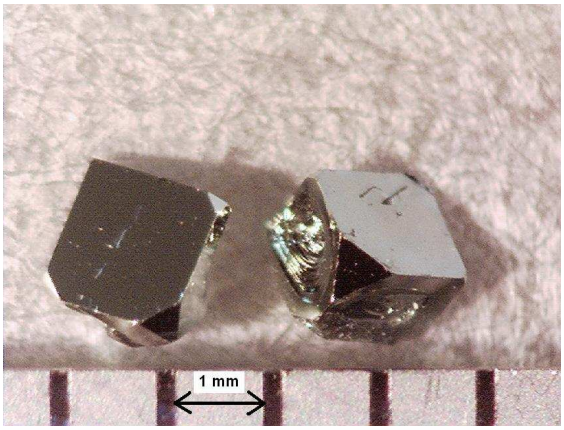

Figure 2.3: Optical image of vapor grown PbTe crystals shown on a millimeter scale. Cube faces of the crystals are (100) facets. Triangular faces are (111) facets.

center has a small temperature gradient of approximately 1–2°C/cm. The vapor from the source material at the higher temperature transports to one or both of the cooler ends of the ampoule where nucleation and growth of crystals take place. The slow growth ensures large, homogeneous single crystals. Each vapor growth produces several crystals up to a few millimeters in size that can be cut and cleaved to prepare bars for thermodynamic and transport measurements. An example of well-formed PbTe crystals with clear cubic morphology is shown in the optical image in Fig. 2.3.

The majority of the growths used Tl_2Te as the Tl source, since it grinds fairly easily compared to the extremely malleable Tl granules. Tl metal also oxidizes quickly in air. However, the Tl metal was of much higher purity. To ensure that the Tl_2Te source did not contribute spurious impurities and alter the Tl-doped PbTe properties, growth batches using different sources were compared. No significant difference in resistivity or susceptibility were observed between the different growths.

2.2 Chemical analysis of crystals

The thallium content was measured by Robert E. Jones using Electron Microprobe Analysis (EMPA). The technique uses an electron beam to eject core level electrons out of sample atoms. Electrons from higher energy levels de-excite by falling into these empty core states and emit x-rays characteristic of the atomic energy level transitions. A wavelength dispersive spectrometer (WDS) collects the emitted x-rays such that these characteristic energies appear as peaks in intensity versus wavelength. The chemical composition of the sample is determined by comparing intensities of peaks from the different elements. For accurate quantitative analysis, ZAF correction factors (incorporated in the instrument software) are necessary to account for atomic number (Z), x-ray absorption (A), and x-ray fluorescence (F) of the sample matrix. In addition, PbTe, Te, and Tl_2Te elemental standards are required. The use of PbTe and Tl_2Te standards as opposed to elemental Pb and Tl standards help reduce the error, since the chemical composition is close to that of the sample matrix. The Pb $M_{\alpha 1}$, Tl $M_{\alpha 1}$, and Te $L_{\alpha 1}$ peaks were used, since these had largest intensities and were farthest from other interfering peaks. Since flat sample surfaces are necessary for reliable microprobe analysis, the samples were either cleaved or polished.

The microprobe analysis of all growth batches are shown in Fig. 2.4. Data were obtained for some polycrystalline source material (open symbols) as well as the grown single crystals (closed symbols). Since these data coincide, it is confirmed that the crystal growth maintains the Tl content of the source material and that only initial

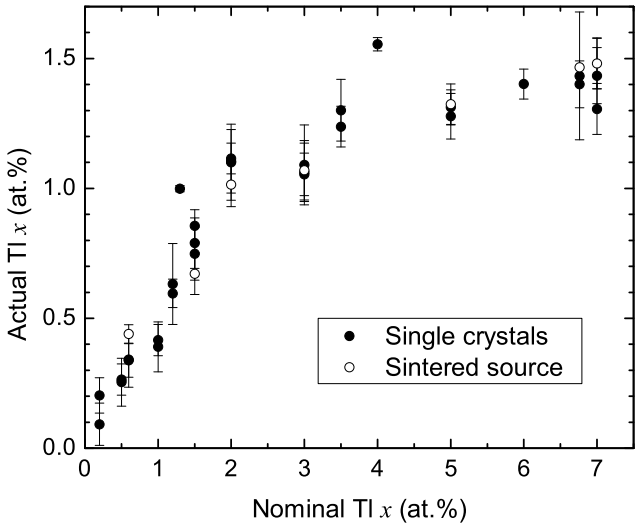

Figure 2.4: Tl content of grown single crystals (closed symbols) and polycrystalline source (open symbols) of $Pb_{1-x}Tl_xTe$ as measured by EMPA.

loss of the nominal Tl content occurs during the grinding and sintering processes. The Tl incorporation appears to saturate at approximately 1.5% near the solubility limit reported elsewhere [23]. Uncertainties are dominated by statistical errors of the signal count for such low Tl contents. Errors in Tl content x shown in subsequent figures reflect the uncertainty of the microprobe method. The Tl concentration for individual samples was observed to be homogeneous within the uncertainty of this measurement.

2.3 Resistivity and electronic transport

Extensive electronic transport studies were made for the characterization of the superconducting and normal state properties of Tl-doped PbTe. Samples for electronic transport measurements were fashioned into geometric bars approximately 1–2 mm in length and 0.2–0.5 mm thick. Since PbTe cleaves easily along the (100) planes, the bars

can be cleaved from the larger as-grown crystals. For best electrical contacts, gold pads were evaporated or sputtered onto the samples. Then 50 μm Pt wires were attached using Epotek H20E silver epoxy cured at 120°C for 15 minutes in air. Typical contact resistances ranged from 1 to 4 Ω.

Four-point resistivity measurements in zero field or applied magnetic field were made using a Linear Research Model 700 ac resistance bridge at 16 Hz. Current flowed along the [100] direction, and if applied, the magnetic field was oriented parallel to the equivalent [001] direction. For resistivity from 300 K down to 1.8 K, samples were measured with the resistance bridge in a Quantum Design Magnetic Property Measurement System (MPMS) loaded with a custom resistivity probe. The MPMS in this case was used for temperature control and for magnetic fields up to 5 T. For temperatures down to 0.3 K, the resistance bridge was attached to a Janis superconducting magnet cryostat system equipped with a ^{3}He insert and 9 T superconducting magnet. For temperatures down to 15 mK, the resistance bridge was integrated with an Oxford dilution fridge system in the laboratory of K. A. Moler, where measurements were performed with the help of H. Bluhm, N. C. Koshnick, and P. G. Björnsson. Depending on sample size, current densities ranged from 5 mA/cm^2 (corresponding to a current of 10 μA for low-temperature measurements in the dilution fridge) to 1 A/cm^2 at higher temperatures. To check for heating effects, resistivity data were taken for different current densities and for warming and cooling cycles for each sample.

Hall effect data were measured at 1.8 K in a Quantum Design Physical Property Measurement System (PPMS). Samples were prepared with 6 contacts, such that a

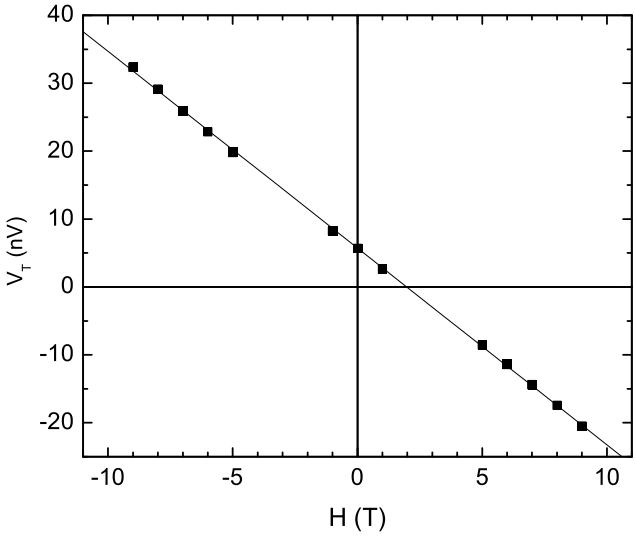

Figure 2.5: Measured transverse voltage V_T shown linear with field H for $x = 0.4\%$ at 1.8 K.

transverse and longitudinal voltage could be measured. An ac current at 37 or 77 Hz was used with current densities of 0.1–1 A/cm^2. The Hall voltage V_H was obtained from linear fits to the measured transverse voltage $V_T(H) = V_0 + V_H(H)$ for fields between -9 and 9 T. Slight misalignments of the transverse voltage contacts gave the zero-field component V_0 to V_T. An example of the measured V_T as a function of applied field is shown in Fig. 2.5.

Magnetoresistance in fields up to 14 T were measured using a Quantum Design Physical Property Measurement System (PPMS) equipped with a ^{3}He Option Insert. The resistivity was measured using an ac current excitation of 16, 37, or 77 Hz chosen to minimize noise. The current was applied in the [100] direction while the magnetic field was oriented perpendicular to the current. Small Hall effect contributions to the total

resistance measurements were occasionally observed from slight misalignments of the electrical contacts. These contributions are linear with magnetic field and were removed from all subsequent data presented in Chapter 6.

2.4 Heat capacity

The low-temperature heat capacity of single crystal samples was measured using a thermal relaxation technique in a Quantum Design Physical Property Measurement System equipped with a ^{3}He Option Insert. The system measures the heat capacity at constant pressure $C_p = (dQ/dT)_P$ by applying a controlled heat pulse to the sample and recording the sample temperature during heating and cooling as a function of time. The samples were mounted with Apiezon N grease onto a low heat capacity platform suspended by four thin wires. For the small sample heat capacity values at ^{3}He temperatures, a sapphire platform was required to reduce the error produced when subtracting the platform heat capacity contribution from the data. The heat capacity of the sapphire was also less sensitive to applied magnetic fields. Crystals with a mass of approximately 10–15 mg were prepared with a flat surface for good thermal contact to the sample platform. Measurements were made in zero applied field and in a field H=0.5–1 T $> H_{c2}$. The field was oriented at an arbitrary angle to the crystal axes, depending on the orientation of the flat surface.

2.5 Susceptibility

Magnetic susceptibility measurements were performed in a Quantum Design MPMS Superconducting Quantum Interference Device (SQuID) magnetometer for temperatures between 1.8 and 300 K. Samples with mass 50–100 mg were mounted with arbitrary orientation between two clear plastic straws. The magnetization $M(T)$ versus temperature was measured at 1000 Oe where the susceptibility is $\chi(T) = M(T)/H$. $M(H)$ loops were measured to confirm diamagnetic behavior that is linear with field.

2.6 High pressure experiments

Hall effect and resistivity were also measured under hydrostatic pressures up to 13.5 kbar at the University of California, Los Angeles in collaboration with Y. Kurosaki, J. Shinagawa, and S. E. Brown. Hydrostatic pressures were achieved with Be-Cu pressure clamp cells with Fluorinert pressure fluid from 3M. Pressure cells were mounted in a ^{3}He refrigerator equipped with a 1.5 T split-coil electromagnet. Resistivity was measured with a Linear Research Model 700 ac resistance bridge. Electrical contacts and configurations are similar to Section 2.3 for 6-point transport measurements to allow for the measurement of resistivity and Hall effect on the same sample. The pressure was estimated by comparing the room temperature pressurization of the cell with calibrated pressure data using a standard $T_c(P)$ curve for superconducting Pb. However, without a simultaneous measurement of the pressure during the run, the uncertainty of this calibration is approximately ± 0.5 kbar.

Hall effect was measured using an EG&G Princeton Applied Research Model 116 lock-in amplifier at 41.3 Hz. Since the sample configuration in the cell may have changed during cooling or pressurization, the split-coil magnet orientation for Hall effect measurements was determined by rotating the magnet and measuring the transverse voltage as a function of magnet angle. The Hall voltage was then measured from the linear fit of the transverse voltage versus field from 0.1 to 1.5 T.

Chapter 3

Theory and Background

3.1 Electronic structure of PbTe

PbTe is a narrow-bandgap semiconductor with $E_g = 190$ meV at 0 K. For the single crystals studied here, the material is a degenerate semiconductor with the Fermi level in the valence band due to either Pb vacancies contributing holes in the undoped PbTe (see Section 2.1) or due to Tl acceptors in the doped samples. This Section will focus on the main features of the valence band structure relevant to the characterization of this system. In the case of Tl doping and small hole doping from Pb vacancies, a rigid band model is assumed where only Fermi level position changes with doping and the band structure remains the same.

The electronic band structure calculated using pseudopotential calculations is shown in Fig. 3.1 from Ref. [29]. For reference, the symmetry points in the fcc Brillouin zone are shown in Fig. 3.2a. The direct bandgap at low temperatures is located at the L point, and

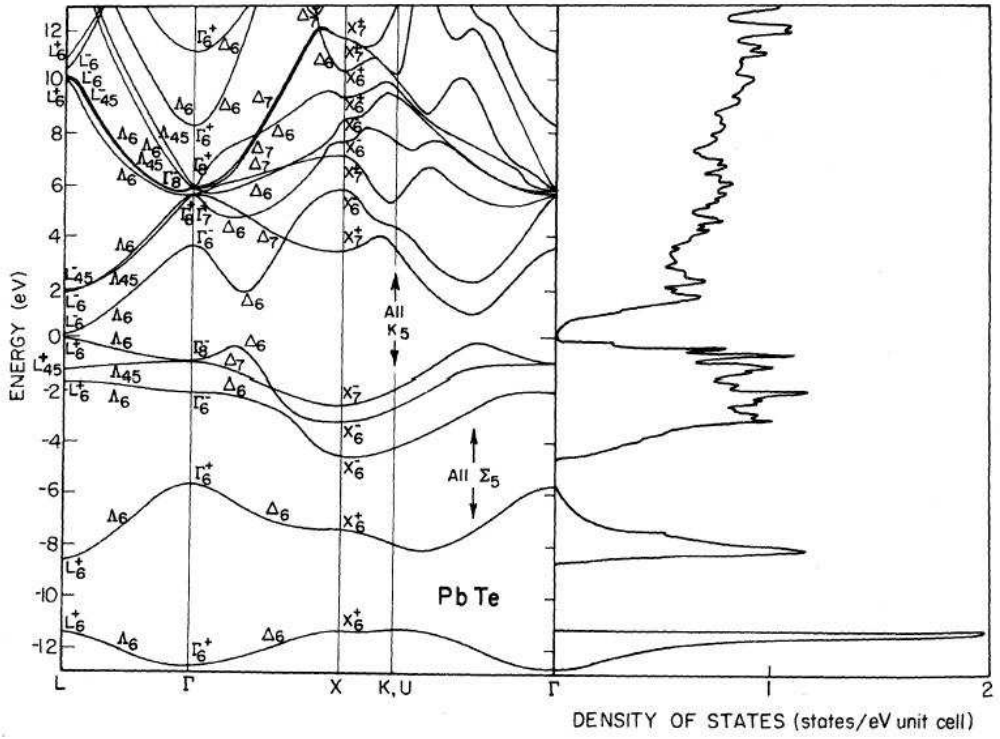

Figure 3.1: Band structure diagram and density of states for PbTe from Ref. [29] pseudopotential calculations.

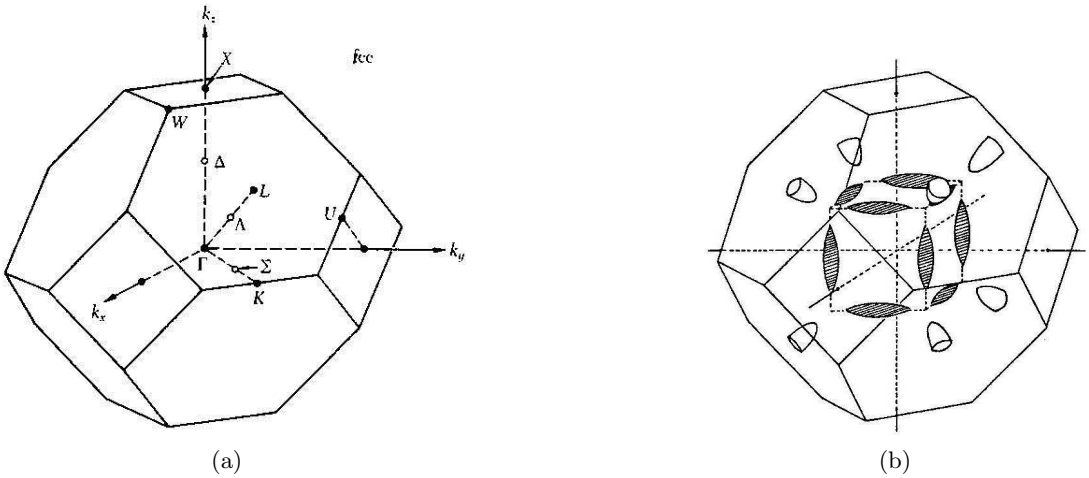

(a) (b)

Figure 3.2: First Brillouin zone of (a) fcc crystal showing symmetry points (taken from Ref. [30]) and (b) PbTe showing valence band hole pockets as 4 L and 12 Σ ellipsoidal Fermi surfaces (taken from Ref. [31]).

the valence band maximum consists of relatively light holes. The four ellipsoidal constant energy surfaces centered at the L points (shown as eight half-ellipsoids in Fig. 3.2b) are well characterized and have an anisotropy with a longitudinal mass $m_l = 0.31m_0$ and a transverse mass $m_t = 0.022m_0$.

A secondary valence band maximum is located at the Σ point in the Brillouin zone (Fig. 3.1). At zero temperature, the Σ-maximum valence band offset ΔE_v is approximately 170 meV below the top of the L band [18]. If sufficient hole doping places the Fermi level in the Σ band, the 12 heavier hole pockets are formed as illustrated in Fig. 3.2b. Much less is known about these states, and reported values for the effective mass range from 0.6–1.4m_0 [18]. However, we chose to use a density of states effective mass $m_\Sigma \sim m_0$ (defined over all Σ pockets as $N^{2/3}(m_t^2 m_l)^{1/3}$, where $N = 12$ is the number of pockets) and an anisotropy of roughly 10 reported in Ref. [32], since reasonable results for heat capacity and the density of states have been reported using these values [33]. Furthermore, we find that a mass larger than $m_\Sigma \sim m_0$ is inconsistent with our heat capacity data (see Section 4.3).

Since the majority of our transport characterization is at low temperatures, the low-temperature PbTe band parameters were used in calculations. However, the bands show a temperature dependence that is important to note when comparing with other studies. Figure 3.3 from Ref. [31] roughly sketches the temperature dependence of the bandgap (labeled ΔE_1) and the band offset (labeled ΔE_2). While most semiconductors have a bandgap that decreases with increasing temperature, PbTe has an uncommon positive coefficient for the bandgap temperature dependence. This has been explained by

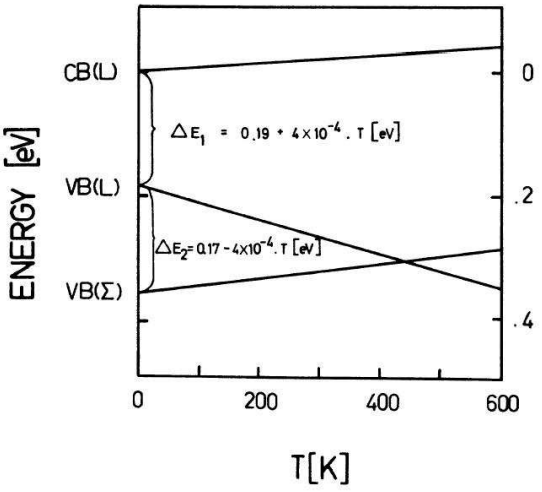

Figure 3.3: Temperature dependence of conduction band edge CB(L), valence band edge VB(L), and secondary valence band edge VB(Σ) in PbTe as a function of temperature (taken from Ref. [31]).

Debye-Waller factor calculations with larger Pb displacements than Te displacements and confirmed by band calculations [34]. The valence band offset decreases with temperature as the separation between the Σ valence maximum and the L conduction minimum remains nearly constant with temperature. At approximately 450 K, the band offset becomes zero and the bandgap becomes indirect.

We can determine the doping dependence of various transport properties using the known electronic band structure of PbTe to analyze the low-temperature Hall effect and resistivity data. Hall effect measurements for each Tl concentration give the carrier densities and Fermi level position in the valence band (Section 4.2). We can then use the resistivity of each sample to obtain values of hole mobility and mean free path as a function of Tl doping, as described in Section 4.2. These parameters are used in later analysis of superconducting parameters, density of states, and normal state transport

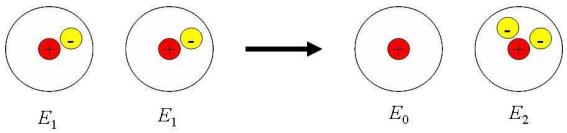

Figure 3.4: Illustration of removing an electron from one atom to another. E_n is the energy of the charge or valence state n.

properties.

3.2 Tl impurities as negative-U centers

Negative-U centers were first described by Anderson [35] in disordered semiconductors and can be impurity or defect sites where one finds empty or double charge occupation. Later, the negative-U model was specifically used to describe the behavior of valence-skipping elements like Tl and was even linked to superconductivity [7, 12]. This section introduces the negative-U model with respect to the valence-skipping behavior of elements like Tl. First, we describe how a negative U is defined and achieved.

The Hubbard energy U is the on-site electron repulsion energy and represents the energy to move an electron from one atom to another (see Fig. 3.4). It can be estimated by the difference between the ionization energy and the electron affinity, or

$$U_n = (E_{n+1} - E_n) - (E_n - E_{n-1}), \tag{3.1}$$

where n labels the charge or valence state. Estimates of U in vacuum for some valence-skipping elements are shown in Table 3.1 and are estimated from ionization energies [7].

Table 3.1: Repulsion parameter U for some valence-skipping elements as calculated by Ref. [7].

	U_{3+}	=	19.7		U_{2+}	=	16.9
Bi	U_{4+}	=	10.7	Pb	U_{3+}	=	10.4
	U_{5+}	=	32.3		U_{4+}	=	25.5
	U_{1+}	=	14.3		U_{1+}	=	13.1
Tl	U_{2+}	=	9.4	In	U_{2+}	=	9.2
	U_{3+}	=	20.9		U_{3+}	=	26.4

We see from these values that the energy cost to add an electron to the middle valence given in Table 3.1 is much less than for the other valence states. This is partly due to the stability of the filled electron shells. For example, the full electron configuration for neutral Tl is $[\mathrm{Xe}]4f^{14}5d^{10}6s^26p^1$. As a result, the Tl^{2+} configuration of $6s^1$ is much less stable than the configurations for Tl^{+} and Tl^{3+} with outer shells $6s^2$ and $6s^0$, respectively.

In vacuum, U is always positive as shown in Table 3.1 due to Coulomb repulsion. Since it is always favorable to add an additional electron to the isolated positive ion, spontaneous disproportionation will not occur in vacuum. When such ions are incorporated in a solid, an electric field from the polarizable medium can screen the local ion charge and lower the energy to add or remove an electron. In certain cases, the energy reduction is large enough to result in a negative effective U such that it is more favorable for double occupancy than single occupancy at a site.

Thallium is one of several elements that is known to skip valences, where the skipped Tl^{2+} valence can be characterized by a negative effective U. The Tl are found to disproportionate in compounds in which one would otherwise expect to contain divalent Tl.

For example, $TlBr_2$ is more specifically $Tl^{I}Tl^{III}Br_4$, and TlS is likewise $Tl^{I}Tl^{III}S_2$ [6]. Charge disproportionation is also expected for Tl in PbTe. The following Sections describe in further detail the behavior of Tl in PbTe and how it may achieve a special form of mixed valency. First, we explain the significance of mixed valence systems.

3.3 Mixed valence compounds

Compounds or systems that contain an element present in two different oxidation or valence states are referred to as mixed valence systems. There are various forms of mixed valence compounds. Robin and Day [6] used ligand field theory to describe mixed valency and classify the different types. In a class I system the different valence ions are found in different crystallographic sites. In a class III system, the different valences are found in equivalent sites such that, if there is no clustering, the wavefunctions are delocalized. A class II system is intermediate, where the different valences are found in sites of the same symmetry but with different ligand distances.

Many valence-skipping elements and negative-U impurities can form mixed valence compounds. There are known Tl compounds that form a static disproportionation where the two valences are found in different crystallographic sites. For example, $Tl^{I}Tl^{III}Br_4$ contains tetrahedral Tl(III) and dodecahedral Tl(I) sites. $Tl^{I}Tl^{III}S_2$ also has a similar structure with two distinct Tl sites. Such systems with static disproportionation are generally insulating.

The notion of a dynamically fluctuating valence in mixed valence compounds has

attracted some attention in different contexts [6, 10, 36]. In particular, it has been suggested that fluctuations between two degenerate valence states differing by two electrons might provide a pairing interaction for superconductivity [7, 10]. It was even suggested that negative-U centers may be a source of additional pairing and T_c enhancement in certain high-temperature cuprates [3], though there is little conclusive experimental evidence. Taraphder and Coleman [37] have also found that if the negative-U pair states are hybridized with the conduction or valence band, the pair fluctuations would resemble the spin fluctuations of the Kondo effect in heavy fermions. The phenomenon, called a charge Kondo effect, results from the degenerate, fluctuating valence (charge) states and further suggests a motion of pairs on and off an impurity site. Therefore the observance of a charge Kondo effect involving a fluctuating mixed valence state would suggest a pairing mechanism for superconductivity in a negative-U system. It was proposed to describe the superconductivity in the barium bismuthates ($BaPb_{1-x}Bi_xO_3$ and $Ba_xK_{1-x}BiO_3$) [7, 37, 38], but no direct evidence of the charge Kondo behavior was observed.

3.4 Description of Tl impurities in PbTe

PbTe has a rocksalt structure and has been treated with reasonable success using ionic models [39]. For example, pseudopotential band structure calculations have shown that the charge distribution in the unit cell is largely consistent with an ionic model [40]. Weiser [39] has calculated incorporation energies and doping behavior for Group III

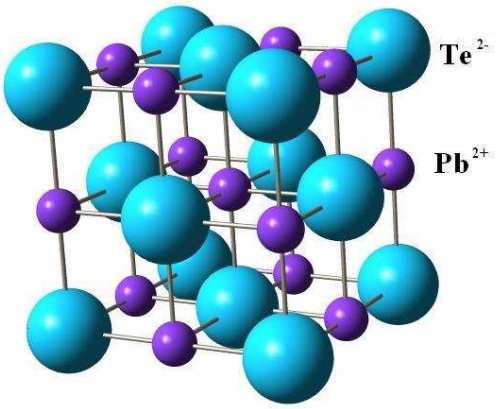

Figure 3.5: Rocksalt crystal structure of PbTe.

impurities in PbTe using an ionic lattice model. Figure 3.5 illustrates the ionic PbTe lattice model where Pb^{2+} cations and Te^{2-} anions form a rocksalt structure. Tl is known to substitute on the Pb^{2+} site. The interstitial sites in PbTe are too small for the Tl ion [39], and powder XRD has shown that there is no significant increase in the lattice parameter with Tl doping [23]. Since the Tl^{2+} is a forbidden valence, we see that substitution for the Pb^{2+} site will result in Tl^{3+} donors or Tl^{+} acceptors with a doping charge of one per Tl. Carrier freeze-out is not observed to the lowest temperatures, indicating that the dopant atoms do not behave as hydrogenlike impurities. This is due to the large dielectric constant ($\varepsilon_0 \sim 1000$) of the host PbTe reducing the ionization energy of the dopant [18].

The Tl valence skipping impurity has been described theoretically by Dzero and

Schmalian [8] using a negative-U model Hamiltonian,

$$H_{\text{imp}} = E_0 + (\epsilon_0 - \mu) \sum_{\sigma} n_{s,\sigma} + U n_{s\uparrow} n_{s\downarrow}, \tag{3.2}$$

where $n_{s,\sigma}$ is a spin σ hole occupying the $6s$ shell, μ is the chemical potential of holes, and U is negative. From Eq. 3.2, the energies of each Tl valence state can be expressed as

$$E(\text{Tl}^{2+}) = E_0 + \epsilon_0 - \mu \tag{3.3}$$

$$E(\text{Tl}^{3+}) = E_0 + 2(\epsilon_0 - \mu) + U \tag{3.4}$$

$$E(\text{Tl}^{+}) = E_0. \tag{3.5}$$

In this negative-U system, the Tl^{2+} state is the forbidden, high-energy state. It has been shown using an ionic model that the Tl^{+} acceptor has a lower energy than the Tl^{3+} donor in PbTe [39]. Therefore initially for small values of μ, the Tl impurities are all Tl^{+} acceptors for small doping levels and, as a result, μ increases deeper into the valence band as each Tl^{+} contributes one hole per Tl. However, the energy difference between the Tl^{+} and Tl^{3+} states, $\delta E = 2(\epsilon_0 - \mu) + U$, is very small in this system. We see from Eq. 3.4–3.5 that δE can be zero, such that the valence states become degenerate, when the chemical potential reaches a special value $\mu^* = \epsilon_0 + U/2$, corresponding to a critical Tl concentration of x^*.

Since the number of Tl acceptors or donors changes μ in this system and the formation

of either valence depends on the relative position of μ with respect to μ^*, we see that the behavior of μ and the Tl valence states are intrinsically dependent on each other. When $\delta E = 0$ is achieved, then the two valence states become degenerate and either state is likely to be formed. However, μ must remain pinned at μ^* for any Tl concentration larger than x^*, since $\mu > \mu^*$ would result in all of the Tl being Tl^{3+} donors. Therefore, any additional Tl beyond this critical value must form a self-compensating mixture of Tl^{+} acceptors and Tl^{3+} donors. The self-compensating formation of both valence states ensures that μ remains stationary, which in turn ensures the formation of both valences even with increased Tl doping. In other words, the ratio of Tl donors and Tl acceptors will always self-tune to keep μ at μ^* and maintain δE at zero.

This description illustrated in Fig. 3.6 shows the evolution of the Tl doping behavior as the Tl content is increased. For low Tl concentrations where $x < x^*$ and $\mu < \mu^*$ [Fig. 3.6a], the system is in a single valence state where only the Tl^{+} state exists. As x is increased, μ progresses deeper into the valence band as more Tl^{+} acceptors are formed. For $x > x^*$ [Fig. 3.6b], there is a coexistence of both Tl^{+} and Tl^{3+} in a mixed valence state and the chemical potential is pinned at μ^*. We present experimental evidence that appear to support this analysis in Chapter 4.

We see here that the Tl impurities achieve degeneracy between the Tl^{+} and Tl^{3+} valences via a self-tuning doping process and cause pinning of the chemical potential. The degenerate states suggest that dynamic valence fluctuations may interact with the valence holes in a charge Kondo effect as predicted above [37] for negative-U systems. To understand the characteristics of the charge Kondo system, the next Section 3.5

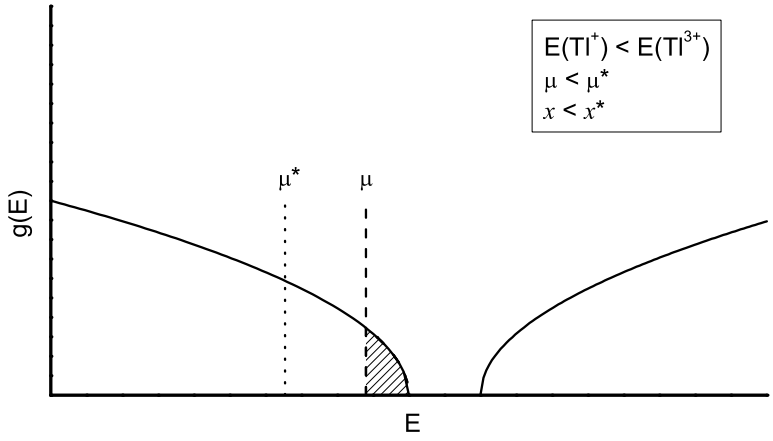

(a)

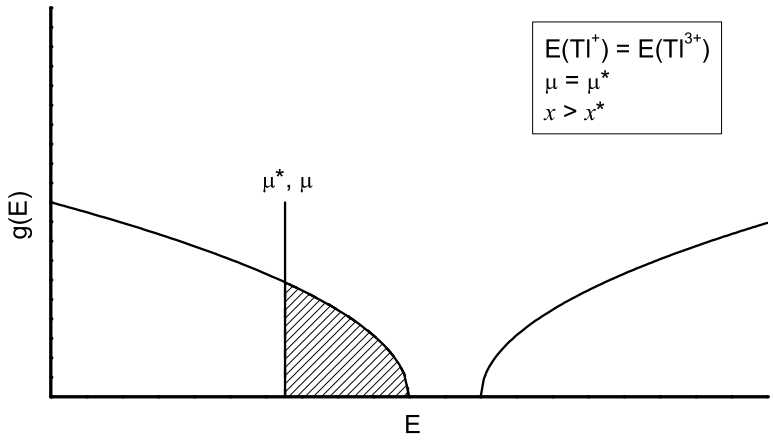

(b)

Figure 3.6: Schematic illustration showing chemical potential of holes μ and filling of the density of states $g(E)$ of PbTe for (a) when $\mu < \mu^*$ and (b) when $\mu = \mu^*$.

first introduces the more familiar spin Kondo effect and then describes the analogous properties of the charge Kondo effect.

3.5 Spin Kondo and charge Kondo effects

The Kondo effect arises from the interaction of conduction electrons with degenerate degrees of freedom in a material and is usually associated with dilute magnetic impurities in a nonmagnetic host [41]. In such cases, the two degenerate states correspond to the impurity spins oriented up or down. However, other systems comprising two degenerate degrees of freedom can also lead to Kondo-like phenomena [42], including the above-mentioned charge Kondo effect for negative-U impurities. We first illustrate the properties of a Kondo system based on the spin Kondo model.

The spin Kondo effect occurs in systems where U is positive and the spin degeneracy of the magnetic impurities cause a low-temperature increase in resistivity [41]. The resistivity minimum was explained by J. Kondo [43] who used third-order perturbation theory for scattering. Kondo noted that the upturn after the resistivity minimum was proportional to the impurity concentration c_{imp} and independent of the ratio c_{imp}/ρ_0 where ρ_0 is the residual resistivity. The temperature of the resistivity minimum T_{min} goes approximately as $c_{\mathrm{imp}}^{1/5}$ so is effectively insensitive to small changes in c_{imp}. Kondo also noted the correlation of the resistivity minimum to the presence of the impurity local moment.

At low temperatures, there is an antiferromagnetic coupling of the local moment

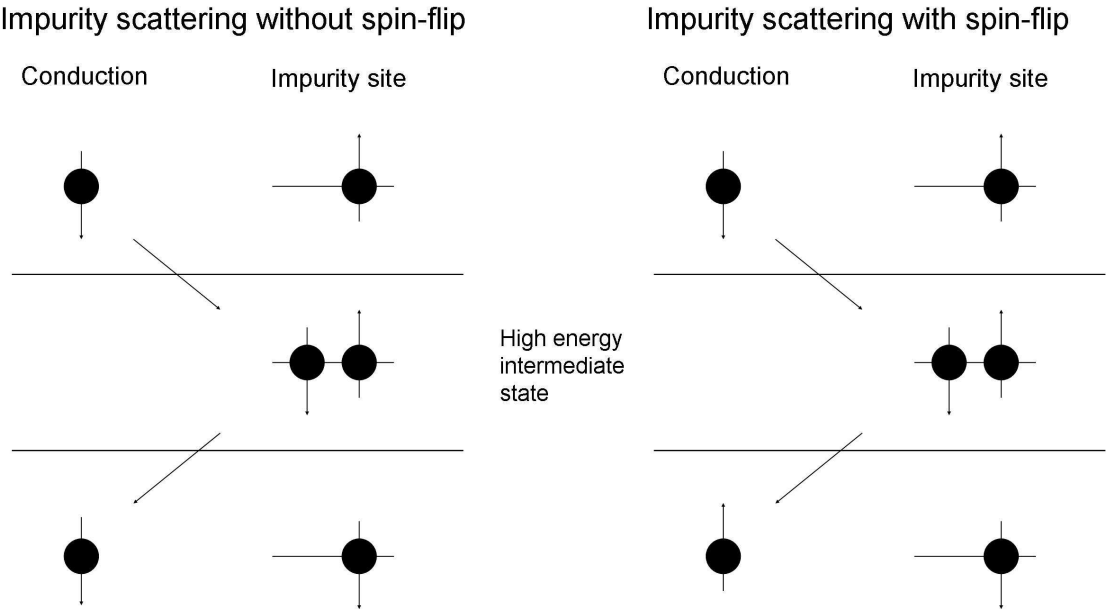

Figure 3.7: Illustration of scattering processes between an initial spin-down conduction electron and an initial spin-up magnetic impurity. The process on the left has no spin-flip events. The process on the right includes spin-flip scattering.

to the conduction electrons. At higher temperatures, the interaction can be treated in terms of a scattering process. These scattering processes are illustrated in Fig. 3.7 for initial local spin-up impurity interacting with a conduction spin-down electron [44]. There is a high-energy, intermediate state where the conduction electron is temporarily localized at the impurity site. In this case, it costs an energy U to place two electrons in the same impurity orbital. In the left figure, the final state is with the delocalized conduction electron and local impurity maintaining their initial spin. In the right figure, a spin-flip scattering process occurs where the final state has the spins reversed due to the degeneracy of the spin states. It is the contribution from these spin-flip processes in third-order perturbation theory that result in a $\ln T$ increase in resistivity at low temperatures.

However, a logarithmic temperature dependence would not be valid at the lowest temperatures, since it would require a diverging resistivity at $T = 0$ K. It was later determined that a ground state with infinite coupling is necessary, meaning the impurity spin is completely screened or bound by the conduction electron. The screened impurity reduces the amount of Kondo scattering. As a result, a power low would be expected from weak excitations to the triplet state. An exact solution from Fermi liquid theory found the resistivity to follow T^2 in this limit below a characteristic Kondo temperature T_K [41]. The overall form of the resistivity is sketched in Fig. 3.8a where there is a $\ln T$ increase below a resistivity minimum and a T^2 saturation below T_K. As an example, the results for Fe in Cu are shown in Fig. 3.8b.

The idea of a charge Kondo effect associated with degenerate valence (charge) states

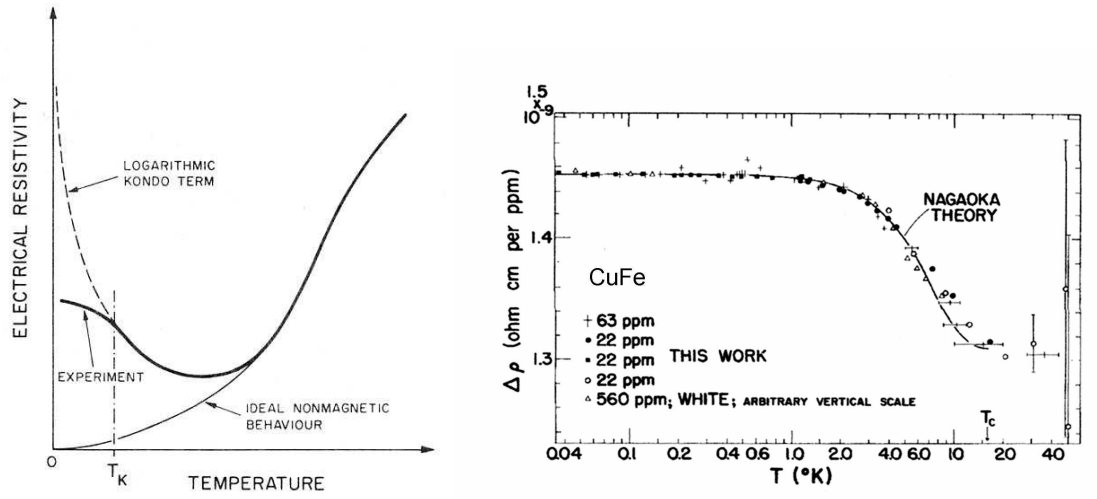

(a) (b)

Figure 3.8: (a) Schematic of the Kondo effect resistivity minimum at low temperatures (taken from Ref. [44]). (b) Kondo contribution to the resistivity for Fe in Cu showing typical logarithmic increase with decreasing temperature followed by resistivity saturation at low temperatures (taken from Ref. [45]).

of a valence-skipping element was first discussed by Taraphder and Coleman [37]. It was later reexamined in the limit of dilute impurities for the case $T_c \sim T_K$ and specifically for Tl-doped PbTe by Dzero and Schmalian [8]. Weak hybridization of these degenerate impurity states with conduction electrons (or in the case of Tl-doped PbTe, with valence band holes) results in a Kondo-like effect with various parallels to the more common magnetic case. Here, the pseudospins correspond to zero or double occupancy of an impurity orbital represented by the Tl^{3+} and Tl^{+} states, respectively. The pseudospin scattering processes are sketched in Fig. 3.9 where a conduction pair interacts with the Tl impurity. The intermediate state in this case is the formation of the forbidden, singly-occupied Tl^{2+} valence, temporarily costing an energy $|U|$. The pseudospin-flip process on the right side results in the impurity state flipping from the occupied Tl^{+} state to the

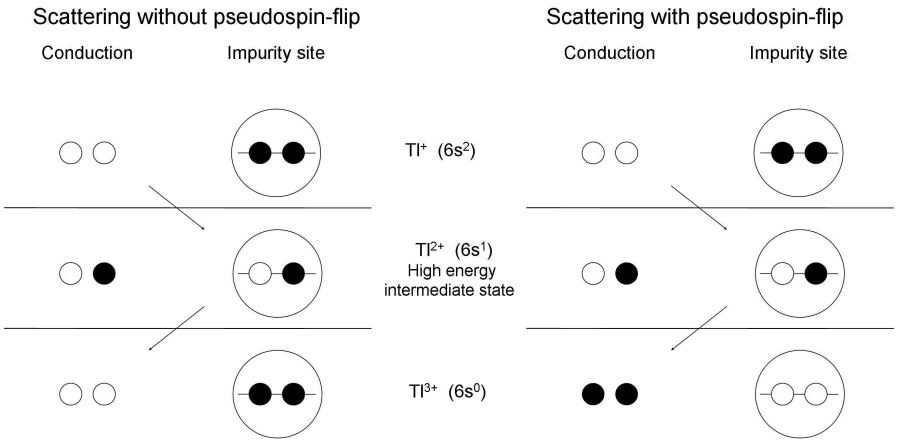

Figure 3.9: Illustration of scattering processes between an initial spin-down conduction electron and an initial spin-up magnetic impurity. The process on the left has no spin-flip events. The process on the right includes spin-flip scattering.

Tl^{3+} state. The resistivity would therefore follow an analogous logarithmic temperature dependence and then a T^2 saturation below T_K where the local pair becomes screened.

The correlation of the charge Kondo effect with superconductivity has been treated theoretically in the literature. Monte Carlo simulations have shown that negative-U impurities can enhance T_c [9]. For systems where $T_c \gg T_K$, it was suggested that there would be preformed pairs above T_c, since screening of the local pair pseudospin would take place well below T_c [11]. In such systems, T_c is finite down to small concentrations. The case for $T_c \sim T_K$ is complicated by the fact that the impurities supply the pairing interaction while the Kondo scattering is pair-breaking. Dzero and Schmalian [8] found that negative-U impurities both induce superconductivity and enhance T_c, and that there is a critical concentration above which superconductivity occurs. A distinguishing feature that may arise from the charge Kondo model is a reentrant superconductivity. The calculation from Ref. [8] is shown in Fig. 3.10 where T_c is plotted as a function

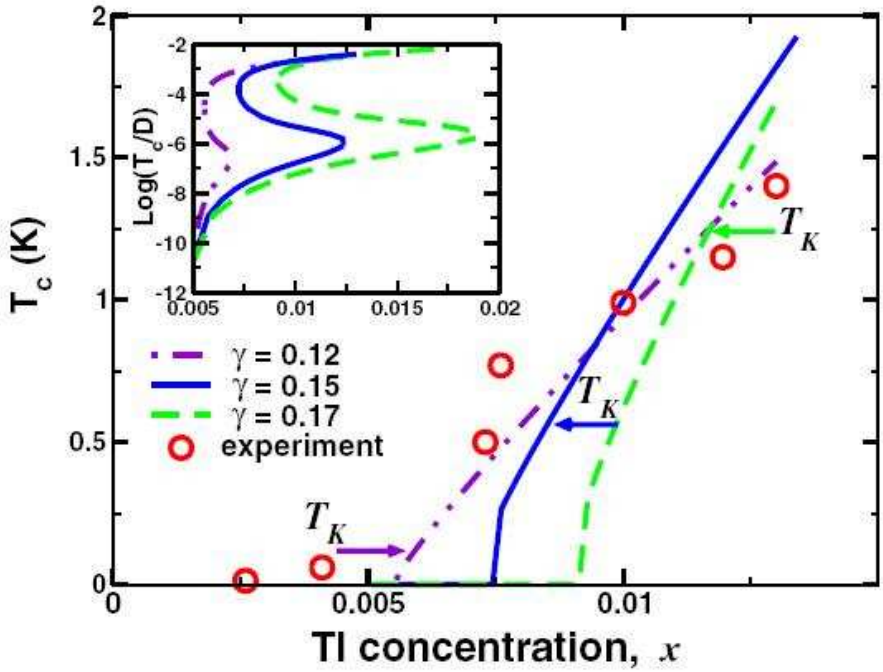

Figure 3.10: T_c as a function of x for different exchange coupling constant γ (taken from Ref. [8]). Experimental data are taken from [47]. Inset shows the low temperature region where reentrant superconductivity appears.

of concentration of impurities for different exchange coupling constant γ as defined in Ref. [8]. The inset shows the low-temperature regime where reentrant superconductivity appears. Such a feature is analogous to reentrant superconductivity in a spin Kondo system such as (La,Ce)Al_2 [46].

The observation of Kondo characteristics without the presence of magnetic impurities would provide evidence for a charge Kondo effect consistent with the fluctuating valence and negative-U model in Tl-doped PbTe. It would further support an unconventional pairing mechanism for superconductivity in this material, potentially accounting for the unexpectedly high T_c values. Signs of a resistivity minimum in Tl-doped PbTe were first

observed by Andronik and co-workers [24] with a limited Hall effect and magnetoresistance analysis. While it was suggested that the observation of the Kondo-like behavior was consistent with scattering in a two-level system [16], further evidence describing the nature of the two-level center was lacking. For this reason, the focus of this dissertation and the following chapters examine evidence in the superconducting and normal state properties that are consistent with a mixed valence, charge Kondo system.

3.6 Resonant impurity band model

Other groups have previously studied Tl-doped PbTe and have accounted for the transport properties and superconductivity in terms of a resonant impurity band model [15, 16]. In this scenario, the Tl impurities are said to form quasilocalized impurity states that are resonant in the valence band. An enhancement in T_c is attributed to the increase in the density of states when the chemical potential enters the narrow impurity band [22, 48]. The filling of this band accounts for observed chemical potential pinning as the filling is slowed upon entering the high-density peak [16].

Besides superconductivity and chemical potential pinning, this model was used to explain a number of observations including a mobility drop due to resonant scattering [16, 22], enhanced electronic heat capacity from the impurity band [48], and resonant state peaks in the optical absorption [49]. The applicability of the charge Kondo model compared to the resonant impurity band model will be discussed in later chapters (Chapters 6 and 7). As we will see from observations in this thesis, an impurity band model

alone cannot explain the anomalous low-temperature transport properties, especially a charge Kondo effect, in this material.

Chapter 4

Electronic transport parameters and density of states from Hall effect and heat capacity measurements

The doping dependence of various transport properties can be determined using the known electronic band structure of PbTe to analyze the low-temperature Hall effect and resistivity data. Hall effect measurements for each Tl concentration gives the carrier densities and Fermi level position in the valence band. We can then use the resistivity of each sample to obtain values of hole mobility, mean free path, and density of states as a function of Tl doping. These parameters are used in later analysis of superconducting

parameters and normal state transport properties. It is assumed in this analysis that the underlying band structure is not affected by Tl doping, as also assumed by previous work on Hall effect [50, 51] and specific heat [52]. It is further assumed that the Pb vacancy concentration does not significantly change with Tl doping. In the absence of any contrary information, this is a reasonable starting point since the hole concentration of $\sim 10^{18}$ cm^{-3} due to Pb vacancies in the undoped samples is significantly less than the typical concentrations for Tl doped samples.

4.1 Hall coefficient calculation

The Hall effect is a common measurement used to estimate the carrier concentration of a material. While applying a magnetic field B_z along the z-direction with an applied current J_x along x, one can measure the transverse voltage V_H along y due to the electric field E_y where $V_H = R_H IB/d$ and d is the thickness of the sample. The Hall coefficient R_H is given by $R_H = 1/en_H$ where the Hall number n_H is exactly the carrier concentration for the case of one carrier type and a spherical Fermi surface. For multiple carrier types with different mobilities and anisotropic Fermi surfaces, a more explicit expression for the Hall coefficient is needed.

More precisely, the Hall coefficient is

$$R_H = \frac{E_y}{J_x B_z} = \frac{\rho_{xy}}{B_z} = \frac{\sigma_{xy}}{B_z(\sigma_{xx}^2 + \sigma_{xy}^2)} \simeq \frac{\sigma_{xy}}{B_z \sigma_{xx}^2}, \tag{4.1}$$

where the conductivity tensor σ_{ij} can be derived from the semiclassical transport expression using the relaxation time approximation. Using a two-band model where the two carrier types in this case are the light holes in the L band and the heavy holes in the Σ band and taking into account the orientation of the Fermi surfaces (see Fig. 3.2) and their anisotropic masses, Eq. 4.1 becomes

$$R_H = \frac{a^2 12 p_\Sigma M_{\Sigma 1} + 4 p_L M_{L1}}{e(a 12 p_\Sigma M_{\Sigma 2} + 4 p_L M_{L2})^2}, \tag{4.2}$$

where the ratio of the relaxation times is

$$a = \tau_\Sigma / \tau_L \tag{4.3}$$

and where the effective mass terms are

$$M_{\Sigma 1} = \frac{3}{m_{\Sigma t}} \left(\frac{1}{m_{\Sigma t}} + \frac{2}{m_{\Sigma l}} \right), \tag{4.4a}$$

$$M_{\Sigma 2} = \frac{2}{m_{\Sigma t}} + \frac{1}{m_{\Sigma l}}, \tag{4.4b}$$

$$M_{L1} = \frac{3}{m_{Lt}} \left(\frac{2}{m_{Ll}} + \frac{1}{m_{Lt}} \right), \tag{4.4c}$$

$$M_{L2} = \frac{1}{m_{Ll}} + \frac{2}{m_{Lt}}. \tag{4.4d}$$

In the limit where the effective masses are isotropic (i.e., $m_{Lt} = m_{Ll}$ and $m_{\Sigma t} = m_{\Sigma l}$),

Eq. 4.2 reduces to the familiar expression for the Hall coefficient of a two-band semiconductor

$$R_H = \frac{p_L \mu_L^2 + p_\Sigma \mu_\Sigma^2}{e(p_L \mu_L + p_\Sigma \mu_\Sigma)^2}, \tag{4.5}$$

where the mobilities are

$$\mu_L = e\tau_L/m_L, \tag{4.6a}$$

$$\mu_\Sigma = e\tau_\Sigma/m_\Sigma. \tag{4.6b}$$

Given the isotropic crystal structure, we roughly approximate the average masses m_L and m_Σ as their respective average conductivity mass from the expression

$$\frac{3}{m_{\text{cond}}} = \frac{2}{m_t} + \frac{1}{m_l}, \tag{4.7}$$

such that $m_L = 0.032 m_0$ and $m_\Sigma = 0.14 m_0$. Eq. (4.2) accounts for the 4 L pockets and 12 Σ pockets where the carrier densities per pocket as a function of Fermi level E_F are

$$p_L = \frac{2^{3/2} m_{Lt} m_{Ll}^{1/2}}{3\pi^2 \hbar^3} E_F^{3/2}, \tag{4.8a}$$

$$p_\Sigma = \frac{2^{3/2} m_{\Sigma t} m_{\Sigma l}^{1/2}}{3\pi^2 \hbar^3} (E_F - \Delta E_v)^{3/2}, \tag{4.8b}$$

and are approximated assuming parabolic band dispersion. For p_Σ, the valence band offset $\Delta E_v = 170$ meV.

From Eq. (4.2) we now see that, while we ultimately wish to know the carrier concentrations p_L and p_Σ, the measurement only gives one number R_H. In addition, the relaxation times and their ratio a have yet to be determined. It is necessary to calculate these parameters in a self-consistent manner by combining the Hall effect expression with band parameter and transport assumptions. By doing this, we can obtain expressions of all parameters in terms of E_F.

We start by assuming that the elastic scattering limit holds for measurements taken at 1.8 K. At low temperatures, inelastic phonon scattering becomes negligible, such that the mean free path l is only limited by elastic scattering from defects and impurities. With this assumption, we can apply the constraint that l is isotropic and $l_L = l_\Sigma = l$ for these low-temperature measurements. The mean free path is related to the relaxation time by

$$l = v_F \tau. \tag{4.9}$$

The average Fermi velocity for L carriers is

$$v_F = \sqrt{\frac{2E_F}{m_L}} \tag{4.10}$$

and for Σ carriers is

$$v_F = \sqrt{\frac{2(E_F - \Delta E_v)}{m_\Sigma}}, \tag{4.11}$$

where ΔE_v is the valence band offset. The elastic scattering limit now requires

$$\sqrt{\frac{2E_F}{m_L}}\tau_L = \sqrt{\frac{2(E_F - \Delta E_v)}{m_\Sigma}}\tau_\Sigma, \tag{4.12}$$

and the expression for a in terms of the Fermi energy is

$$a(E_F) = \sqrt{\frac{E_F m_\Sigma}{(E_F - \Delta E_v)m_L}}. \tag{4.13}$$

Finally, we combine Eq. (4.13) with the expressions for p_L and p_Σ from Eq. (4.8a) and R_H in Eq. (4.2). Now, $R_H(E_F)$ is only a function of E_F and known effective masses. In this way, each sample's measured R_H corresponds to a value of E_F and subsequently to specific values of p_L, p_Σ, v_F, and l.

4.2 Hall effect results and transport parameters

The data at 1.8 K for the Hall coefficient R_H as a function of Tl concentration x is shown in Fig. 4.1. The positive values of R_H confirm the presence of hole carriers in our vapor-grown crystals of both undoped and Tl-doped PbTe. The corresponding data for E_F based on the analysis described above are plotted as symbols in Fig. 4.2. For comparison, $E_F(x)$ can also be calculated assuming that each Tl contributes one hole in the valence band. In other words, if we assume the Tl concentration is the same as the total hole concentration $p_{\text{tot}} = 4p_L + 12p_\Sigma$, we can calculate $E_F(x)$ based on known PbTe band parameters as shown in Fig. 4.2 as the solid line. The theoretical calculation

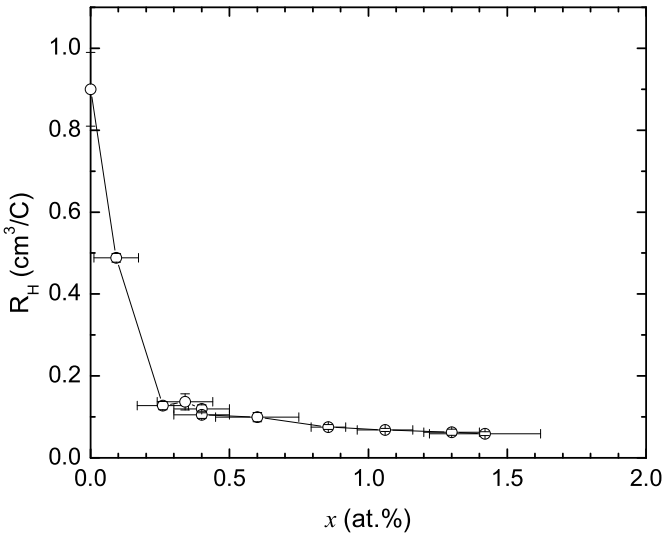

Figure 4.1: Hall coefficient R_H as a function of Tl concentration x measured at 1.8 K.

shows the Fermi level initially increasing rapidly with x due to the light mass of the L band and then increasing at a slower rate after entering the Σ band containing heavier holes. As can be seen, the measured values of E_F appear lower than the calculated line beyond about $x = 0.3\%$. This indicates that something has slowed the band filling in this material.

The Hall number $p_H = 1/R_H e$ and corresponding hole concentration $p_{\rm tot}$ are shown as symbols in Fig. 4.3. It turns out that p_H does not differ much from the actual $p_{\rm tot}$ since the mobilities of the two bands are very similar in the elastic limit as has been observed elsewhere [15, 16, 50]. This is due to the fact that the heavy holes have smaller velocities and longer scattering times, while the light holes have larger velocities but shorter scattering times. As above for E_F, the solid line represents the calculated

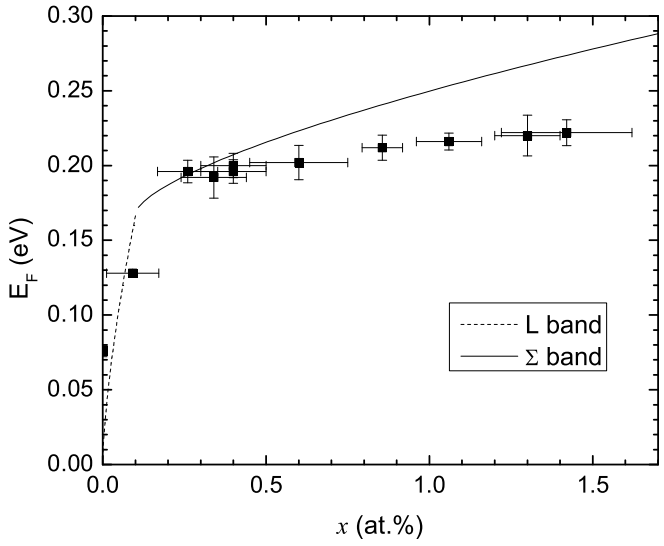

Figure 4.2: Fermi level E_F as a function of Tl concentration x at 1.8 K. Solid line represents calculated $E_F(x)$ for theoretical doping of one hole to valence band per Tl.

values of $p_H(x)$ from band filling effects assuming a carrier doping of one hole per Tl. For Tl concentrations beyond a critical value near 0.3%, p_H begins to strongly deviate from the calculated values and appears to rise at a much slower rate with x while not increasing beyond $\sim 10^{20}$ cm^3. This behavior was also observed elsewhere at 77 K for polycrystalline material [16], single crystals [23], and thin films [22].

The saturation of the carrier concentration is evidence for the emergence of the Tl mixed valence state. For low Tl doping and small E_F, the data shows p_H rapidly increasing and follows that expected for Tl^+ doping of one hole per Tl. Our data is consistent with previous work which have carefully shown data in this region below $x = 0.3\%$ [16, 22, 23]. Beyond a critical concentration $x^* \sim 0.3\%$, the data suggest that the Tl impurities act in a self-compensating manner. One interpretation of this behavior is the emergence of a Tl mixed valence state where Fermi level pinning (Fig. 4.2), or at

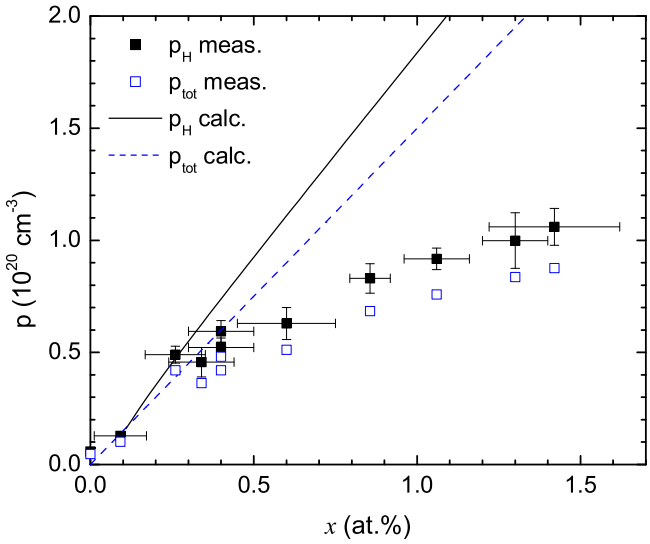

Figure 4.3: Hall number $p_H = 1/R_H e$ and hole concentration $p_{\rm tot}$ as a function of Tl concentration x at 1.8 K. Solid and dashed lines are $p_H(x)$ and $p_{\rm tot}$ calculated for theoretical doping of one hole per Tl.

least reduced filling, occurs and the Tl form a self-compensating mixture of Tl^{+} acceptors and Tl^{3+} donors as described in the negative-U picture. An alternative argument is that the impurities form a third, low-mobility band as described in Section 3.6. While the Hall data alone cannot distinguish between these two models, the subsequent chapters describe transport anomalies for $x > 0.3\%$ that indicate that a simple impurity band model is unlikely the case.

Using Eqs. (4.10) and (4.11), we estimate the average Fermi velocities shown in Fig. 4.4 as a function of x. Due to the cubic structure, transport properties are nearly isotropic despite the anisotropic Fermi surfaces. The average transport masses m_L and m_Σ are approximated as the conductivity effective masses defined in Eq. 4.7. The heavier Σ mass results in a v_F for the Σ band almost an order of magnitude smaller than for the

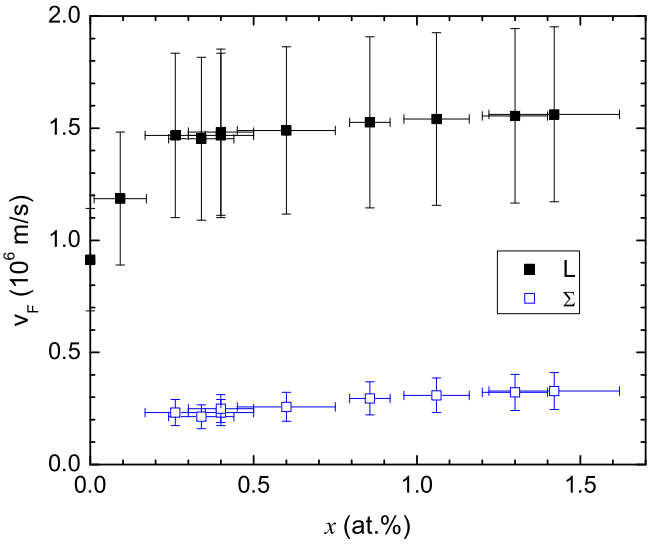

Figure 4.4: Fermi velocity v_F as a function of Tl concentration x at 1.8 K. Closed symbols are for L band, and open symbols are for Σ band.

L band.

Resistivity measurements were combined with the Hall effect data to obtain relaxation times, mobility, and mean free paths. The resistivity is given by

$$1/\rho = \sigma = \frac{p_L e^2 \tau_L}{m_L} + \frac{p_\Sigma e^2 \tau_\Sigma}{m_\Sigma}, \tag{4.14}$$

where p_L and p_Σ were determined from the Hall effect measurements. Combining Eq. 4.14 with Eq. 4.13 and 4.6a, we obtain estimates of the mobilities as shown in Fig. 4.5 as a function of x. Both μ for each band are close to the Hall mobility $\mu_H = R_H/\rho$, except for the data for $x = 0.1\%$. The discrepancy in this sample reflects the uncertainty in the band offset ΔE_v and therefore the exact Tl concentration at which E_F enters the Σ band. The mean free path l estimated from Eq. (4.9) is shown in Fig. 4.6 for the various

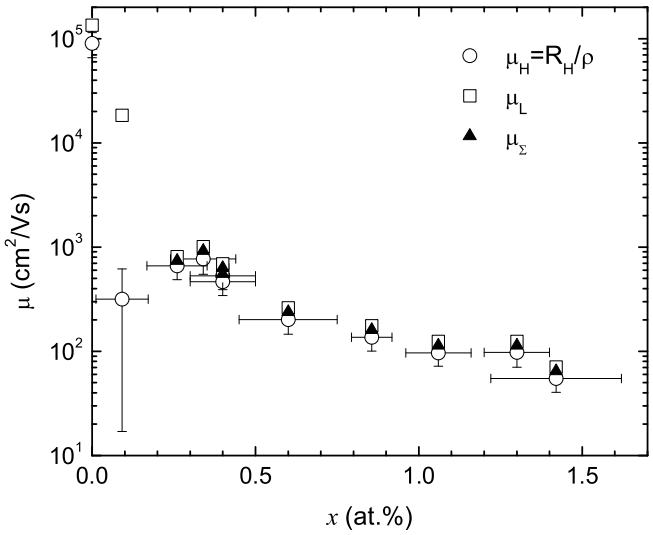

Figure 4.5: Mobility as a function of Tl doping x for the L and Σ bands. Values are near the Hall mobility $\mu_H = R_H/\rho$. Since the $x = 0.1\%$ sample is near the Σ band edge, the large difference from μ_H reflects the uncertainty in the concentration at which E_F enters the Σ band.

samples. l is as high as 2 μm for the undoped PbTe and drops with increasing x to only 19 Å for $x = 1.4\%$.

4.3 Density of states from heat capacity measurements

As a consequence of the carrier concentration saturation above the critical value $x^* \sim 0.3\%$, the total hole density $p_{\rm tot}$ does not equal the total Tl concentration x. As a result, the actual valence band filling as a function of x is not the same as if every Tl contributed one hole to the valence band. Consequently, the density of states as a function of x for the two cases are also not the same and should be taken into account when analyzing measurements that depend on $N(0)$ such as heat capacity and later calculations of superconducting and transport parameters.

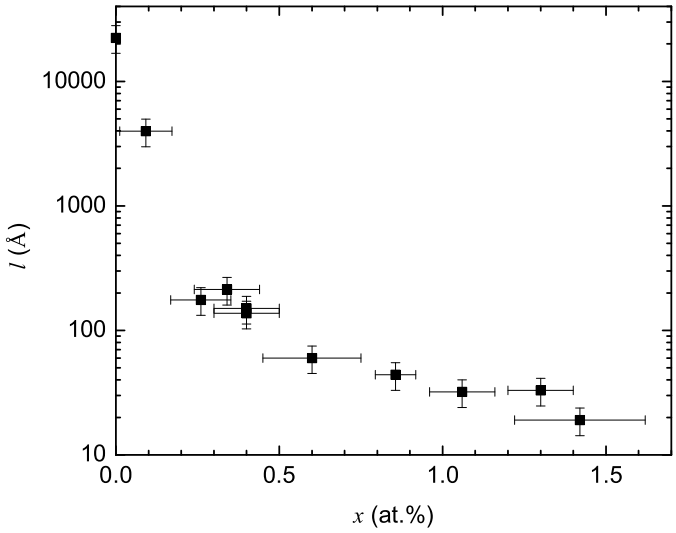

Figure 4.6: Estimates of mean free path l as a function of Tl concentration x at 1.8 K.

The density of states can be measured from the electronic contribution γ to the heat capacity, where the low-temperature heat capacity C_p is given by

$$C_p/T = \gamma + \beta T^2, \tag{4.15}$$

where βT^2 is the phonon contribution. The density of states at the Fermi energy $N(0)$ can be estimated from γ using

$$\gamma = \frac{\pi^2}{3} k_B^2 N(0), \tag{4.16}$$

where spin degeneracy is included.

Heat capacity data for representative Tl concentrations are shown in Fig. 4.7 as C_p/T versus T^2 for applied fields that totally suppress the superconductivity. For all samples there is a slight curvature in the data even at low temperatures. This curvature was

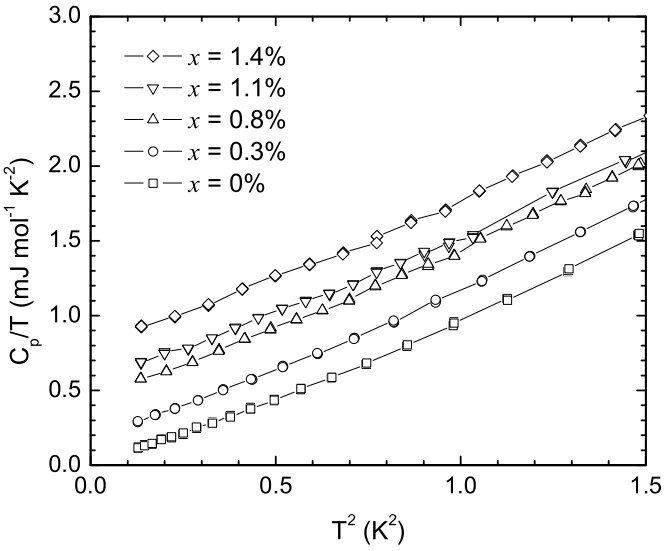

Figure 4.7: Measured heat capacity of $Pb_{1-x}Tl_xTe$ single crystals, shown as C_p/T versus T^2, for representative Tl concentrations. For superconducting samples, data were taken in an applied field H=0.5–1 T $> H_{c2}$.

observed previously for undoped PbTe samples and was attributed to possible softening of transverse optical phonon modes [53]. Data for Tl-doped PbTe samples are essentially parallel to those for undoped samples indicating that the phonon contribution is not affected by Tl substitution and that reasonable comparisons of the electronic contribution can be made between different doping concentrations [54]. Data were fit to $C/T = \gamma + \beta T^2 + \delta T^4$ from the base temperature (0.3 K) up to 1 K. From $\beta = N(12\pi^4/5)R\Theta^{-3}$, where $R = 8.314$ J/(mol K) and $N = 2$ for PbTe, we estimate $\Theta_D = 168 \pm 4$ K for $x = 0\%$, which is consistent with previous reports [17, 53]. Thallium substitution does not substantially affect this value but causes a clear increase in γ, suggesting a rapid rise in the density of states with x. Values of γ obtained from the above fits are shown as a function of Tl concentration x in Fig. 4.8, with the corresponding values for $N(0)$

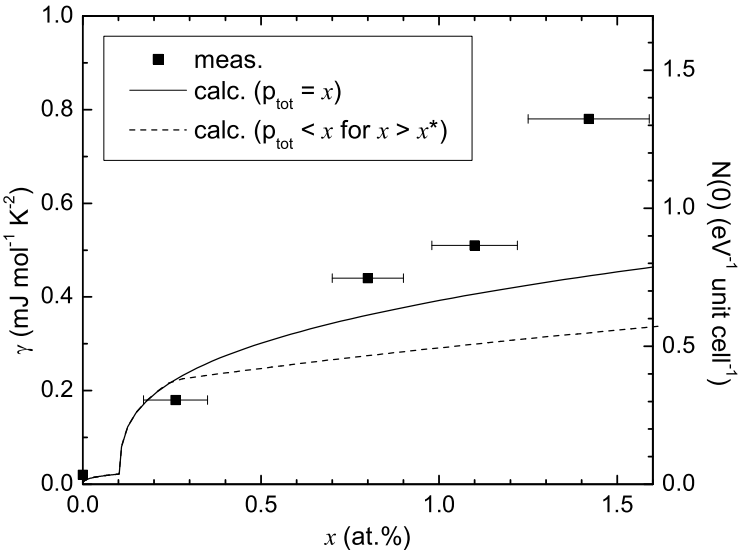

Figure 4.8: Electronic heat capacity γ (left axis) and density of states $N(0)$ (right axis) for Tl-doped PbTe as a function of Tl concentration x. Solid line is calculated from known PbTe band parameters and assuming $p_{\rm tot} = x$ where every Tl contributes one hole to the valence band. Dashed line is calculated from measured Hall effect data, where $p_{\rm tot} < x$ for $x > x^*$ due to carrier concentration saturation. The rapid increase in calculated values of γ at $\sim 0.1\%$ corresponds to the chemical potential entering the heavier Σ band.

included on the right axis. These data are in broad agreement with previously published values for polycrystalline samples [52].

Given the band structure of PbTe from Section 3.1 and assuming that the Tl doping does not alter these parameters [50, 51], we can calculate the density of states at the Fermi level $N(0)$ for each valence band from

$$N_L(0) = \frac{2^{1/2} m_{Lt} m_{Ll}^{1/2}}{\pi^2 \hbar^3} E^{1/2}, \tag{4.17a}$$

$$N_\Sigma(0) = \frac{2^{1/2} m_{\Sigma t} m_{\Sigma l}^{1/2}}{\pi^2 \hbar^3} (E - \Delta E_v)^{1/2}, \tag{4.17b}$$

where parabolic bands are assumed. Since there are 4 L pockets and 12 Σ pockets, the total density of states is

$$N(0) = 4N_L + 12N_\Sigma \tag{4.18}$$

The solid line in Fig. 4.8 is $N(0)$ calculated as a function of $x = p_{\rm tot}$ if every Tl contributed one hole. The rapid increase at $\sim 0.1\%$ corresponds to the chemical potential entering the heavier Σ band. However, Fig. 4.2 shows that the measured $E_F(x)$ deviates from the calculated $E_F(x)$ due to the carrier saturation beyond $x \sim 0.3\%$. Using the measured values of $E_F(x)$ in Eq. 4.18, we obtain $N(0)$ as the dashed line in Fig. 4.8 since $p_{\rm tot} < x$ for $x > x^*$.

We see that the $N(0)$ corrected for carrier concentration saturation is substantially less than for purely acceptor doping. Furthermore, the measured values of γ from heat capacity increase rapidly above the calculated density of states beyond a concentration near the critical concentration for superconductivity $x_c \sim 0.3\%$. Such a feature in the density of states is consistent with an impurity band due to Tl impurities [16, 22]. However, an enhancement of the density of states can also appear due to other effects, including a Kondo effect. In subsequent Chapters, we see that an anomalous normal state resistivity in Tl-doped PbTe cannot be easily interpreted in terms of a simple impurity band model.

Chapter 5

Superconducting Properties

The first study of superconductivity in Tl-doped PbTe by Chernik and Lykov [21] was on polycrystalline material. Evidence for bulk superconductivity was observed as a jump in the heat capacity and a resistivity transition at 1.4 K for 1.5% Tl. The authors estimated the upper critical field $H_{c2} \sim 5000$ Oe, the coherence length $\xi(0) \sim 350$ Å, and the Ginzburg-Landau parameter $\kappa \sim 82$, indicating Type II superconductivity. Further studies of the the heat capacity were presented as evidence for resonant Tl states in the density of states [33, 48, 52].

As described in Chapter 1, Tl-doped PbTe has a remarkably high T_c when compared to similar superconducting semiconductors. In light of the anomalous appearance of superconductivity in this material, we have systematically investigated the superconducting properties of single crystal samples for a range of Tl concentrations up to the solubility limit of 1.5%. In particular, T_c for low Tl concentrations was measured down to 13 mK for the first time, revealing a critical concentration for superconductivity. In

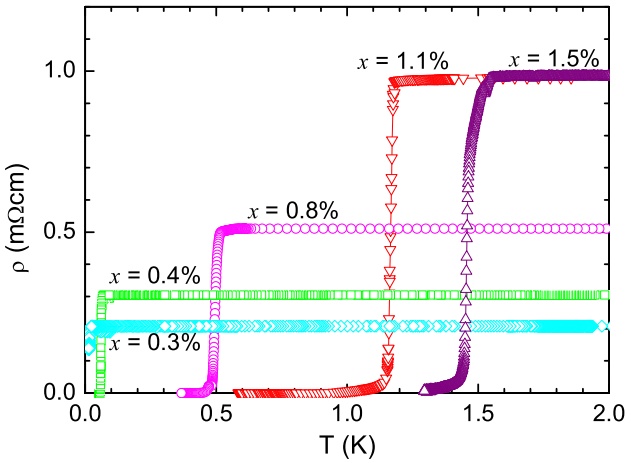

Figure 5.1: Representative resistivity data for single crystal $Pb_{1-x}Tl_xTe$ showing sharp superconducting transitions.

this chapter, we present measurements of the heat capacity and H_{c2} and the resulting estimates for coherence length, penetration depth, Ginzburg-Landau parameter, and critical fields.

5.1 Superconducting parameters from H_{c2} and electronic transport

Low-temperature electrical resistivity was measured in a ^{3}He refrigerator or a dilution refrigerator as described in Section 2.3. Representative data in Fig. 5.1 show sharp superconducting transitions. The critical temperature T_c was estimated from the midpoints of the superconducting transitions and are shown in Fig. 5.2 as a function of Tl content. The error bars indicate the width of the transition estimated by the difference

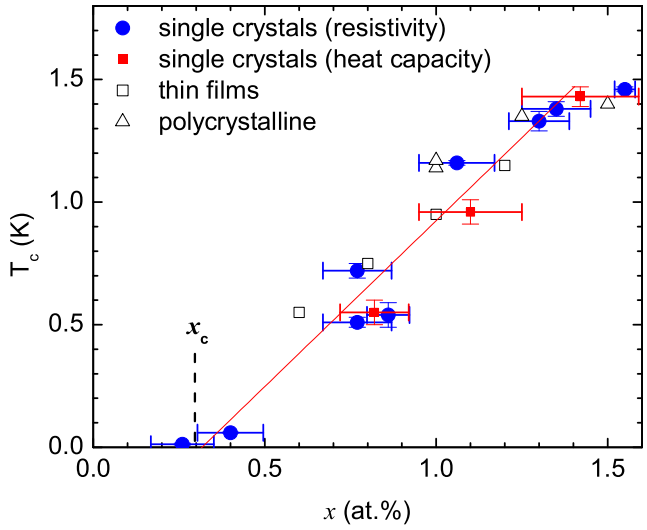

Figure 5.2: Variation of T_c with Tl content x. Line shows linear fit to single crystal data. Data for thin films and polycrystalline samples were taken from Ref. [22] and Ref. [21], respectively. A critical Tl concentration $x_c \sim 0.3\%$ is observed below which the material does not superconduct.

in temperature between 10% and 90% of the resistive transition. Our T_c values for single crystals agree well with published data for polycrystalline samples [21] and for thin films [22]. Of particular importance is the data from our lowest Tl concentrations, which indicate that there is a critical concentration of $\sim 0.3\%$ below which the material does not superconduct above 20 mK.

The upper critical field $H_{c2}(T)$ was determined from resistivity measurements in an applied field. Two Tl concentrations were studied for which the suppression of the resistive transition in a field could be observed over an appreciable range of temperature. Representative data are shown in Fig. 5.3 for $x = 1.4\%$. An estimate of T_c was obtained from the midpoint of the resistive transition for each applied field. Resulting H_{c2} curves

are shown in Fig. 5.4 for $x = 1.1\%$ and 1.4%. Error bars indicate the width of the superconducting transition measured by the difference in temperature between 10% and 90% of the resistive transition. The upper critical field at zero temperature $H_{c2}(T = 0)$ can be estimated from these data using the Werthamer-Helfand-Hohenberg approximation [55]

$$H_{c2}(0) = 0.69(dH_{c2}/dT)_{T_c}T_c. \tag{5.1}$$

Resulting values for $x = 1.1\%$ and 1.4% are approximately 3900 ± 400 Oe and 6000 ± 700 Oe, respectively (Table 5.1) and are consistent with reasonable extrapolations of the lowest temperature data in Fig. 5.4 and previous reports [16]. The errors in $H_{c2}(0)$ are estimated from the difference between the above approximation and a parabolic fit to the observed data.

Superconducting parameters such as the coherence length and penetration depth are dependent on the electron mean free path $l = v_F\tau = v_F\mu m^*/e$, where v_F is the Fermi velocity and μ is the hole mobility. From Hall effect and resistivity measurements at 1.8 K and following the analysis outlined in Section 4.2, we find $l = 32 \pm 8$ Å for $x = 1.1\%$ and $l = 19 \pm 5$ Å for $x = 1.4\%$ as listed in Table 5.1. The principle contribution to the uncertainty in this quantity arises from errors in the geometric factor used to calculate the resistivity of these samples. Propagation of this error is the dominant effect in the uncertainties of subsequent derived quantities, including ξ_0 and λ_{eff}.

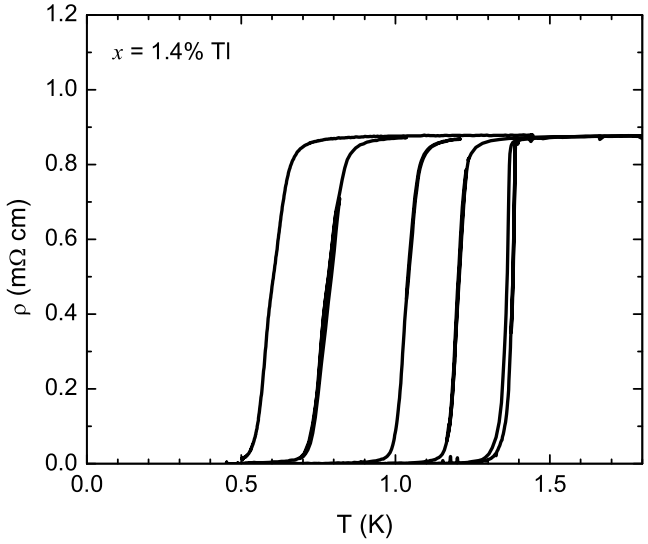

Figure 5.3: Representative resistivity data for $x = 1.4\%$, showing the superconducting transition as a function of temperature for different magnetic fields (0, 108, 1083, 2166, 3791, and 4875 Oe) applied parallel to the [001] direction.

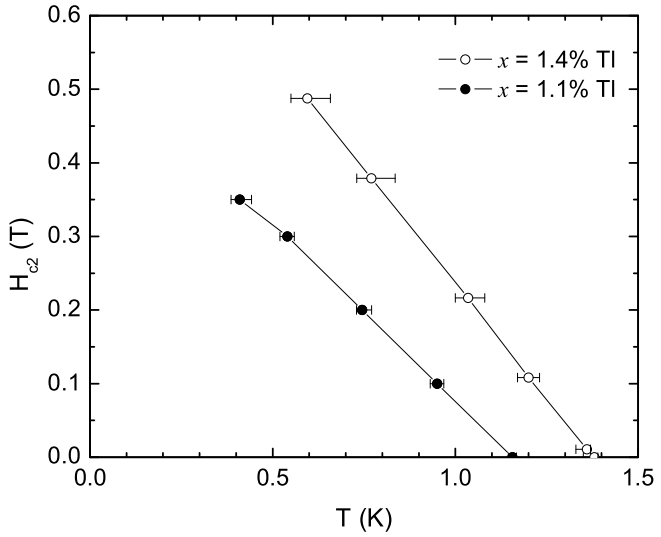

Figure 5.4: Temperature dependence of H_{c2} for $x = 1.1\%$ and 1.4% with the field parallel to the [001] direction. Error bars were determined as described in the main text. Lines are drawn to guide the eye.

The Ginzburg-Landau coherence length $\xi(0)$ is calculated from $H_{c2}(0)$ by

$$H_{c2}(0) = \frac{\Phi_0}{2\pi\xi^2(0)}, \tag{5.2}$$

where $\Phi_0 = 2.0678 \times 10^{-15}$ T m^2 is the flux quantum. Estimates for $\xi(0)$ are 290 ± 15 Å for $x = 1.1\%$ and 240 ± 14 Å for $x = 1.4\%$ (Table 5.1) and should be independent of orientation for this cubic material. These values are also in broad agreement with previous measurements for polycrystalline material [21]. The small values of l imply that the material is in the dirty limit with $l < \xi_0$. Therefore the intrinsic coherence length ξ_0 can be extracted from the approximation $\xi(0) \sim (l\xi_0)^{1/2}$, where the values are listed in Table 5.1. In comparison, the BCS expression for ξ_0 is

$$\xi_0 = \frac{\alpha\hbar v_F}{k_B T_c}, \tag{5.3}$$

where the BCS value of α is 0.18. Using values of ξ_0 derived from the dirty limit approximation, we find v_F estimated from this formula (given in Table 5.1) is between those calculated separately for the L and Σ holes. This is consistent with a mixed contribution from both carrier types due to the substantial scattering implied from the short mean free path.

The London penetration depth for two carrier types is given by

$$\frac{1}{\lambda_L^2} = \frac{\mu_0 p_L e^2}{m_L} + \frac{\mu_0 p_\Sigma e^2}{m_\Sigma}, \tag{5.4}$$

where the superfluid densities are approximated as the hole carrier densities p_L and p_Σ for each carrier type, and m_L and m_Σ are the effective masses of each band. The corresponding values of λ_L are listed in Table 5.1 and are almost independent of orientation. In the dirty limit, we can estimate the effective penetration depth from

$$\lambda_{\text{eff}} = \lambda_L(\xi_0/l)^{1/2}, \tag{5.5}$$

values of which are given in Table 5.1. These estimates are in good agreement with microwave conductivity measurements obtained by R. J. Ormeno, P. J. Baker, and C. E. Gough at the University of Birmingham, which show $\lambda(0) \sim$ 2–3 μm for $x = 1.4\%$ [56]. The measured temperature dependence of this parameter appears to follow a BCS temperature dependence (Fig. 5.5). Finally, we find the Ginzburg-Landau parameter using $\kappa = \lambda_{\text{eff}}/\xi(0)$ and estimate the thermodynamic critical field H_c and the lower critical field H_{c1} from the relationships $H_{c2} = \sqrt{2}\kappa H_c$ and $H_{c1} = \frac{H_c}{\sqrt{2}\kappa} \ln \kappa$ (Table 5.1).

5.2 Heat capacity

Heat capacity data in zero field are shown in Fig. 5.6 for representative Tl concentrations with T_c above 0.3 K. T_c values were obtained from the midpoint of the heat capacity anomaly and agree well with data obtained from resistive transitions (Fig. 5.2). The jump at T_c, ΔC, can be estimated using a standard geometric construction extrapolating normal state and superconducting state behaviors towards T_c, as indicated by dashed lines for $x = 1.4\%$ in Fig. 5.6. Resulting estimates of $\Delta C/\gamma T_c$, where γ is obtained

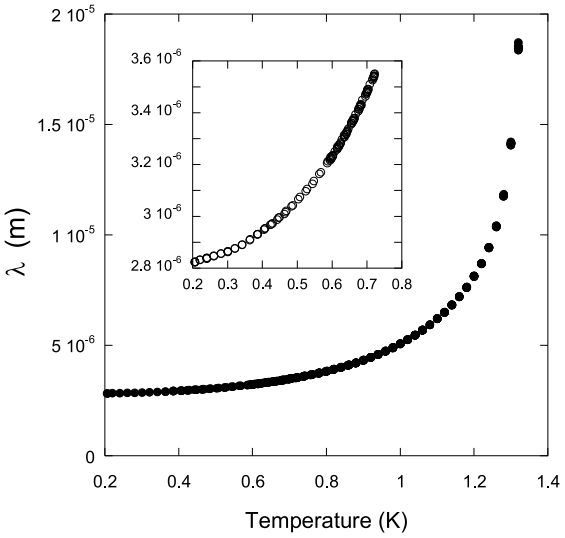

Figure 5.5: Temperature dependence of the penetration depth measured by microwave conductivity measurements of a sample with $x = 1.4\%$ from Ref. [56].

Table 5.1: Superconducting parameters of $Pb_{1-x}Tl_xTe$ for two representative Tl concentrations.

	$x = 1.1 \pm 0.1$ at.%	$x = 1.4 \pm 0.1$ at.%
T_c	1.16 ± 0.01 K	1.38 ± 0.03 K
$H_{c2}(0)$	0.39 ± 0.04 T	0.60 ± 0.07 T
l	32 ± 8 Å	19 ± 5 Å
$\xi(0)$	290 ± 15 Å	240 ± 14 Å
ξ_0	2600 ± 700 Å	3000 ± 850 Å
v_F	$2.2 \pm 0.6 \times 10^5$ m/s	$3.0 \pm 0.8 \times 10^5$ m/s
λ_L	1600 ± 80 Å	1500 ± 120 Å
λ_{eff}	1.4 ± 0.4 μm	1.9 ± 0.5 μm
κ	48 ± 12	79 ± 20
H_c	57 ± 14 Oe	54 ± 13 Oe
H_{c1}	3 ± 0.8 Oe	2 ± 0.5 Oe

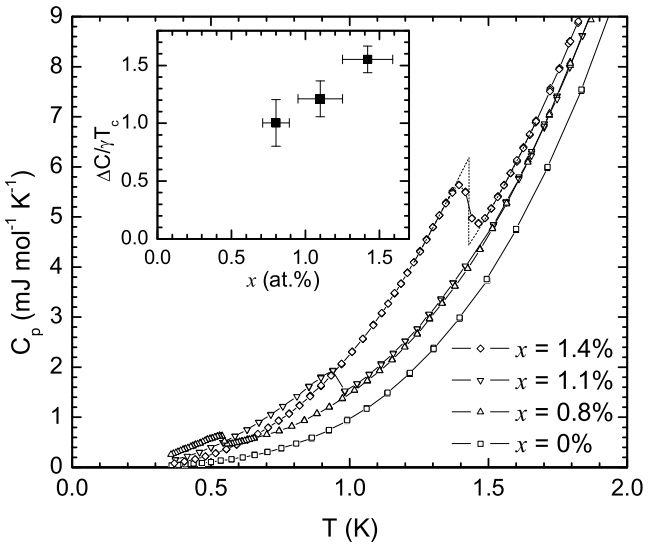

Figure 5.6: C_p versus T in zero applied field showing the superconducting anomaly for several Tl concentrations x. Dashed lines show the geometric construction used to obtain ΔC and T_c for $x = 1.4\%$. Inset shows $\Delta C/\gamma T_c$ as a function of x. Uncertainty in $\Delta C/\gamma T_c$ is derived principally from errors in the geometric construction used to estimate ΔC.

from Fig. 4.8, are shown in the inset to Fig. 5.6 as a function of Tl concentration x. The value for the highest Tl concentration, $x = 1.4\%$, is $\Delta C/\gamma T_c = 1.55 \pm 0.12$, which is close to the weak coupling BCS result of 1.43. As x is reduced, the data show a small but significant systematic variation, tending towards a smaller value for smaller Tl concentrations. The smallest value, 1.00 ± 0.20, is recorded for $x = 0.8\%$, which is the lowest Tl concentration for which we can confidently extract ΔC given the base temperature of our instrument.

Given that the above observations are consistent with a BCS scenario, we may characterize T_c in terms of the BCS expression where T_c varies exponentially with $-1/N(0)V$, and V is the pairing interaction. Figure 5.7 shows $\ln(T_c)$ versus $1/\gamma$ for samples with

$x > x_c$. For samples with $T_c > 0.5$ K, both parameters were extracted from the same physical crystal. However, for samples with a lower critical temperature, T_c was determined from resistivity measurements on different crystals from the same growth batch, introducing additional errors due to uncertainty in the Tl concentration. As can be seen, $\ln(T_c)$ scales approximately linearly with $1/\gamma$ within the uncertainty of the measurements. For a constant V, these data imply that increasing $N(0)$ with increasing x contributes towards the observed trend in T_c. However, it is difficult to fully account for such a large increase in T_c with increasing x only with $N(0)$ and small values for the coupling. Furthermore, the observed trend does not rule out a possibly significant role of the pre-exponential factor in the BCS expression for T_c nor a possibly changing V. Either scenario may indicate additional physics coming into play for superconductivity in this material, and further investigations are necessary to determine the applicability of the weak-coupled model in this system.

5.3 Effects of high presssures on superconductivity

To further understand the mechanisms possibly involved in the superconductivity of this material, the effect of hydrostatic pressures on T_c was also investigated following the techniques described in Section 2.6. Superconducting transitions were measured from the midpoint of the resistive transitions at different applied pressure. T_c versus pressure is plotted in Fig. 5.8 for $x = 0.8\%$ and 1.5%. Error bars correspond to the width of the transition between 10% and 90% of the resistive transition. The error in applied pressure

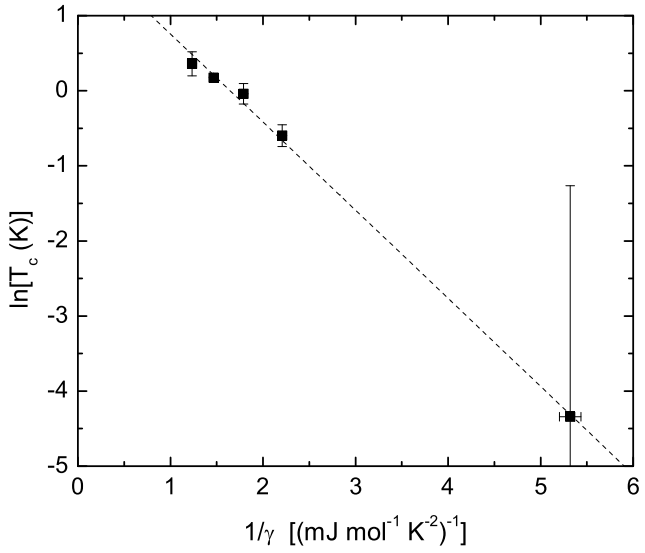

Figure 5.7: Plot of $\ln(T_c)$ vs. $1/\gamma$. Dashed line is a guide for the eye.

is estimated as a calibration uncertainty from the method described in Section 2.6. For both samples, T_c monotonically decreases with increasing pressure. This is consistent with most low-temperature superconductors and may indicate that the T_c is responding to a decrease in the density of states in a weak-coupled, BCS model. An analysis of the pressure dependence of the transport properties presented in Section 6.6 may provide further information about the behavior of T_c in the context of the charge Kondo model proposed earlier (Section 3.5).

5.4 Summary of superconducting properties

The above results indicate that Tl-doped PbTe is a Type II, BCS superconductor in the dirty limit, which is not too surprising given that the material is a doped semiconductor.

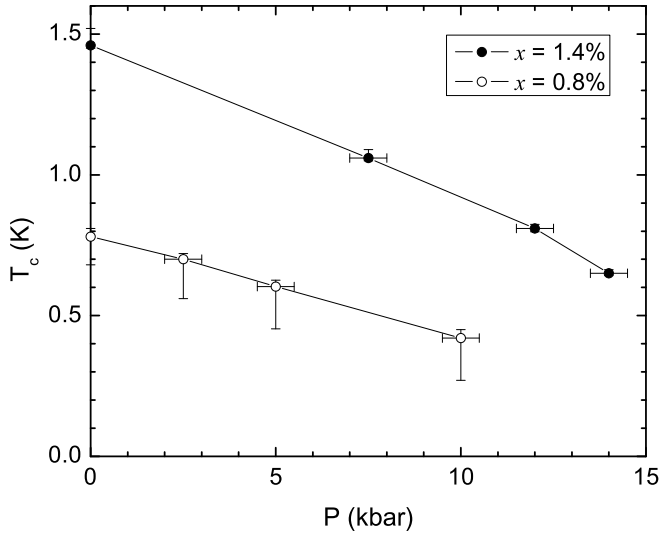

Figure 5.8: Pressure dependence of T_c for $x = 0.8\%$ and $x = 1.5\%$.

To a large extent this observation rules out the possibility of more exotic scenarios for the superconductivity, such as condensation of preformed pairs, at least for the highest Tl concentrations. The data also show that T_c appears to follow a BCS dependence on the density of states. However, the contributions to $N(0)$ besides the underlying band structure may come from other sources that will be discussed in Chapter 7. A significant feature in the superconducting properties of Tl-doped PbTe is the critical Tl concentration $x_c \sim 0.3\%$ at which superconductivity emerges (Fig. 5.2). Within the uncertainty of the measurements, x_c is the same as x^*, the characteristic concentration beyond which the carrier density begins to saturate. It is remarkable that as x is increased beyond x_c, T_c rises linearly over two orders of magnitude from 13 mK for $x \sim 0.3\%$ to 1.5 K for $x \sim 1.5\%$, while the hole concentration appears to be approaching saturation

and varies by less than a factor of two. Clearly the Tl impurities are intimately linked to the superconductivity in this material. In order to understand the possible link to the presence of a mixed Tl valence state, the effect of Tl doping on the normal state properties is investigated in the next chapter.

Chapter 6

Normal state properties and evidence for charge Kondo effect

In Chapter 4, we have interpreted a carrier concentration saturation in the Hall effect measurements as evidence for the emergence of a mixed valence state beyond a critical Tl concentration $x_c \sim 0.3\%$. However, carrier concentration saturation and chemical potential pinning have been associated with other scenarios, like resonant impurity bands [15,16] or defect compensation in doped semiconductors [57]. In an impurity band model, the impurity states form a narrow band of impurity states with very low mobility. The result is a narrow peak in the density of states that pins the chemical potential at the impurity band as the peak grows with increasing impurity concentration. A low-mobility band would hardly contribute to the Hall number, resulting in a saturation as the chemical potential enters the band.

This chapter presents the temperature and field dependence of the thermodynamic and transport properties of Tl-doped PbTe in the normal state. The data suggest anomalous resistivity and transport behavior that is not easily explained by a simple impurity band description. In particular, samples with $x > x_c$ exhibit a Kondo-like low-temperature resistivity upturn. We show that this effect is not associated with magnetic impurities and is not easily described by weak localization. These observations can be interpreted as evidence for the charge Kondo effect proposed in Section 3.5, supporting the suggestion that the superconductivity in Tl-doped PbTe is intimately associated with the presence of a mixed Tl valence.

6.1 Zero-field resistivity

As Hall effect measurements have shown (Fig. 4.3), crystals with $x = 0\%$ grown by our physical vapor transport technique have a hole concentration of approximately 10^{18} cm^{-3} due to the presence of a small concentration of Pb vacancies. The resistivity of these samples [$x = 0\%$ curve in Fig. 6.1(a)] is characteristic of metallic behavior. The observation of quantum oscillations in the magnetoresistance of the undoped samples indicates a well-formed Fermi surface. Such behavior has been observed previously and is attributed to the large dielectric constant of PbTe which screens defects and allows for large mobilities [17, 18].

Upon doping with Tl, the temperature dependence of the resistivity begins to deviate strongly from the $x = 0\%$ curve [Fig. 6.1(a)], reflecting changes in both the carrier

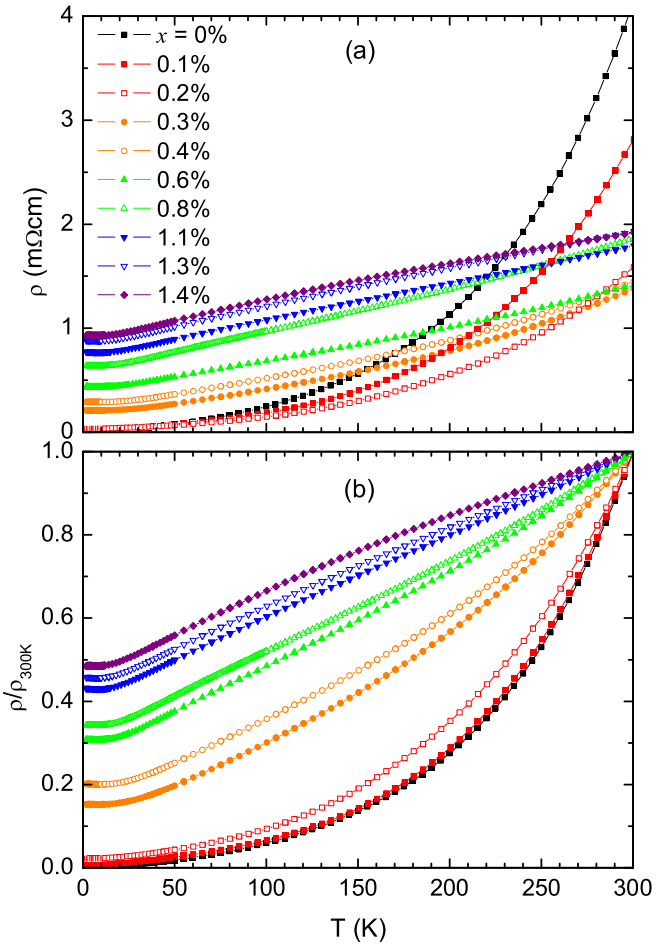

Figure 6.1: Temperature dependence of resistivity for representative samples of each Tl concentration from $x = 0\%$ to $x = 1.4\%$: (a) $\rho(T)$; (b) normalized resistivity $\rho/\rho_{300K}(T)$.

concentration and the scattering. The residual resistivity ρ_0 increases rapidly with x as shown in Fig. 6.2 where ρ_0 is measured at 1.8 K. There appears to be a sudden jump in ρ_0 near $x_c \sim 0.3\%$, the critical concentration for superconductivity (dotted line in Fig. 6.2), beyond which ρ_0 rises rapidly with increasing x. In addition, the Tl substitution reduces the strong temperature dependence of the resistivity forming a linear dependence that extends over a growing range of temperature with increasing x. This evolution of the temperature dependence with changing x is shown more clearly in Fig. 6.1(b), where ρ/ρ_{300K} is the resistivity normalized at 300 K. The linear temperature dependence becomes apparent after a concentration $\sim 0.3\%$ near the critical Tl concentration $x_c \sim 0.3\%$. The linear region extends from about 20 K to 150 K for $x = 0.3\%$ and grows to cover 20 K to 300 K for $x = 1.1\%$. For the highest Tl concentration $x = 1.4\%$, the resistivity follows a slightly weaker temperature dependence above ~ 150 K and may be approaching saturation at the highest temperatures. This behavior shows that the Tl doping dramatically affects the electronic transport in PbTe. We discuss the possible origins of the linear resistivity later in Chapter 7.

For samples with $x > x_c$, the residual resistivity for the unitary scattering limit $\rho(0)$ was estimated using $\rho(0) = 2mc_{\rm imp}/[ne^2\pi\hbar g(E_F)]$, [41] where $c_{\rm imp}$ is the Tl impurity concentration.[1] The hole concentration n was calculated from Hall effect data, and the density of states $g(E_F)$ was estimated from L and Σ band filling using E_F from Chapter 4. The hole mass m was approximated as the average density of states Σ mass $m_\Sigma = 0.2m_0$ (defined here as $m_{\rm DOS} = (m_t^2 m_l)^{1/3}$), since the majority of the carriers for

[1]The Tl impurity concentration $c_{\rm imp}$ in units of cm^{-3} is related to x in at.% by the expression $c_{\rm imp} = 4x/a^3$, where a is the lattice parameter in cm and where there are 4 formula units per unit cell.

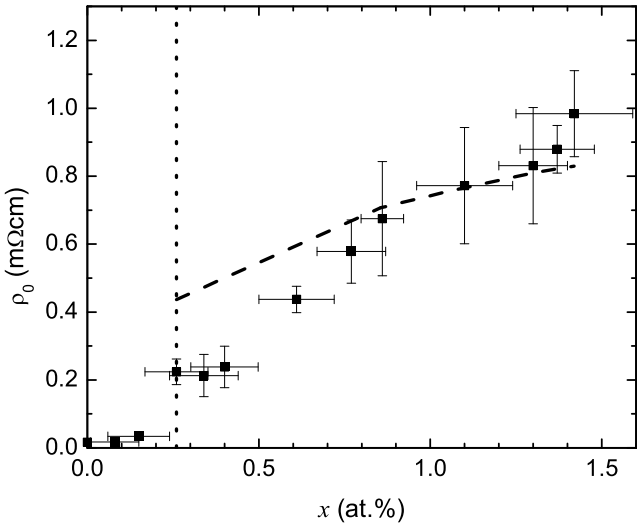

Figure 6.2: Residual resistivity ρ_0 measured at 1.8 K for each Tl concentration x. Data points are average values from several samples for each x. Dashed line represents estimates of the unitary scattering $\rho(0)$ as described in the main text. Vertical dotted line represents the critical concentration $x_c \sim 0.3\%$ for superconductivity. Error bars for ρ_0 represent the standard deviation which was mainly dominated by the uncertainty in the geometric factor used to calculate the resistivity.

samples $x > x_c$ consist of these heavier holes. The resulting estimate of $\rho(0)$ versus x is plotted as the dashed line in Fig. 6.2. Despite some uncertainty in the parameters used to calculate $\rho(0)$, it appears that the resistivity due to the Tl impurities is close to unitary scattering for $x > x_c$. It is noted that using $g(E_F)$ estimated from the low-temperature heat capacity data results in smaller values of $\rho(0)$ relative to the observed residual resistivity ρ_0. The significance of this observation is discussed in Chapter 7.

The temperature dependence of the normal state resistivity at low temperatures was also studied more carefully. For Tl concentrations $x < x_c$ in Fig. 6.3, the resistivity approaches a temperature-independent residual resistivity typical for metallic systems.

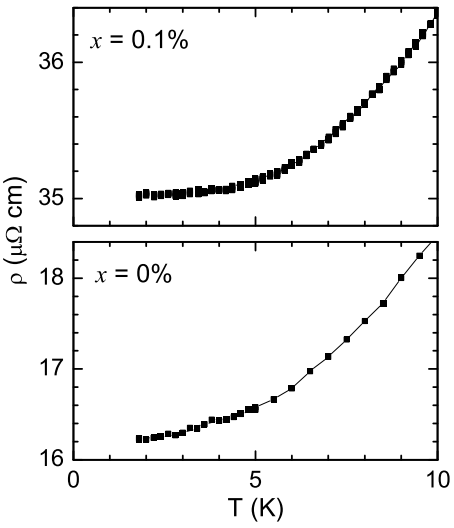

Figure 6.3: Low-temperature resistivity for undoped PbTe (bottom) and $x = 0.1\%$ (top).

While there is large uncertainty in the EMPA data for $x = 0.1\%$, the presence of Tl was confirmed by x-ray absorption. For comparison, the resistivity curves for $x > x_c$ are shown on a logarithmic scale in Fig. 6.4 for temperatures below 10 K. The resistivity shows a distinct upturn for temperatures below approximately 9 K, following a form characteristic of the Kondo effect. Since T_c is higher for $x = 1.3\%$ and $x = 0.8\%$, the resistivity increases briefly before the onset of the superconducting transition. For $x = 0.4\%$ and $x = 0.3\%$, the resistivity increases logarithmically over a restricted temperature range followed by a T^2 saturation as seen in spin Kondo systems, for example Fe in Cu (see Fig. 3.8b). The onset of the upturn at the resistivity minimum does not appear to vary significantly with x. Similar results were observed previously by Andronik and co-workers for temperatures above 4.2 K for a smaller subset of two Tl concentrations [24]. A crude estimate for the magnitude of this effect, neglecting any additional temperature

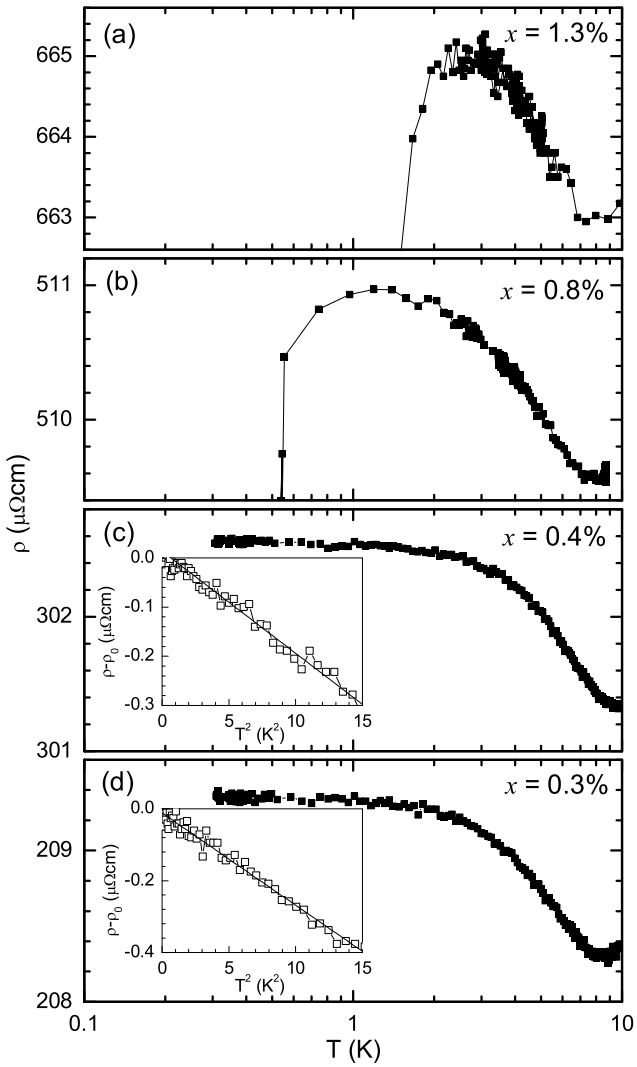

Figure 6.4: Low-temperature resistivity of $Pb_{1-x}Tl_xTe$ for (a) $x = 1.3\%$, (b) $x = 0.8\%$, (c) $x = 0.4\%$, and (d) $x = 0.3\%$. Insets to (c) and (d) show T^2 behavior at low temperatures for the smallest Tl concentrations.

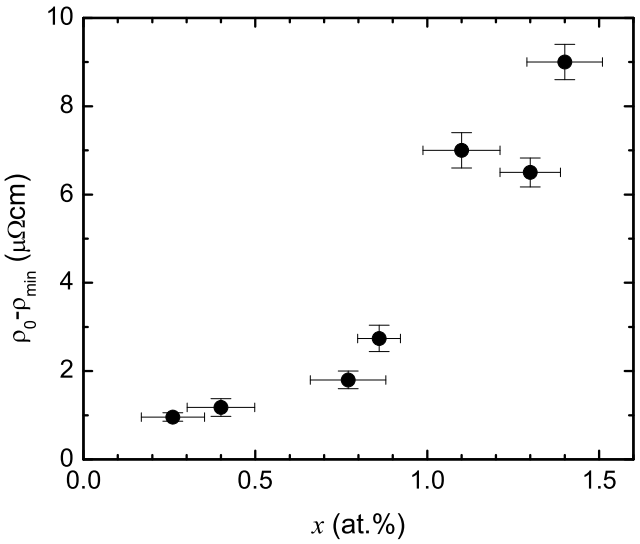

Figure 6.5: Approximate magnitude of the low-temperature resistivity upturn $\rho_0 - \rho_{\min}$ as a function of x. Values were averaged from several crystals at each Tl content x.

dependence below 10 K, can be made from the quantity $\rho_0 - \rho_{\min}$. Here, ρ_0 is the residual resistivity measured at our lowest temperatures and in a field $H > H_{c2}$ to suppress the superconductivity. $\rho_{\min}$ is the value of the resistivity at the resistance minimum. As shown in Fig. 6.5, this quantity appears to scale with the Tl concentration x.

Insets to Fig. 6.4(c) and 6.4(d) show the resistivity as a function of T^2 for the two lowest Tl contents, $x = 0.3$ and 0.4%, for which T_c is less than 0.3 K and the zero-field normal state resistivity can be followed for an appreciable range of temperatures. The resistivity clearly follows a T^2 temperature dependence, as expected for Kondo-like behavior, for temperatures below approximately 4 K. If we associate the observed resistivity upturn with a Kondo-like mechanism, then we can estimate the characteristic Kondo temperature by fitting the data in the insets to Fig. 6.4(c) and 6.4(d) to $\rho_K \sim$

$\rho_K(0)[1 - \left(\frac{T}{T_K}\right)^2]$ where $\rho_K(0)$ is the impurity contribution to the resistivity at $T = 0$, approximated from the measured values of $\rho_0 - \rho_{\min}$. This results in a value of $T_K \sim 6$ K, with considerable uncertainty due to the crude estimate of $\rho_K(0)$.

If we attribute the resistivity upturn to Kondo scattering, then we can estimate the concentration of Kondo impurities c_K at unitary scattering from the observed upturn $\rho - \rho_{\min}$. We use the relation for unitary scattering for Kondo impurities, where Eq. 6.1 becomes

$$\rho_0 - \rho_{\min} \approx \rho_K(0) = \frac{2mc_K}{ne^2\pi\hbar g(E_F)}. \tag{6.1}$$

As in Section 6.1, n is the hole concentration from the measured Hall effect data, $g(E_F)$ is the density of states estimated from band filling effects, and m is approximated as the average Σ effective mass $m_\Sigma = 0.2m_0$ since this band contributes the majority of the density of states. The resulting estimates for c_K are plotted in Fig. 6.6 as a function of x (bottom axis). These values are substantially smaller than the total concentration of Tl c_{imp} (top axis) in each sample, suggesting that only a small fraction of the Tl are contributing to the Kondo scattering. Interpretations of this observation and its implications for the charge Kondo model will be discussed further in Chapter 7.

6.2 Magnetic susceptibility

Since the temperature dependence of the resistivity anomaly for a spin Kondo or charge Kondo effect would be the same, it is necessary to determine the presence or absence of magnetic impurities in this system. The Tl-doped PbTe system alone, if containing

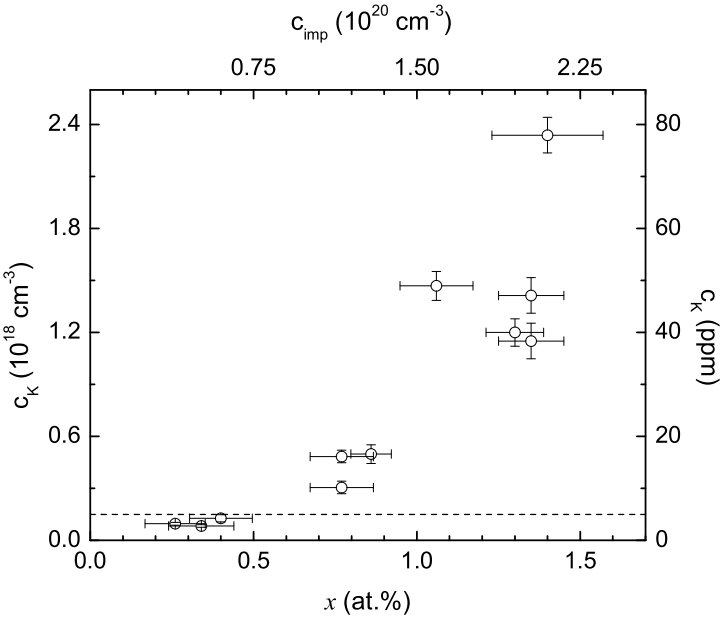

Figure 6.6: Estimated concentration of Kondo impurities c_K as a function of total Tl content x in at.% (bottom axis) and c_{imp} in cm^{-3} (top axis). The right axis indicates the corresponding concentration of Kondo impurities in ppm. The dashed line at 5 ppm represents the upper limit for the concentration of magnetic impurities based on susceptibility measurements.

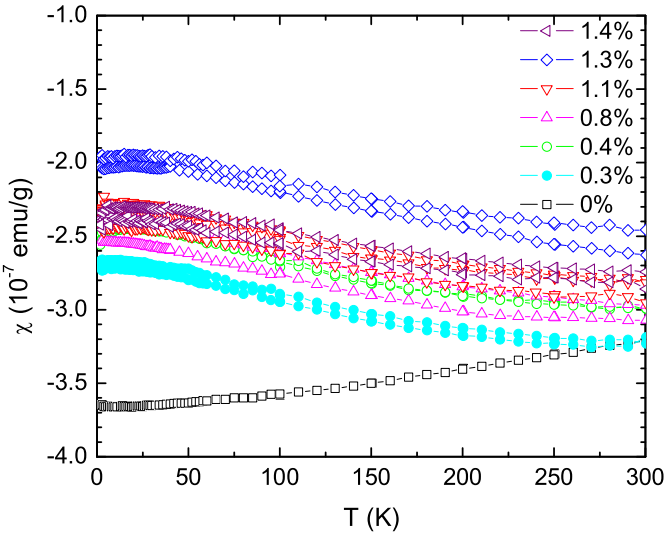

Figure 6.7: Temperature dependence of the susceptibility $\chi(T)$ for different Tl concentrations.

only Tl^{+} and Tl^{3+} impurities, is not expected to exhibit Curie Law paramagnetism. The possibility of accidental magnetic impurities from contamination in the source materials, growth procedure, or crystal handling must also be eliminated.

Representative susceptibility measurements at 1000 Oe for several samples of each Tl concentration are shown in Fig. 6.7 as a function of temperature from 1.8 to 300 K and are broadly consistent with previous reports between 77 to 280 K [58]. The susceptibility is diamagnetic for all Tl concentrations due to the small density of states and becomes less diamagnetic with increasing hole concentration. The weak temperature dependence arises from a temperature dependence of both the band gap and effective mass of PbTe [59]. The difference in temperature dependence between the undoped and doped samples is attributed to the additional temperature-dependent contribution of the

heavy Σ band for samples with Tl [59]. The significant difference between samples of the same Tl content is attributed to errors from background or contamination, which may appear large compared to the very small diamagnetic signal from the actual sample.

The paramagnetic contribution from dilute magnetic impurities can be calculated using the Curie law

$$\chi(T) = \frac{C}{T} = \frac{N_A s(s+1) g^2 \mu_B^2}{3 k_B T}, \tag{6.2}$$

where N_A is 6.022×10^{23}, k_B is Boltzmann's constant, and μ_B is a Bohr magneton. For the free spin case, we use $s = 1/2$ and the Landé factor $g = 2$. The results are shown in Fig. 6.8 where the top figure shows the low-temperature data measured from three representative doped samples, and the bottom figure shows the theoretical Curie contribution for 5 and 50 ppm of magnetic impurities plotted on the same scale. The comparison suggests that there are no magnetic impurities down to < 5 ppm, limited by the resolution of the measurement. However, the estimated c_K values in ppm (right axis in Fig. 6.6) extend much higher than the dashed line representing the 5 ppm upper limit of magnetic impurities. This eliminates both possibilities of accidental sample contamination as well as the presence of magnetic Tl^{2+}. Hence, the low-temperature upturn in the resistivity of Tl-doped PbTe follows a temperature dependence characteristic of the Kondo effect in the absence of magnetic impurities. Since the resistivity upturn scales with the Tl concentration, it is necessary to ensure that the results are reproducible for different Tl sources. Significantly, similar susceptibility results as well as the low-temperature resistivity anomaly were also observed for samples grown by both the very pure elemental Tl

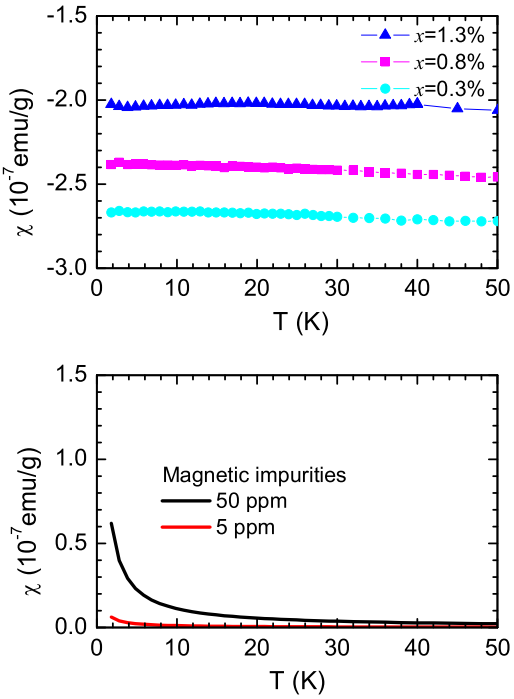

Figure 6.8: Low-temperature susceptibility for (top) measured data from three representative doped samples and (bottom) theoretical Curie contribution for 5 and 50 ppm of magnetic impurities for comparison.

(99.999%) and the less pure Tl_2Te (99.9%) source material (see Section 2.1), confirming that the resistivity upturn is not associated with spurious magnetic impurities from the growth source material.

6.3 Magnetoresistance

Magnetoresistance measurements can provide further information about the scattering mechanisms. Figure 6.9 shows resistivity versus field $\rho(H)$ at different temperatures for a nonsuperconducting sample with $x = 0.1\%$ and three superconducting samples with

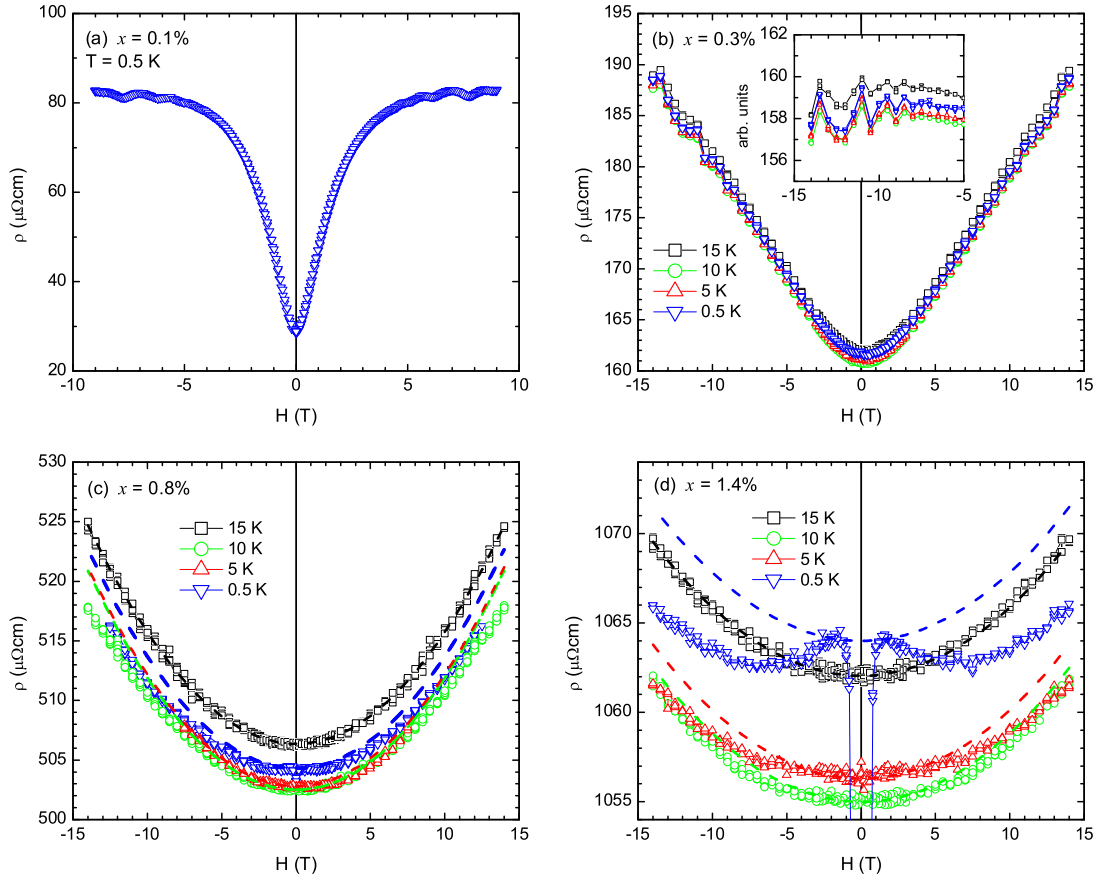

Figure 6.9: Resistivity ρ versus applied field H for Tl concentrations (a) $x = 0.1\%$, (b) $x = 0.3\%$, (c) $x = 0.8\%$, and (d) $x = 1.4\%$ taken at different temperatures.

$x = 0.3\%$, $x = 0.8\%$, and $x = 1.4\%$. First, for $x = 0.1\%$ in panel (a) of Fig. 6.9, the magnetoresistance at 0.5 K is parabolic for very low fields and then quickly becomes linear for fields above approximately 0.4 T. In the high field regime, the resistivity approaches saturation and reveals quantum oscillations which appear symmetric with field. Using Hall data taken at 1.8 K, we can estimate $\omega_c\tau \sim 15$ for this sample at 9 T.

For $x = 0.3\%$ in Fig. 6.9(b), weak field parabolic magnetoresistance is observed for $H < 5$ T. For higher fields, the resistivity varies approximately linearly with field and quantum oscillations are observed for $H > 9$ T and for all temperatures measured below 15 K (where $\omega_c\tau \sim 1$ at 14 T). For $x = 0.8\%$ and 1.4% in (c) and (d) of Fig. 6.9, the magnetoresistance is parabolic up to 14 T at 15 K, indicating that the material is in the weak field limit for all fields measured. Also as a consequence of the smaller $\omega_c\tau$ values, the magnitude of the magnetoresistance is reduced as x increases, and the quantum oscillations disappear by the time x is 0.8%. All curves show positive magnetoresistance except the 0.5 K data for the $x = 1.4\%$ sample in (d), which has $T_c = 1.4$ K. In this 0.5 K curve, after the critical field is reached and superconductivity is suppressed, the magnetoresistance first is negative and then becomes positive at higher fields.

The low field H^2 dependence at 15 K seems to follow a standard Kohler's rule for magnetoresistance in metals [60], where the magnetoresistance is given by

$$\frac{\Delta\rho_K}{\rho(H=0)} = \alpha\left(\frac{H}{\rho(H=0)}\right)^2, \tag{6.3}$$

and α is a constant. If we apply Kohler's rule to the above data in the low field region,

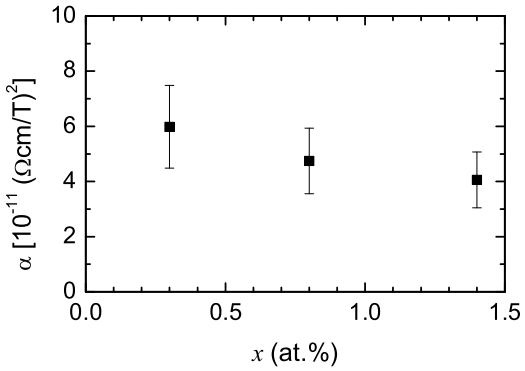

Figure 6.10: Kohler's rule constant factor α versus Tl content x estimated from Eqn. 6.3. Error bars are from uncertainties in the geometric factor used to calculate the sample resistivity.

then the H^2 coefficient should only depend on the zero-field resistance $\rho(H = 0)$. Using the B^2 coefficient at 15 K, we can estimate α for $x = 0.3\%$, 0.8%, and 1.4% where the results are plotted in Fig. 6.10. The values for α remain constant to within the error of the measurement and indicate that Kohler's rule can be reasonably applied to this system. Since the resistivity in these samples changes by $< 1\%$ below 15 K, we can anticipate that the H^2 coefficient would not change significantly for lower temperatures, in the absence of any additional scattering mechanisms. Using α from Fig. 6.10 and respective $\rho(H = 0)$ for each temperature, we plot $\Delta\rho_K$ as dashed lines in (c) and (d) of Fig. 6.9 for the different temperatures. This comparison shows that the measured H^2 coefficient appears to decrease with temperature for $x = 0.8\%$ and $x = 1.4\%$. For the case of $x = 1.4\%$, the suppression is strong enough to produce a negative magnetoresistance at 0.5 K.

6.4 Field dependence of resistivity upturn

As previously reported, all samples with $x > x_c$ exhibit an anomalous low-temperature resistivity upturn, the magnitude of which scales with Tl concentration. The onset of this upturn at 9 K does not appear to change with x. To further analyze the effects of the magnetoresistance, we have measured the temperature dependence of the resistivity upturn in different fields up to 14 T and for temperatures down to 0.5 K. In order to compare the size of the upturn, we have plotted $\rho(T)$ in different fields for each sample after subtracting the Kohler's H^2 magnetoresistance contribution. This procedure is especially important for the smallest Tl concentrations, for which the magnetoresistance can be an order of magnitude larger than the zero field resistivity. Fig. 6.11 plots $\rho(T) - \Delta\rho_K(H)$ for (a) $x = 0.3\%$, (b) $x = 0.8\%$, and (c) $x = 1.4\%$, where $\Delta\rho_K(H)$ is the magnetoresistance contribution estimated from the respective 15 K $\rho(H)$ using Kohler's rule and is equivalent to the shift in resistivity $\Delta\rho_{15K} = \rho(H) - \rho(H = 0)$ at 15 K. For $x = 0.3\%$, the data above 5 T exceeds the weak field limit where the Kohler's H^2 dependence is valid, so the $\Delta\rho_{15K}$ subtraction is used as a reasonable estimate. Since the $x = 0.3\%$ sample has a significantly large magnetoresistance (nearly 30 $\mu\Omega$cm) that is much greater than the observed resistivity upturn ($\rho_0 - \rho_{\min} \sim 1.5\mu\Omega$cm), there is a relatively large uncertainty in the magnetoresistance subtraction. As a consequence of the Kohler's rule magnetoresistance subtraction, the curves shown in Fig. 6.11 are necessarily matched at 15 K well above the resistivity upturn. As can be seen, the resistivity upturn persists even at fields up to 14 T but is reduced in magnitude by approximately 40% for the

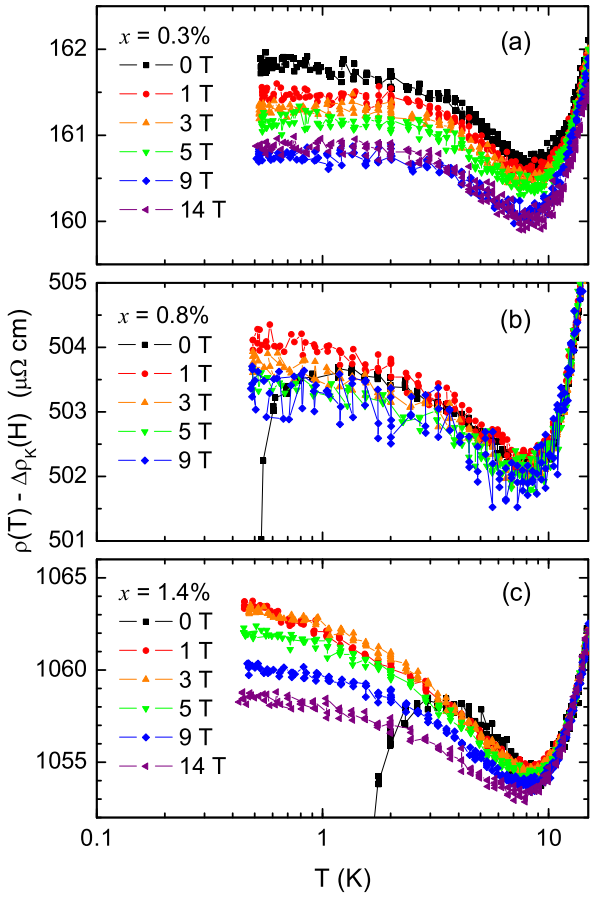

Figure 6.11: Temperature dependence of the low-temperature resistivity upturn measured as $\rho(T) - \Delta\rho_K(H)$ in fields up to 14 T for (a) $x = 0.3\%$, (b) $x = 0.8\%$, and (c) $x = 1.4\%$, where $\Delta\rho_K(H)$ is the Kohler's rule magnetoresistance as defined in the text.

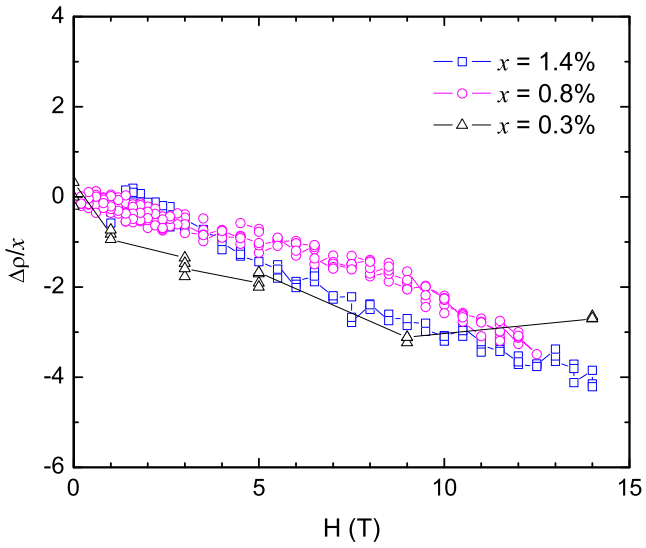

Figure 6.12: Magnetoresistance deviation from Kohler's rule $\Delta\rho(H) = \Delta\rho_{\rm obs}(H) - \Delta\rho_K(H)$ normalized by Tl content x for $x = 1.4\%$, 0.8%, and 0.3% at 0.5 K.

highest fields and for all three Tl concentrations. In addition, the temperature below which the upturn is observed (at ~ 9 K) at the resistivity minimum $\rho_{\rm min}$ does not appear to change as a function of field or Tl content.

The suppression of the resistivity upturn in a magnetic field can be characterized by the field dependence of the deviation of the magnetoresistance from Kohler's rule. We can express this value $\Delta\rho(H) = \Delta\rho_{\rm obs}(H) - \Delta\rho_K(H)$ as the difference between the observed magnetoresistance and the Kohler's contribution. The resulting curves normalized by the Tl content x are shown in Fig. 6.12 for the three samples greater than x_c and for fields greater than H_{c2}. The data appear to follow similar, approximately linear field dependence to within the uncertainty of the subtraction, indicating that the mechanism for the field dependence is similar for all three Tl concentrations. In other words, all

three Tl concentrations exhibit the same small negative magnetoresistance contribution when scaled by the amount of Tl. The initial negative magnetoresistance observed at 0.5 K for $x = 1.4\%$ is a consequence of the smaller Kohler's contribution combined with the larger Tl content, rather than representing a qualitatively separate behavior. A negative contribution to the magnetoresistance is anticipated for magnetic impurities where an applied field causes partial suppression of the spin Kondo effect. However, as the evidence from susceptibility measurements indicate, the resistivity anomaly occurs in the absence of magnetic impurities, suggesting a different origin for the observed behavior. We return to possible explanations of this behavior within a charge Kondo model in the following Chapter.

6.5 Weak localization

The above characterization of Tl-doped PbTe shows that the Tl doping has a drastic effect on the normal state transport properties. The linear resistivity, the low-temperature upturn, and their dependence on doping are particularly difficult to describe with a simple impurity band model. Rather, the low-temperature resistivity upturn appears characteristic of the predicted charge Kondo effect. However, an increase in resistivity at low temperatures can occur by other mechanisms, including quantum interference of the conduction electrons due to defects or disorder in a material. Weak localization is one such effect that may be consistent with the large residual resistivity and the possible negative contribution to the magnetoresistance. This section defines the requirements

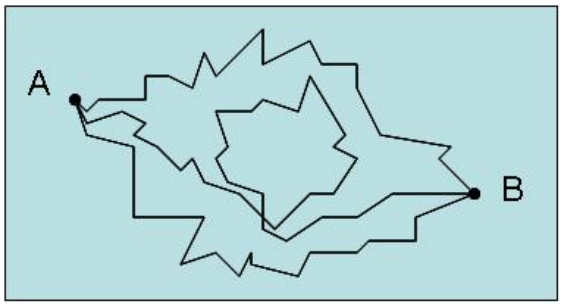

Figure 6.13: Illustration of different random walk electron paths from point A to point B, including an example of a closed-loop path.

for weak localization and some of its characteristic features for comparison with our analysis of Tl-doped PbTe. The analysis suggests that weak localization cannot easily account for the observed normal state transport properties of this material.

Weak localization occurs due to an enhanced probability for scattering due to quantum interference effects and has been described for thin films [61] and for bulk disordered metals [62]. If the elastic mean free path is short, the electron path in a material may be described by a random walk treatment. An illustration of the different paths that an electron may make between points A and B in a material is depicted in Fig. 6.13. There exist closed-loop paths in which the electron may travel clockwise or counterclockwise and return to its starting point. From classical diffusion and in three dimensions, the probability for an electron to travel a distance r in time t is

$$p(r,t) = \frac{\exp(-r^2/4\pi Dt)}{(4\pi Dt)^{3/2}}, \tag{6.4}$$

where $D = v_F l/3$ is the diffusion coefficient. Due to quantum mechanics, the electron

partial waves may travel in different directions around the same closed-loop path, causing constructive interference of their amplitudes. As a result, there is an enhanced backscattering probability for those paths where the electron returns to its starting point. For an electron of wavelength $\lambda = 2\pi/k_F$ that on average maintains phase coherence up to the inelastic scattering time $\tau_{\rm in}$, the probability for enhanced backscattering is

$$p(\tau_{\rm in}) \simeq \frac{\lambda^2 v_F(\tau_{\rm el}^{-1/2} - \tau_{\rm in}^{-1/2})}{(4\pi D)^{3/2}}. \tag{6.5}$$

The result is a reduction in D which in turn reduces the conductivity by the same amount. Therefore, the increase in resistivity is

$$\Delta\rho/\rho_0 = \frac{\alpha(1 - (\tau_{\rm el}/\tau_{\rm in})^{1/2})}{(k_F l)^2}, \tag{6.6}$$

where α is a constant.

The result in Eq. 6.6 describes some of the requirements for weak localization to be observed in a material. The effect is usually considered significant only for small values of the localization parameter $k_F l$, since l must be comparable to the electron wavelength. Additionally, Eq. 6.6 requires $\tau_{\rm in} > \tau_{\rm el}$. Since inelastic scattering would destroy phase coherence, the electron should experience several elastic scattering events before inelastically scattering with phonons. As a consequence, weak localization is a low-temperature effect, since the phonon scattering is reduced and elastic scattering dominates. The onset of weak localization occurs when $\tau_{\rm in} \sim \tau_{\rm el}$, and the resistivity

increases with decreasing temperature. Therefore the temperature dependence of the resistivity is linear with T at low temperatures and goes as $T^{1/2}$ at higher temperatures if the mechanism is phonon scattering.

A magnetic field may also break the phase coherence of the conduction electrons. As a result, weak localization is also expected to exhibit a characteristic field dependence. Specifically, a magnetic field would produce an amount of magnetic flux through the closed-loop path of the electron, inducing a phase change proportional to the field due to the Aharonov-Bohm effect [62]. As a result, the weak localization is reduced rapidly in a magnetic field following a $-B^{1/2}$ dependence.

In the presence of spin-orbit scattering, as the involvement of heavy elements such as Pb and Tl may suggest, the effect of a magnetic field is actually reversed. The spin of an electron may interact with the orbital motion in an atom, where the interaction is stronger for larger nuclear charge. This interaction causes phase changes during scattering events such that the net result is destructive interference for the closed paths and a reduced resistivity. The dephasing effects of the magnetic field would therefore reduce the interference and increase resistivity, resulting in a positive magnetoresistance at low fields. However, a positive magnetoresistance contribution was not observed in our data for Tl-doped PbTe from Section 6.3, suggesting that the resistivity upturn is not associated with weak localization.

The transport measurements presented for Tl-doped PbTe appear to have several other inconsistencies with a simple weak localization scenario. For example, one would expect the onset of weak localization to vary with x, since the effect of changing the

Table 6.1: Electronic and transport parameters of $Pb_{1-x}Tl_xTe$ for representative Tl concentrations at 1.8 K, assuming an isotropic elastic scattering limit. Parameters are calculated separately for both longitudinal and transverse values of effective masses m_L and m_Σ. Uncertainties derive principally from errors in the geometric factor used to estimate resistivity and l.

	$x = 0.1 \pm 0.08$ at.%	$x = 0.3 \pm 0.1$ at.%	$x = 0.8 \pm 0.1$ at.%	$x = 1.4 \pm 0.2$ at.%
E_F	128 ± 3 meV	192 ± 28 meV	212 ± 17 meV	222 ± 17 meV
l	4000 ± 1000 Å	210 ± 52 Å	44 ± 11 Å	19 ± 5 Å
k_F (m_{Ll})	$1.0 \pm 0.1 \times 10^9$ m^{-1}	$1.2 \pm 0.2 \times 10^9$ m^{-1}	$1.3 \pm 0.1 \times 10^9$ m^{-1}	$1.3 \pm 0.1 \times 10^9$ m^{-1}
k_F (m_{Lt})	$2.7 \pm 0.1 \times 10^8$ m^{-1}	$3.3 \pm 0.5 \times 10^8$ m^{-1}	$3.5 \pm 0.3 \times 10^8$ m^{-1}	$3.6 \pm 0.3 \times 10^8$ m^{-1}
k_F ($m_{\Sigma l}$)	–	$7.6 \pm 1.1 \times 10^8$ m^{-1}	$1.0 \pm 0.1 \times 10^9$ m^{-1}	$1.2 \pm 0.1 \times 10^9$ m^{-1}
k_F ($m_{\Sigma t}$)	–	$2.4 \pm 0.3 \times 10^8$ m^{-1}	$3.3 \pm 0.3 \times 10^8$ m^{-1}	$3.7 \pm 0.3 \times 10^8$ m^{-1}
$k_F l$ (m_{Ll})	410 ± 100	26 ± 6.5	5.8 ± 1.4	2.5 ± 0.6
$k_F l$ (m_{Lt})	110 ± 25	7.0 ± 1.7	1.5 ± 0.4	0.7 ± 0.2
$k_F l$ ($m_{\Sigma l}$)	–	16 ± 4.0	4.6 ± 1.1	2.2 ± 0.5
$k_F l$ ($m_{\Sigma t}$)	–	5.0 ± 1.2	1.5 ± 0.4	0.7 ± 0.2

number of scattering impurities changes τ_{el}. This is also assuming that the phonon distribution and inelastic scattering is not changing with x. Our data in Fig. 6.11 show instead that the onset of the resistivity upturn is at approximately 9 K for all samples and does not shift with x nor with field. Additionally, while weak localization is generally limited to low fields, our data show that the resistivity upturn is not completely suppressed up to a field of 14 T and suggest that the mechanism of the upturn is fairly robust in a magnetic field.

The localization parameter $k_F l$ for this material also shows some inconsistencies with the applicability of weak localization. In Table 6.1, we list estimates of the Fermi level E_F, mean free path l, and Fermi wavevector k_F calculated from previous Hall effect analysis (see Section 4.2) at 1.8 K for representative Tl concentrations. Taking into account the existence of both the light and heavy holes at the L and Σ points respectively, we list separate values calculated for the transverse and longitudinal masses

for each band. Tl doping slowly increases the Fermi level deeper into the valence band while rapidly decreasing the mean free path. The resulting $k_F l$ values also decrease significantly. For $x = 0.3\%$, which is the lowest Tl concentration that exhibits a resistivity upturn, $k_F l$ ranges from 26 for the longitudinal L mass m_{Ll} to 5 for the transverse Σ mass $m_{\Sigma t}$. Since Eq. 6.6 shows $\Delta\rho/\rho_0 \sim 1/(k_F l)^2$, these estimated values of $k_F l$ indicate that weak localization is expected to be quite small. For the highest Tl concentration, these same quantities fall to 2.5 and 0.7, respectively. The smaller $k_F l$ values imply that weak localization may become significant, and values near 1 or lower even suggest the possibility of strong localization effects, in which case one would expect more insulating behavior. However, the transport measurements clearly do not indicate a metal-to-insulator transition for this material.

If weak localization is applicable to this system, then these observations would suggest a significant amount of complexity to the localization and scattering mechanisms. Our estimates of $k_F l$ are limited by our assumptions of the known band parameters of PbTe and may not represent the true localization parameter without an accurate description of the two-band transport and any mixed scattering between bands. If the $k_F l$ values are accurate and localization should be significant, then there is the possibility that the weak localization is being screened in this system and may account for the lack of apparent strong localization for $x = 1.4\%$. Overall, it is difficult to describe the temperature and field dependence of the resistivity in terms of the simple weak localization picture.

6.6 High pressure effects

To further investigate the validity of the charge Kondo picture, transport measurements were performed at high pressures. A simple argument based on an ionic model suggests that high enough pressures may split the degeneracy of the two Tl valence states. Specifically, one might naively expect higher pressures to lower the energy of the smaller ion (Tl^{3+}) relative to that of Tl^{+} as the atomic distances are reduced. As the pressure increases, one might then expect that valence degeneracy may occur at a lower critical Tl concentration x^* and that the critical μ^* values may move closer to the top of the valence band.

Hall effect measurements at high pressures may provide information about the carrier density and Fermi level position in the valence band as the pressure is varied. The Hall number for three samples at ambient pressure and 13.5 kbar are shown in Fig. 6.14. The solid line represents the expected Hall number if every Tl contributed one hole. The hole concentration increases under pressure for all samples, increasing more for higher x. The largest is for $x = 1.5\%$, where p_H increases from 1.2×10^{20} cm^{-3} at ambient pressure to 1.4×10^{20} cm^{-3} at 13.5 kbar. This behavior indicates that the hole concentration has increased under pressure. Within the negative-U model proposed for this system (Chapter 3), this suggests that the number of compensating Tl has decreased and the number of Tl^{+} acceptors has increased under pressure. While this is in contrast to the naive assumptions based on ionic radii, possible explanations for the increase in Hall number with pressure are discussed in Section 7.4.

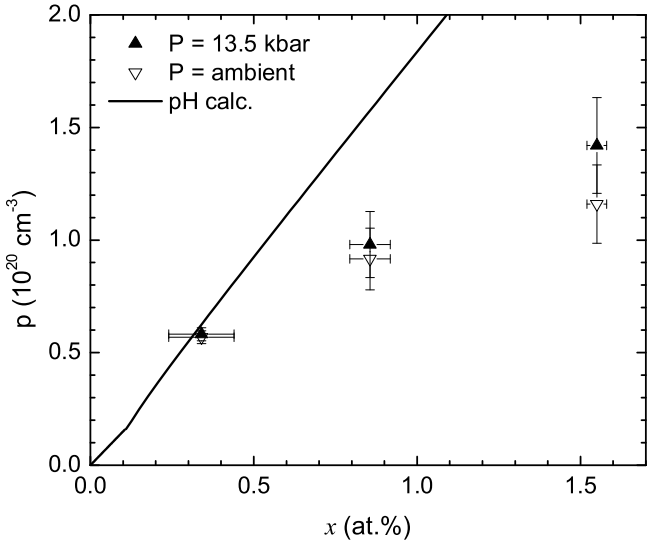

Figure 6.14: Hall number p_H measured for $x = 0.3$, 0.8, and 1.5% at ambient pressure and 13.5 kbar. The solid line represents p_H calculated assuming that each Tl contributes one hole.

In order to study the pressure effects on the charge Kondo mechanism, the low-temperature resistivity upturn was also measured under pressure. The relative temperature dependence of the resistivity upturn for different pressures is shown in Fig. 6.15 as $\rho(T) - \rho_{\min}$. A field of 1 T was applied to suppress the superconducting transition in order to observe the normal state resistivity down to the base temperature. For $x = 1.5\%$, the magnitude of the upturn roughly approximated as $\rho_0 - \rho_{\min}$ is suppressed monotonically with increasing pressure up to approximately 14 kbar as shown in the inset to Fig. 6.15(b). For $x = 0.8\%$ in Fig. 6.15(a), the upturn appears to slightly increase before decreasing with pressure up to approximately 13.5 kbar. The uncertainty in estimating the value $\rho_0 - \rho_{\min}$ is more significant for this sample due to the relatively large noise in the data. For this reason, the trend when comparing changes with pressure for this

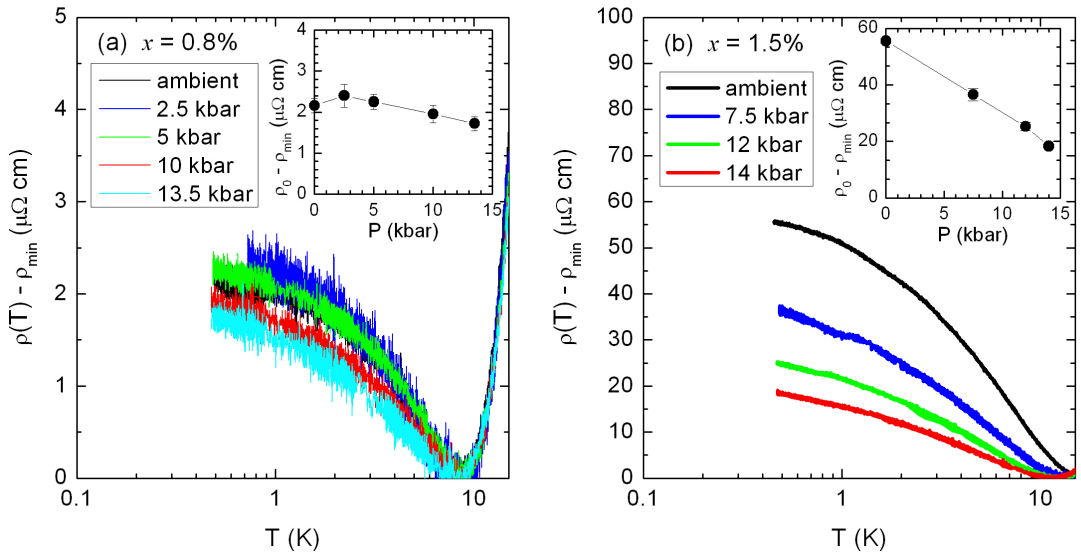

Figure 6.15: Pressure dependence of the low-temperature resistivity upturn estimated as $\rho(T) - \rho_{\text{min}}$ for (a) $x = 0.8\%$ and (b) $x = 1.5\%$. Data was measured at $H = 1$ T $> H_{c2}$ to suppress the superconductivity.

sample is less reliable.

Within the negative-U charge Kondo model (Chapter 3), the increase in Hall number with pressure indicates that the number of Tl^{+} acceptors has increased and, therefore, the number of fluctuating, charge compensating Tl has decreased. If the charge Kondo model is valid, then this observation is consistent with the slight suppression of the resistivity upturn (Fig. 6.15) as well as the suppression of T_c with pressure (Fig. 5.8). However, since these observations are not consistent with the simplistic assumption that high pressure may reduce the energy of the Tl^{3+} state, further possibilities considering more complex pressure dependences are discussed in the following Chapter.

Chapter 7

Discussion

7.1 Evidence for a charge Kondo effect

So far, a number of observations have shown to support the negative-U charge Kondo model proposed in Chapter 3 for Tl-doped PbTe. First in Chapter 4, evidence for the negative-U mixed valence state appears as a carrier concentration saturation in the Hall effect measurements (Fig. 4.3), indicating a self-compensating mixture of Tl^{+} and Tl^{3+} valence states beyond a characteristic Tl concentration $x^{*} \sim 0.3\%$. A low-temperature resistivity upturn was presented in Section 6.1 that is consistent with the charge Kondo effect. The doping dependence and field dependence of the upturn is not easily explained by magnetic impurities, which are limited to less than 5 ppm in this material. Furthermore, the resistivity anomaly and the transport properties are not consistent with a simple weak localization scenario. Significantly, the resistivity anomaly was observed only in superconducting samples where $x > x_c \sim 0.3\%$, coinciding with

the appearance of carrier self-compensation in the mixed valence state above $x^* \sim 0.3\%$. These combined observations suggest that the superconductivity is intimately linked to the presence of the mixed valence state and charge Kondo effect as suggested by the coherent motion of electron pairs on and off the negative-U impurity sites described in the theory (Section 3.5).

In the following Sections, we now examine more closely if these observations, as well as the superconductivity and other anomalous normal state behavior, can be quantitatively explained within the charge Kondo model presented in Section 3.5. Within this model, it was already shown in Section 6.1 that the concentration of Kondo impurities c_K calculated from the resistivity anomaly is small, suggesting that only a small fraction of the Tl are contributing to the Kondo scattering. In this Chapter, the analysis of further observations, including $N(0)$ measured from γ, the dependence of T_c on this quantity, the effects of high pressure, and anomalous transport mechanisms may similarly place limitations on the applicability of the charge Kondo model. An explanation for such limitations is offered and other alternative scenarios are discussed.

7.2 Concentration of Kondo impurities

Although the characteristics of the low-temperature resistivity anomaly are largely consistent with a charge Kondo effect, Section 6.1 has shown that the magnitude of the resistivity upturn is rather small when analyzed in terms of the unitary scattering limit for Kondo scattering. Specifically, if we estimate c_K from the observed resistivity upturn

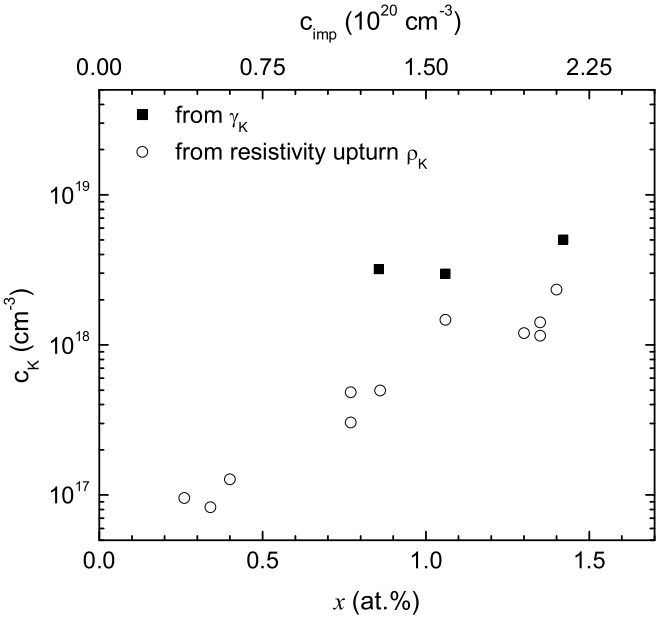

Figure 7.1: Estimated concentration of Kondo impurities as a function of Tl content x in at.% (bottom axis) and c_{imp} in cm^{-3} (top axis). The open symbols are calculated from the magnitude of the resistivity upturn $\rho_0 - \rho_{\mathrm{min}}$. The closed symbols are estimated from the enhancement to the electronic heat capacity γ_K attributed to a Kondo resonance.

and assume unitary scattering at low temperatures, we find a value corresponding to approximately 1% of the total number of Tl impurities (Fig. 6.6). These data of c_K versus x are shown again in Fig. 7.1 on a logarithmic scale.

Another measure of the number of Kondo impurities can be obtained from the additional contribution to the electronic heat capacity deduced in Section 4.3. A Fermi liquid theory treatment of the Kondo problem revealed a Kondo resonance, or the Abrikosov-Suhl resonance, peak at the Fermi level in the electron density of states [41]. It is a high, narrow peak at low temperatures that gradually broadens, shrinks, and disappears above T_K. The feature, which is distinct from the impurity resonance level in the Anderson model, may be detected in spectroscopic techniques like x-ray photoemission

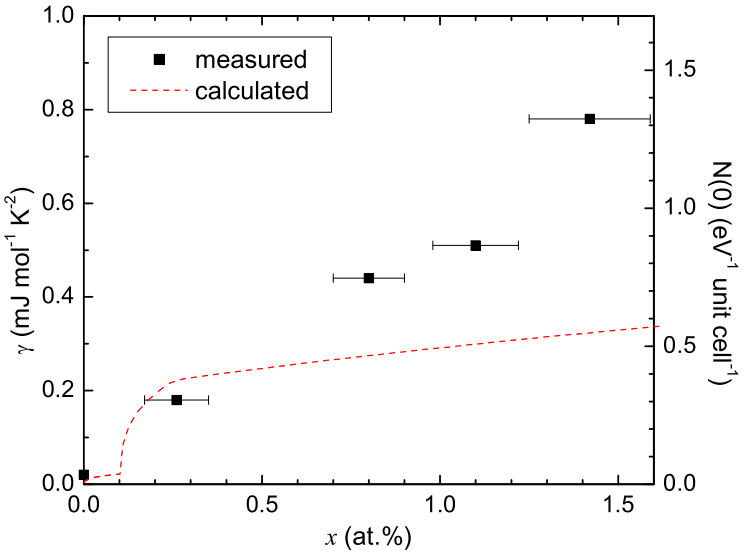

Figure 7.2: Electronic contribution to the heat capacity γ (left axis) and density of states at the Fermi level $N(0)$ (right axis) as a function of Tl content x. The dashed line shows values calculated from known PbTe band parameters and measured values of the Hall number, as described in the main text. Beyond a critical concentration of $\sim 0.3\%$, the measured γ increases to values well above the calculated dashed line.

spectroscopy (XPS) and photoemission specroscopy (PES), or other techniques which probe the density of states like tunneling and heat capacity.

The density of states at the Fermi energy $N(0)$ can be estimated from measurements of the electronic heat capacity γ. The data for γ, estimated from C_p measurements described in Section 4.3, are shown again in Fig. 7.2, with the corresponding values for $N(0)$ included on the right axis. The dashed line represents calculated values for $N(0)$ from known PbTe band parameters and from the Fermi level estimated from the measured Hall number (Fig. 4.2) as described in Section 4.3.

As can be seen, the measured values for γ in Fig. 7.2 increase rapidly above the calculated band contribution for the superconducting samples ($x > x_c \sim 0.3\%$). Such

behavior has been discussed elsewhere [52], where it was said that the observed heat capacity is larger than expected from band filling effects alone, implying the presence of additional states associated with the Tl impurities. One interpretation of this heat capacity peak within the charge Kondo model is that a Kondo resonance contributes to γ as the temperature drops below T_K. The entropy contribution from the (iso)spin 1/2 impurities is $\Delta S = R\ln 2$, such that the total contribution to the heat capacity below T_K may be estimated by the crude approximation

$$\gamma_K T_K \sim R\ln 2 \tag{7.1}$$

per mole of Kondo impurities. Therefore, a measurement of γ_K enables us to estimate the concentration of Kondo impurities.

If we attribute the observed γ enhancement to Kondo physics, then we use Eq. 7.1 to estimate the concentration of Kondo impurities for $T_K \sim 6$ K (the value estimated in Section 6.1 for $x = 0.3\%$). The results are shown as the closed symbols in Fig. 7.1 and are in reasonable agreement with c_K values calculated from the resistivity anomaly (open symbols in Fig. 7.1). Hence, if a charge Kondo description is appropriate for this material, and if the Kondo temperature is ~ 6 K, then the data from γ also support the notion that only a small fraction of the Tl impurities are contributing to this effect.

Invoking Kondo physics of course implies a temperature dependence to the enhancement of γ for temperatures above T_K. Our measurements (Fig. 4.7) show that the enhancement to γ is temperature independent for temperatures between 0.3 and 1 K.

However, uncertainty in this difference grows rapidly at higher temperatures due to the increasingly large phonon contribution to the heat capacity. As a result, we cannot unambiguously extract the temperature dependence of any heat capacity enhancement beyond the estimated Kondo temperature of 6 K.

If a charge Kondo model applies, the analysis above indicates that only a small fraction of Tl impurities are contributing to the Kondo effect. One interpretation of this observation is that not all of the Tl have achieved $\mu = \mu^*$ for valence degeneracy. As described in Section 3.5, the charge Kondo effect requires degenerate, fluctuating valence states. In PbTe, the two Tl valence states become degenerate when a characteristic value of the chemical potential μ^* is reached. The chemical potential then becomes pinned, and all of the Tl impurities may fluctuate between the degenerate valence states. However, it is unlikely that all of the Tl impurities have precisely the same value of μ^*. Given that each Tl may have subtly varying local environments, it is reasonable to assume that there is a distribution of μ^* values. For example, each Tl may have different distributions of nearby vacancies or Tl impurities, resulting in slightly different μ^* values.

For illustration, Fig. 7.3 sketches the density of states $N(0)$ as a function of energy. The distribution of μ^* values are depicted as a Gaussian peak (dotted curve) in the valence band. The chemical potential μ is positioned such that the number of Tl states with $\mu^* < \mu$ (to the right of μ) equals the valence band filling. The shaded region is the approximate width of energy within $T_K \sim 6$ K of μ. Only the small subset of impurities in the shaded region have degenerate valence states where $\mu = \mu^*$ to within $T_K = 6$ K and would contribute to the Kondo effect.

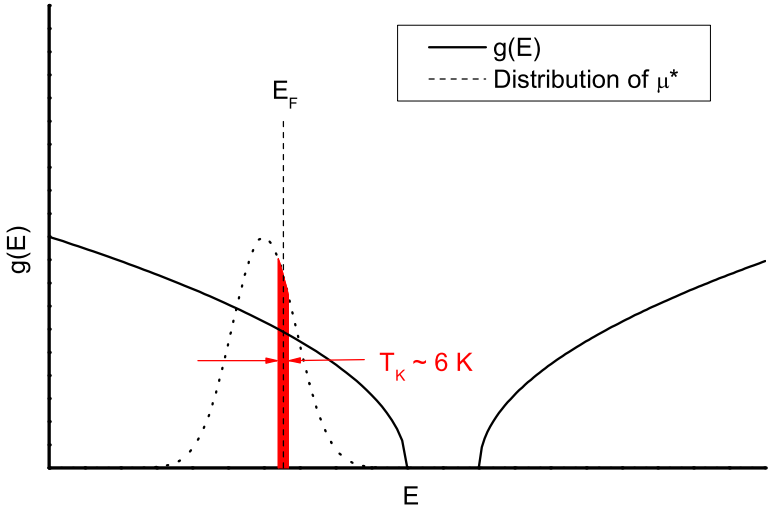

Figure 7.3: Illustration of the density of states $N(0)$ of PbTe relative to a distribution of critical chemical potential μ^* values for degenerate Tl valence states. The width of the shaded region depicts the fraction of impurities within $T_K \sim 6$ K of μ.

There are other observations that appear to support this picture. Hall effect measurements presented in Chapter 4 show that the carrier concentration, and therefore the chemical potential, is not pinned precisely at one value (see Fig. 4.3). It instead continues to rise at a much slower rate beyond the critical concentration x_c. This suggests that μ increases slightly as the distribution of μ^* values grows with increasing Tl doping x.

Heat capacity measurements involving Na counterdoping allow an estimate for the range of μ^* values for Tl impurities in PbTe, which is characterized by a width of 30 meV for $x = 0.5\%$ [16]. Assuming a Gaussian distribution of values of μ^* centered at 220 meV (slightly deeper in the valence band than the observed μ) and with a full width at half maximum of 30 meV, the fraction of Tl impurities for which the two valence states will be degenerate to within $T_K = 6$ K is approximately 1%. The corresponding concentration of 6×10^{17} cm^{-3} is similar to c_{imp} estimated for $x = 0.4\%$ in Fig. 7.1. Within the uncertainties from the rough estimate of the width of the Gaussian distribution and the position of μ, the result of this estimate suggests that the charge Kondo picture with a distribution of μ^* provides a reasonable explanation for the smallness of the resistivity upturn relative to unitary scattering.

Alternatively, a form of the impurity band model may still allow for a smaller number of Kondo impurities than the actual Tl concentration. For example in silicon heavily doped with phosphorus, it has been suggested that not all of the phosphorus contribute to the impurity band and can still add a paramagnetic term to the susceptibility [63]. If a similar situation is occurring for Tl-doped PbTe, then most impurities form a band

and a few are fluctuating Kondo impurities. In this case, the increase in the density of states at the Fermi level is partially due to the impurity band and partially from the Kondo resonance. Such a description preserves the notion of a Tl impurity band that is consistent with Hall effect and heat capacity observations (Chapter 4) while including the notion of a charge Kondo effect to account for the anomalous low-temperature resistivity upturn.

Finally, a third scenario to possibly account for the small magnitude of the resistivity upturn is that the system is already near the unitary scattering limit. Figure 6.2 has shown that the residual resistivity ρ_0 is near the unitary scattering limit if all Tl impurities are contributing and therefore suggests that all of the Tl impurities may already be scattering as effectively as they can regardless of Kondo physics. In that case, the onset of an additional scattering mechanism like the Kondo effect below T_K can only contribute a very small amount to the resistivity beyond the already strong unitary scattering. Since the resistivity saturation due to unitary scattering is independent of the mechanism, the amount due to Kondo scattering or other mechanisms cannot necessarily be distinguished. For example, the data may describe a situation where all of the Tl impurities are contributing to the Kondo effect, but the system is already near unitary scattering due to simple impurity scattering.

7.3 Superconductivity in the charge Kondo model

If a charge Kondo model applies for this system, it is necessary to consider some implications on the superconductivity. The estimate of $T_K \sim 6$ K places this system in the regime where $T_c \sim T_K$. Dzero and Schmalian [8] have provided a theoretical description of superconductivity in charge Kondo systems for $T_c \sim T_K$, where some features are discussed in Section 3.5. In particular, the doping dependence of T_c is interpreted in terms of the competing effects of pair-breaking charge Kondo fluctuations and pair formation due to the negative-U interactions at the impurities.

Whether the enhancement of the density of states $N(0)$ is due to a Kondo resonance or to an impurity band, the results in Fig. 5.7 indicate that the increase in T_c may be attributed to the increase in $N(0)$ if V is constant in a BCS model. However, the situation is less clear if the charge Kondo picture is applicable, in which case V depends strongly on the Tl concentration [8], and the enhancement in $N(0)$ derives from Kondo physics. In the case of a superconductor with magnetic impurities, although $N(0)$ is enhanced by this effect, the superconductivity is nevertheless suppressed for $T \sim T_K$ due to the pair-breaking effect associated with the rapid fluctuations in the magnetic moment [46, 64]. In the case of the charge Kondo model, the situation is slightly more complex because the impurities now provide both a local pairing mechanism as well as a pair-breaking effect close to T_K. Consequently, the range of temperatures over which it is anticipated that T_c will be suppressed is predicted to be much lower than T_K [8], in contrast to the case of magnetic impurities. Hence, for the case $T_c \sim T_K$, the superconductivity can in

principle benefit from the enhancement in $N(0)$ due to the charge Kondo effect in a way that it cannot for magnetic impurities. The observed trend shown in Fig. 5.7 may reflect this effect, but it is difficult to obtain quantitative estimates of the relative contributions to T_c from the enhancement in $N(0)$ and the pairing interaction itself in this crossover regime of $T_c \sim T_K$ [8].

In the charge Kondo model, if T_c is large compared to T_K, then the pseudospin moment is unscreened at T_c, in which case the superconductivity is born from preformed pairs [8]. In this limit, one would anticipate a much smaller anomaly in the heat capacity $\Delta C/\gamma T_c$ than the BCS result of 1.43. As noted in Sec. 5.2, this is clearly not the case for the highest Tl concentrations, consistent with our previous observation that $T_c \sim T_K$ for this material [47]. However, it is difficult to understand the observed x dependence of $\Delta C/\gamma T_c$ within this same picture. Since T_c decreases with decreasing x (Fig. 5.2), one would expect the superconductivity to become more BCS-like at lower Tl concentrations. Instead, we find that $\Delta C/\gamma T_c$ becomes substantially smaller as x is reduced (inset to Fig. 5.6). Experiments are in progress to measure the heat capacity of samples with yet smaller Tl concentrations to even lower temperatures to see whether this trend continues [65].

The most extraordinary aspect of the competing pair-breaking and pair-forming role of charge Kondo impurities is the predicted reentrant superconductivity (Section 3.5). From estimates of the charge Kondo parameters based on T_c versus x data for Tl-doped PbTe, it was estimated that the normal state may reappear below 30 mK for this system [8]. However, reentrance was not observed in dilution fridge measurements

(Section 5.1) down to 15 mK. This places limits on the charge Kondo parameters for Tl-doped PbTe, where the reentrance regime in this system may actually occur at lower temperatures. Experiments are currently in progress to measure down to microkelvin temperatures with Y. Lee at the Microkelvin Laboratory in the University of Florida.

7.4 Effect of high pressure

Based on the negative-U charge Kondo model discussed in Section 3.5, the increasing Hall number under pressure in Fig. 6.14 indicates that the number of fluctuating, charge compensating impurities has reduced under pressure and that the number of acceptor Tl^+ has increased. Therefore, the data suggests that the μ^* values have shifted slightly deeper into the valence band. This description is consistent with the observed reduction of the charge Kondo upturn under pressure (Fig. 6.15) and reduction in T_c (Fig. 5.8), since the number of fluctuating Tl has decreased. This is in contrast to naive expectations based on ionic radii, indicating that a more sophisticated approach is necessary to understand the effect of pressure on both the superconductivity and the resistivity upturn.

One way to account for the pressure effect of the Hall number is to estimate the movement under pressure of the valence bands and impurity band (or μ^* distribution peak) relative to each other and then estimate the band filling. We start by assuming that the effect of decreasing temperature on the band structure is nearly the same as the effect of increasing pressure due to volume change. This assumption has been shown

to be reasonable for changes in the fundamental bandgap using band structure calculations, compressibility data, and thermal expansion coefficients and comparing with experimental data [66]. For $\partial E_g/\partial T$ ranging from 4.1 to 4.5×10^{-4} eV/K from absorption spectra and band structure calculations [19, 31, 66] and $\partial E_g/\partial P$ ranging from -7.4 to -7.5×10^{-6} eV/bar from optical absorption experiments and band calculations [18,66], we see that a pressure of 13.5 kbar results in a bandgap change approximately equivalent to a temperature change of 230–250 K. Similarly, the change in ΔE_v with temperature and pressure can be expected to produce the same result due to volume change. With $\partial \Delta E_v/\partial T$ ranging from -4.1 to -4.3×10^{-4} eV/K from optical absorption [19, 31, 67] and $\partial \Delta E_v/\partial P = 7 \times 10^{-6}$ eV/bar from galvanomagnetic measurements [68], we find that increasing the pressure to 13.5 kbar is also the same as decreasing the temperature by 230–240 K, which increases the secondary valence band edge deeper into the L band from 170 meV to approximately 270 meV.

Given that a 13.5 kbar pressurization can be reasonably approximated as a 230 K temperature decrease, we now estimate the pressure dependence of the Tl impurity band (or μ^* states) using its known temperature dependence. Previous studies using an impurity band model have estimated $\partial E_i/\partial T = 2 - 4 \times 10^{-4}$ eV/K from Hall effect measurements [50] and from Hall effect and optical absorption [51]. These values indicate that the Tl states appear to shift at the same rate as ΔE_v with temperature and pressure, as illustrated in Fig. 7.4. For increasing temperature towards the right, both the Σ band and the impurity states E_i shift up toward the top of the L valence band. For increasing pressure towards the left, they shift down deeper into the L band.

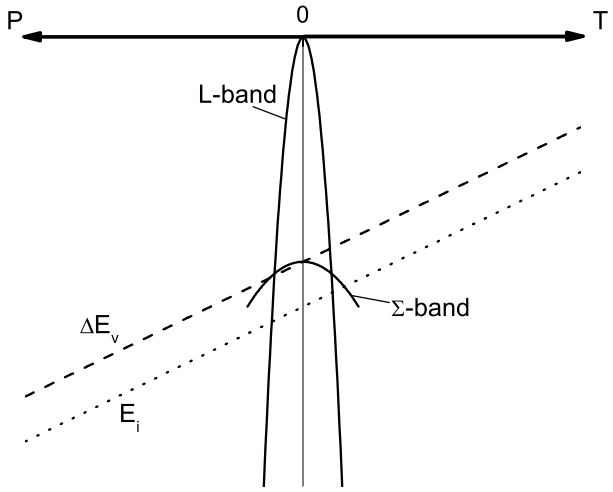

Figure 7.4: Illustration of the energy shift with temperature (top axis towards the right) and pressure (towards the left) of the Σ band offset ΔE_v and Tl states E_i relative to the top of the L valence band.

To depict the situation for the measured $x = 1.5\%$ sample, Fig. 7.5 shows the approximate picture for the density of states $g(E)$ and the Tl states at ambient pressure (top panel) and at 13.5 kbar (bottom panel). Using the measured Hall number to estimate E_F (dotted line) for each pressure, we find that the position of the Fermi level did not shift much relative to the top of the heavy Σ band. Therefore, the valence band shift due to pressure accounts almost entirely for the increase in carrier concentration as holes are transferred from the impurity band to the L band. Also as a result of this transfer, the impurity band appears to have shifted slightly deeper into the Σ, since more Tl states have become (doubly) occupied Tl^+ or filled below E_F. If we consider a distribution of μ^* values due to hybridization, it is also possible that the distribution has broadened with pressure, further reducing the number of states degenerate to within T_K.

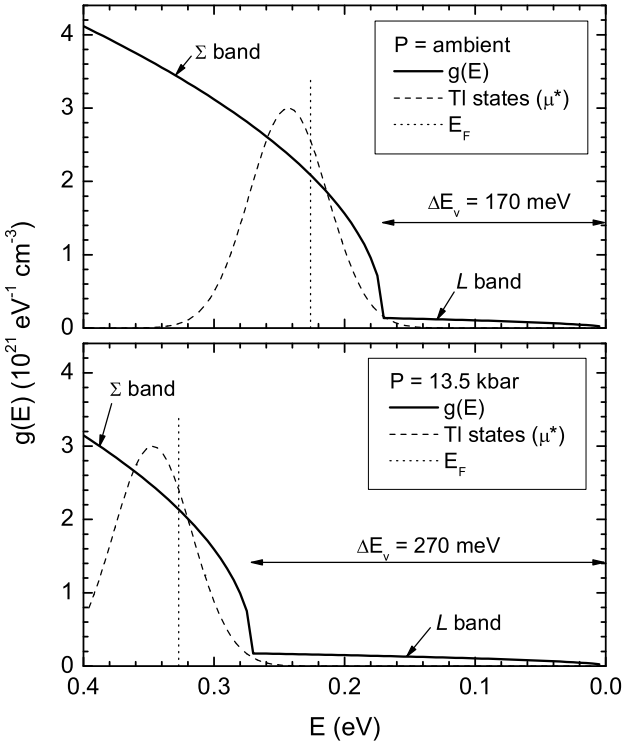

Figure 7.5: Density of states $g(E)$ (solid curve) of Tl-doped PbTe relative to a distribution of Tl states (dashed curve) and E_F (dotted line). Top panel is at ambient pressure with $\Delta E_v = 170$ meV. Bottom panel shows the increase of ΔE_v to 270 meV at 13.5 kbar.

The data on our single crystals are not entirely consistent with previous high pressure work on thin films interpreted with a quasilocal impurity band model [69]. An increase in T_c at low pressures was observed in the thin films followed by a decrease at higher pressures up to 12 kbar. The data was explained by a shifting of the impurity band into the L band and a rapidly changing density of states near the Σ band edge based on a Hall coefficient at 77 K that was decreasing with pressure. Since an increase in T_c was not observed in our single crystals, it is possible that strain effects from the thin film samples modify the applied pressure results.

Although for the analysis here the pressure dependence of the band shifts were roughly approximated using the assumptions of previously calculated or measured temperature and pressure dependences, this model appears to account for the measured Hall effect data under pressure. For a consistent doping effect implied by the Hall number and since the position of E_F within this band determines how many Tl are acceptors and how many are donors, it appears that the Fermi level is slightly lower on the shoulder of the Tl impurity band distribution illustrated in Fig. 7.5. As a result, in a charge Kondo model, the states that are degenerate to with T_K have been reduced by pressure. This picture of a reduced fraction of Kondo impurities with pressure is consistent with the pressure dependence of the resistivity upturn (Fig. 6.15) and of T_c (Fig. 5.8). As the number of fluctuating Tl impurities decrease, the upturn becomes suppressed. The decrease in concentration of Kondo impurities would consequently reduce the Kondo resonance and the enhancement to the density of states. As a result, T_c becomes smaller as the number of pairing centers decrease as well as due to the smaller density of states

in a BCS picture.

7.5 Evidence for an alternative transport mechanism

A few puzzling aspects of the transport behavior described in Chapter 6 are particularly difficult to explain based on simple models. First, it is surprising that the localization parameter $k_F l$ values reported in Section 6.5 for the highest Tl concentrations are quite small despite the lack of insulating behavior in this material. If the estimates of $k_F l$ are accurate, then the presence of a separate conductivity mechanism that masks the single electron band contribution may be necessary to account for this behavior.

Secondly, the linear resistivity $\rho(T)$ in Fig. 6.1 is a drastic deviation from the temperature dependence of the undoped PbTe. The growing linear region with Tl doping suggests the emergence of another scattering or transport mechanism contributing to the resistivity. While the increasing carrier concentration with x may suggest an enhanced screening of phonons or electron-phonon interactions, it is unclear if such a scenario may account for the dramatic change in temperature dependence.

An intriguing possibility suggested by Dzero and Coleman [70] is the effect of a pair diffusion component to the high-temperature conductivity predicted in charge Kondo systems. The pair conductivity using the Einstein relation is $\sigma_p \sim D\chi_c$, where D is the diffusion constant and the charge susceptibility χ_c goes as $1/T$ at high temperatures. Consequently, the resistivity is expected to have a linear temperature dependence that acts in parallel with the usual band contribution and that increases with impurity doping.

While the data appears to roughly follow such a trend (Fig. 6.1), a more exact analysis of the pair conductivity is necessary to quantitatively confirm its applicability. The details of this model go beyond the scope of this thesis and are still being developed [70]. However, if the temperature dependence of the resistivity is associated with a two-channel conductivity, this might also account for the metallic behavior observed in a regime where $k_F l \sim 1$.

7.6 Origin of negative contribution to magnetoresistance

Perhaps the greatest challenge to the applicability of a charge Kondo model in this material is the small negative contribution to the magnetoresistance. This observation was shown to be difficult to explain by weak localization and is not likely due to magnetic impurities. In a spin Kondo picture, a magnetic field splits the degeneracy of the spin states and results in a negative magnetoresistance as the Kondo scattering is reduced. In a charge Kondo picture, the magnetic field does not affect the degeneracy of the impurity valence states, so at first sight there is no expected magnetoresistance.

In the case of Tl-doped PbTe however, there are small Fermi surfaces with a rapidly changing density of states with Fermi energy. In large fields, a Pauli spin magnetization resulting from the Zeeman splitting may cause a significant change in the number of spin up states relative to spin down states. For small Fermi surfaces and large fields, the relative difference of up and down states can be large. Since the charge Kondo model includes the motion of electron pairs with up and down spins, a substantial imbalance

in the number of available up and down spin electrons may suppress the charge Kondo behavior and may be consistent with the systematic suppression of the Kondo anomaly and field dependence depicted in Fig. 6.11 and 6.12. This hypothesis qualitatively accounts for the small negative magnetoresistance, but a quantitative description awaits more detailed theoretical treatment.

7.7 Alternative descriptions

While the interpretation of the transport properties and normal state data are consistent with a charge Kondo model of negative-U impurities in a mixed valence state, most observations cannot rule out a resonant impurity band theory. It has been previously suggested that the superconductivity in Tl-doped PbTe can be described in terms of quasilocalized impurity states at the Fermi level with resonant scattering [16]. Since a resonant impurity band of localized states or with very low mobility would not contribute to the Hall number, it was suggested [16, 22] that the saturation of the carrier concentration is due to filling of the narrow impurity band peak where the chemical potential is pinned. The large increase in the electronic heat capacity γ is then also consistent with an impurity band contribution to the density of states causing the T_c enhancement. In such a case, the pairing interaction would most likely be phonon mediated, though the substantial residual resistance might argue that strong Coulomb scattering also plays a role.

On the other hand, the anomalous transport properties described in Chapter 6 are

not explained satisfactorily with the resonant impurity band model. Significantly, simple impurity potential scattering alone cannot produce a resistivity minimum and low-temperature upturn. Furthermore, the dramatic change in the temperature dependence of the resistivity with Tl content is difficult to explain with resonant scattering alone with the assumption that the Tl doping does not significantly alter the band structure. While the superconductivity has been treated with the resonant scattering theory [16,22], these anomalous transport features have not been thoroughly addressed previously.

If the impurity band model is valid, then the anomalous transport properties must arise from other sources. In the absence of magnetic impurities, then the most likely candidate for the resistivity upturn would be weak localization. However, as described in Section 7.6, such a scenario would require an unusual combination of effects to result in the temperature dependence and magnetoresistance observed. It is especially difficult to produce a ρ_{min} that does not change with impurity doping within a simple weak localization picture. Given the shortcomings of these alternative descriptions, our observations indicate that Tl-doped PbTe is best described by a charge Kondo model.

Chapter 8

Conclusion and ongoing collaborations

In this thesis, we have described Tl-doped PbTe using a negative-U charge Kondo model where the Tl impurities form a special mixed valence state of Tl^{+} and Tl^{3+}. We have shown evidence for the appearance of the mixed valence state as a carrier concentration saturation in the Hall number beyond $x_c \sim 0.3\%$. This work has presented the first extensive and systematic study of the low-temperature resistivity upturn to show that, in the absence of magnetic impurities down to 5 ppm and without a clear signature for weak localization, it is consistent with a charge Kondo effect arising from quantum valence fluctuations between the degenerate valence states differing by two electrons. Significantly, the charge Kondo effect was observed only in superconducting samples where

$x > x_c \sim 0.3\%$ and coinciding with the mixed valence state suggested by Hall measurements to appear above $x^* \sim 0.3\%$. While none of our observations are inconsistent with a charge Kondo model, they do show some limitations to its applicability by suggesting that the magnitude of the resistivity upturn is consistent with a small concentration of the total number of Tl impurities contributing to this effect. Other mechanisms or scenarios were considered, including an impurity band model with resonant scattering. However, such a model does not satisfactorily explain a resistivity upturn, although our data do not necessarily rule out a form of an impurity band contribution.

A clear demonstration of a charge Kondo effect and a negative-U scenario would suggest an alternate pairing mechanism for superconductivity in this material and potentially explain its anomalously high T_c. For example, the theoretical models based on negative-U impurities described in Section 3.5 predict reentrant superconductivity at low temperatures due to the pair-forming behavior of the negative-U impurities and the pair-breaking nature of the Kondo scattering. The observance of such an effect would provide unambiguous evidence for charge Kondo physics. As mentioned in Section 7.3, microkelvin experiments are currently underway in collaboration with Y. Lee at the Microkelvin Laboratory in the University of Florida [71].

Another signature for the Kondo effect is the Kondo resonance peak in the spectral density at the Fermi level (Section 7.2). Such a feature would appear as a zero-bias peak in a tunneling spectrum below T_K and would confirm that the observed enhancement in the electronic heat capacity is indeed due to the Kondo resonance and not simply an impurity band. Preparations are being made for scanning tunneling microscopy

(STM) experiments on cleaved single crystals at low temperatures with L. Mattos and H. Manoharan at Stanford University.

Experiments to extend the limits of the current experimental range of Tl doping in PbTe, may reveal more about the role of the Tl impurities for superconductivity and a charge Kondo effect. For instance, we see how T_c increases rapidly with x (Fig. 5.2), but we are limited by the solubility limit ($\sim 1.5\%$) of Tl in PbTe. Methods including ion implantation and rapid crystallization allow one to exceed thermodynamic limits and solubilities in a material. Ion implantation followed by a conditioning anneal has been used to form thermodynamically unstable GaN_xAs_{1-x} films by N^+ ion implantation [72]. To investigate the superconductivity and charge Kondo behavior for possibly higher doping concentrations, Tl ion implantation experiments on single crystal PbTe are currently in progress in collaboration with M. A. Scarpulla and O. D. Dubon at the University of California, Berkeley.

Finally, if the charge Kondo effect can be found generically in other systems, it would support the validity of a negative-U charge Kondo model for superconductivity. In other words, the observation of similar physical effects in different systems involving valence-skipping elements or suspected negative-U centers would further substantiate our suggestion that valence fluctuations are responsible for the high T_c in Tl-doped PbTe. The charge Kondo model was originally proposed for the superconducting barium bismuthates, $BaBi_xPb_{1-x}O_3$ and $Ba_xK_{1-x}BiO_3$, for which the Bi was thought to form Bi^{3+} and Bi^{5+} [37]. Previous data of extended x-ray absorption fine structure (EXAFS) experiments on $BaBi_xPb_{1-x}O_3$ were found to fit two distinct Bi-O distances in support

of the mixed valence state [73]. As was the case with Tl-doped PbTe, we believe a small charge Kondo effect in the resistivity at low temperatures may be easily overlooked, as the anomaly may be quite small compared to the residual resistivity. However, preliminary attempts to observe a charge Kondo effect in single crystal Bi-doped $BaPbO_3$ were hampered by substantial sample inhomogeneity and possible magnetic impurities [74].

A more promising system that is very similar to Tl-doped PbTe is In-doped SnTe. Indium is also a valence-skipping element (Section 3.2) and possible negative-U center where it is known to form In^+ and In^{3+} valence states in solids. It may account for remarkably high T_c values for In-doped SnTe [75, 76] due to the same mechanism as the Tl in PbTe. Preliminary results [74] have shown a similar correlation between superconductivity and the appearance of a resistivity upturn at low temperatures. Further systematic studies of the superconducting and normal state properties of In-doped SnTe are currently in progress.

Bibliography

[1] R. Micnas, J. Ranninger, and S. Robaszkiewicz, Rev. Mod. Phys. **62**, 113 (1990).

[2] V. Z. Kresin, H. Morawitz, and S. A. Wolf, *Mechanisms of conventional and high Tc superconductivity*, volume 84, Oxford University Press, New York, 1993.

[3] T. H. Geballe and B. Y. Moyzhes, Physica C **341-348**, 1821 (2000).

[4] T. H. Geballe and B. Y. Moyzhes, in *10th International Workshop on Oxide Electronics*, volume 13, pages 20–6, Augsburg, Germany, 2004.

[5] J. A. Wilson and A. Zahrir, Rep. Prog. Phys. **60**, 941 (1997).

[6] M. B. Robin and P. Day, Adv. Inorg. Chem. and Radiochem. **10**, 247 (1967).

[7] C. M. Varma, Phys. Rev. Lett. **61**, 2713 (1988).

[8] M. Dzero and J. Schmalian, Phys. Rev. Lett. **94**, 157003 (2005).

[9] H. B. Schuttler, M. Jarrell, and D. J. Scalapino, Phys. Rev. B **39**, 6501 (1989).

[10] J. E. Hirsch and D. J. Scalapino, Phys. Rev. B **32**, 5639 (1985).

[11] A. G. Mal'shukov, Solid State Commun. **77**, 57 (1991).

[12] B. Y. Moizhes and I. A. Drabkin, Sov. Phys. Solid State **25**, 1139 (1983).

[13] M. V. Krasin'kova and B. Y. Moizhes, Sov. Phys. Solid State **33**, 202 (1991).

[14] A. A. Abrikosov and L. P. Gor'Kov, Sov. Phys. JETP **12**, 1243 (1961).

[15] V. I. Kaidanov and Y. I. Ravich, Sov. Phys. Usp. **28**, 31 (1985).

[16] S. A. Nemov and Y. I. Ravich, Phys. Usp. **41**, 735 (1998).

[17] Y. I. Ravich, B. A. Efimova, and I. A. Smirnov, *Semiconducting Lead Chalcogenides*, Plenum Press, New York, 1970.

[18] R. Dornhaus, G. Nimtz, and B. Schlicht, *Narrow-Gap Semiconductors*, volume 98 of *Springer Tracts in Modern Physics*, Springer-Verlag, New York, 1983.

[19] D. Khokhlov, editor, *Lead Chalcogenides: Physics and Applications*, Taylor and Francis, New York, 2003.

[20] J. K. Hulm, M. Ashkin, D. W. Deis, and C. K. Jones, Prog. in Low-Temp. Phys. **VI**, 205 (1970).

[21] I. A. Chernik and S. N. Lykov, Sov. Phys. Solid State **23**, 817 (1981).

[22] H. Murakami, W. Hattori, and R. Aoki, Physica C **269**, 83 (1996).

[23] K. G. Gartsman, T. B. Zhukova, and S. A. Nemov, Inorg. Mater. **21**, 426 (1985).

[24] K. I. Andronik, V. F. Banar, V. G. Kantser, and A. S. Sidorenko, Phys. Status Solidi B **133**, K61 (1986).

[25] T. B. Massalski, editor, *Binary Alloy Phase Diagrams*, ASM International, Materials Park, OH, 2nd edition, 1990.

[26] W. Palosz, J. Cryst. Growth **216**, 273 (2000).

[27] R. F. C. Farrow, in *Molecular Beam Epitaxy and Heterostructures. Proceedings of a NATO Advanced Study Institute*, pages 227–62, Erice, Italy, 1985.

[28] T. C. Harman and J. P. McVittie, J. Electron. Mater. **3**, 843 (1974).

[29] G. Martinez, M. Schluter, and M. L. Cohen, Phys. Rev. B **11**, 651 (1975).

[30] C. Kittel, *Introduction to Solid State Physics*, Wiley, New York, 1996.

[31] H. Sitter, K. Lischka, and H. Heinrich, Phys. Rev. B **16**, 680 (1977).

[32] B. F. Gruzinov, I. A. Drabkin, and Y. I. Ravich, Sov. Phys. Semicond. **13**, 315 (1979).

[33] P. P. Konstantinov, S. N. Lykov, Y. I. Ravich, and I. A. Chernik, Sov. Phys. Solid State **24**, 2011 (1983).

[34] C. Keffer, T. M. Hayes, and A. Bienenstock, Phys. Rev. B **2**, 1966 (1970).

[35] P. W. Anderson, Phys. Rev. Lett. **34**, 953 (1975).

[36] C. M. Varma, Rev. Mod. Phys. **48**, 219 (1976).

[37] A. Taraphder and P. Coleman, Phys. Rev. Lett. **66**, 2814 (1991).

[38] A. Taraphder, H. R. Krishnamurthy, R. Pandit, and T. V. Ramakrishnan, Phys. Rev. B **52**, 1368 (1995).

[39] K. Weiser, Phys. Rev. B **23**, 2741 (1981).

[40] M. Schluter, G. Martinez, and M. L. Cohen, Phys. Rev. B **11**, 3808 (1975).

[41] A. C. Hewson, *The Kondo Problem to Heavy Fermions*, volume 2 of *Cambridge Studies in Magnetism*, Cambridge University Press, New York, 1997.

[42] D. L. Cox and A. Zawadowski, Adv. Phys. **47**, 599 (1998).

[43] J. Kondo, Prog. Theor. Phys. **32**, 37 (1964).

[44] C. M. Hurd, editor, *Electrons in Metals*, Wiley, New York, 1975.

[45] A. J. Heeger, Solid State Phys. **23** (1969).

[46] M. B. Maple et al., Solid State Commun. **11**, 829 (1972).

[47] Y. Matsushita, H. Bluhm, T. H. Geballe, and I. R. Fisher, Phys. Rev. Lett. **94**, 157002 (2005).

[48] I. A. Chernik, S. N. Lykov, and N. I. Grechko, Sov. Phys. Solid State **24**, 1661 (1982).

[49] A. N. Veis, V. I. Kaidanov, and R. Y. Krupitskaya, Sov. Phys. Semicond. **22**, 215 (1988).

[50] T. R. Mashkova and S. A. Nemov, Sov. Phys. Semicond. **19**, 1148 (1985).

[51] S. D. Darchuk, L. A. Korovina, and F. F. Sizov, Sov. Phys. Semicond. **26**, 476 (1992).

[52] I. A. Chernik and S. N. Lykov, Sov. Phys. Solid State **23**, 2062 (1981).

[53] A. J. Bevolo, H. R. Shanks, and D. E. Eckels, Phys. Rev. B (Solid State) **13**, 3523 (1976).

[54] I. A. Chernik and S. N. Lykov, Sov. Phys. Solid State **23**, 1724 (1981).

[55] N. Werthamer, E. Helfand, and P. Hohenberg, Phys. Rev. **147**, 295 (1966).

[56] R. J. Ormeno, P. J. Baker, and C. E. Gough, (private communication).

[57] G. Mandel, Phys. Rev. **134**, A1073 (1964).

[58] K. I. Andronik, M. P. Boiko, and A. V. Luzhkovskii, Sov. Phys. Semicond. **22**, 1190 (1988).

[59] G. V. Lashkarev, R. O. Kikodze, and A. V. Brodovoi, Sov. Phys. Semicond. **12**, 633 (1978).

[60] A. B. Pippard, *Magnetoresistance in Metals*, Cambridge University Press, New York, 1989.

[61] G. Bergmann, Phys. Rep. **107**, 1 (1984).

[62] J. S. Dugdale, editor, *The Electrical Properties of Disordered Metals*, Cambridge University Press, New York, 1995.

[63] M. Lakner, H. v. Lohneysen, A. Langenfeld, and P. Wolfle, Phys. Rev. B **50**, 17064 (1994).

[64] E. Muller-Hartmann and J. Zittartz, Phys. Rev. Lett. **26**, 428 (1971).

[65] F. Ronning and R. Movshovich, (private communication).

[66] M. Schluter, G. Martinez, and M. L. Cohen, Phys. Rev. B **12**, 650 (1975).

[67] R. N. Tauber, A. A. Machonis, and I. B. Cadoff, J. Appl. Phys. **37**, 4855 (1966).

[68] A. A. Andreev, J. Phys. (Paris) **29**, C4 (1968).

[69] S. A. Kaz'min et al., Sov. Phys. Solid State **26**, 1930 (1984).

[70] M. Dzero and P. Coleman, (private communication).

[71] Y. Lee, (private communication).

[72] K. M. Yu et al., J. Appl. Phys. **94**, 1043 (2003).

[73] J. B. Boyce et al., Phys. Rev. B **44**, 6961 (1991).

[74] A. S. Erickson, (private communication).

[75] G. S. Bushmarina et al., Sov. Phys. Solid State **28**, 612 (1986).

[76] A. L. Shelankov, Solid State Commun. **62**, 327 (1987).